# Numerical Analysis of Co-flowing Immiscible Liquids in Co-axial Microtubes

**IN-HWAN YANG AND MOHAMED S. EL-GENK**

*Institute for Space and Nuclear Power Studies, and*
*Department of Chemical and Nuclear Engineering*
*School of Engineering*
*University of New Mexico, Albuquerque, NM*

**Technical Report No. ISNPS-2-2013**
Institute for Space and Nuclear Power Studies,
The University of New Mexico
Albuquerque, New Mexico

**July 2013**

# ACKNOWLEDGEMENTS

The University of New Mexico's Institute for Nuclear Power Studies funded this research.

.

# ABSTRACT

This work numerically investigates various controlling parameters affecting emulsification of co-flowing, immiscible Newtonian liquids in coaxial microtubes with a primary emphasis on the dispersity, size and frequency of forming microdroplets, and the regimes for forming the droplets. Parameters investigated include interfacial tension, velocities and viscosities of the continuous and disperse liquids, and diameters of the coaxial microtubes.

The transient two-dimensional momentum and continuity equations of the two immiscible liquids in the axisymmetric computational domain are solved simultaneously with the advection equation of the momentum jump at the evolving surface of the disperse droplet surface. A finite element numerical scheme, in conjunction with the Level Set method in the commercial source code COMSOL Multiphysics version 4.0, are used to solve the governing equations and track the evolving shape, and eventual break-off of the forming droplets. The calculations are validated with reported numerical results of the disperse droplets radius in the dripping, transition and jetting regimes. Additional validation is carried out by comparing present numerical results with reported experimental measurements by Gu et al. (2011) of the monodisperse droplet radius.

Changing the transport properties of the liquids affects the formation dynamics of the disperse droplets. The regimes for forming disperse droplets are "*dripping"*, "*transition"*, and "*jetting"*. Results show that monodisperse droplets are produced in the dripping regime, at low injection velocities of disperse and continuous liquids and high interfacial tension. Increasing the injection velocity of either liquids, develops a

disperse-liquid thread prior to the necking stage and break-off of the primary disperse droplets. The disperse liquid thread then breaks up into a number of negligibly small satellite droplets. This is defined as the transition (or polydisperse dripping). In this regime, the size of the primary droplet is typically smaller than that in the dripping regime, but the number and total volume of the satellite droplets increases as the length of the disperse liquid thread increases. Further increase in injection velocities increases the length of the disperse-liquid thread, which eventually evolves into a stable jet. The formation of a stable disperse-liquid jet and the break-off of disperse droplets by hydrodynamic instability at the tip of the jet, marks the transition to the jetting regime. In this regime, the sizes of the disperse droplets are comparable, but not identical, and much smaller than in the dripping and transition regimes.

The numerical results are used to generate motion picture movies, which are carefully examined to identify the prevailing regime of forming disperse droplets. The compiled results show distinct boundaries among the formation regimes of the droplets. The conditions for shifting the formation of disperse droplets from dripping to transition and from the latter to jetting are accurately predicted by the present numerical simulations. The developed semi-empirical correlations for characterizing the boundaries between the dripping, transition and jetting regimes use relevant dimensionless parameters. There are the Capillary number of the disperse liquid ($Ca_d$), the dynamic force ratio of the continuous and disperse liquids ($\mu_r \bar{u}_r$), and the microtube radius ratio ($R^*$). These correlations are in good agreements with the results of the reported experimental data in the dripping and jetting regimes. The experimental results are for different immiscible liquids, including ionized water and PDMS (Polydimethylsiloxane) oil with $R^* = 10$, and aqueous solutions

of glycerine into silicone oil flow with and without surfactant (Sodium Dodecyl Sulfate) with $R^* = 13.8$ (Utada et al., 2007; Guillot et al., 2007; Herrada et al., 2008).

In addition, the predictions of the developed correlation for the boundary between the transition and jetting are compared with the performed calculations using linear instability analysis. The results of the linear instability analysis are lower both of the experimental data and the present correlation for the boundary between the transition and jetting regimes.

The present numerical analysis predicts the size of the primary disperse droplet, and the sizes and number of satellite droplets. The results are used to develop semi-empirical correlations for calculating the radius and the formation frequency of the disperse droplets in the dripping regime, as well as in the transition regime when the total volume of the satellite droplets is < 1% of the primary droplets. These correlations are formulated in terms of relevant dimensionless number. There are the continuous liquid capillary number ($Ca_c$), the ratios of Reynolds numbers ($Re_d/Re_c$), and microtube radii ($R^*$) of the co-flowing liquids. The developed correlation for the dimensionless radius of the disperse droplet ($r_d^*$) is within ±10% of the numerical predictions. The correlation of the dimensionless formation frequencies ($f^*$) of the disperse droplets, are in good agreement with the numerical results, to with ±20%.

The developed dimensionless correlations in this study would be useful tools for determining the boundaries between the dripping, transition and jetting regimes, as well as for estimating the radius and formation frequency of micro-emulsions. In healthcare, food processing, fertilizer, animals feed, chemical petroleum, energy, pharmaceutical, cosmetics polymerization industries demanding monodisperse micro-emulsions, these

dimensionless correlations are directly applicable to designing prototype or commercial coaxial microtubes emulsion generators.

# TABLE OF CONTENTS

# LIST OF FIGURES

# LIST OF TABLES

# NOMENCLATURE

| | |
|---|---|
| $Ca$ | Capillary number of liquid, $\mu_n \bar{u}_n / \sigma_{d,c}$ |
| $Ca^*$ | Normalized capillary number, $Ca^*_{d,TJ} = \left(1 + 0.01\left(R^{*2}\mu_r \bar{u}_r\right)^{2.7}\right)^{-0.27}$ |
| $f$ | Frequency of forming droplet (Hz) |
| $f^*$ | Dimensionless frequency of forming droplet, $f_{mb} R_d / \bar{u}_d$ |
| $g$ | Acceleration of gravity (m/s$^2$) |
| IM | Imaginary part of complex number |
| RE | Real part of complex number |
| $Ka$ | Capillary number of basic disperse liquid flow , $\mu_d u^0_{z,\text{int}} / \sigma_{d,c}$ |
| $k$ | Wave number (m$^{-1}$) |
| $k^*$ | Dimensionless wave number, $r_j^0 k$ |
| $L$ | Length of continuous liquid flow microtube (μm) |
| $p$ | Pressure (Pa) |
| $p'$ | Perturbed pressure (Pa) |
| $\hat{p}$ | Linearized perturbed pressure (Pa) |
| $\hat{p}^*$ | Dimensionless linearized perturbed pressure, $\hat{p} / (\rho_d \hat{u}^{0\ 2}_{z,\text{int}})$ |
| $Q$ | Liquid flow rate (μl/s) |
| $R$ | Microtube radius (μm) |
| $R_{d,o}$ | Outer radius of inner microtube (μm) |
| $R^*$ | Microtubes radii ratio, $R_c / R_d$ |
| $R_c^*$ | Dimensionless outer microtube radius, $R_c / r_j^0$ |
| $Re_d$ | Inlet Reynolds number of disperse liquid, $2R_d \rho_d \bar{u}_d / \mu_d$ |
| $Re_c$ | Inlet Reynolds number of continuous liquid, $2\left(R_c - R_{d,o}\right)R_c \rho_c \bar{u}_c / \mu_c$ |
| $Re_{\text{int}}$ | Reynolds number of disperse liquid at interface, $r_j^0 \rho_d u^0_{z,\text{int}} / \mu_d$ |
| $r$ | Radial distance (μm) |
| $r_j$ | Radius of disperse liquid jet (μm) |
| $r^*$ | Dimensionless radial distance, $r / r_j^0$ |
| $r_d$ | Radius of disperse droplet (μm) |
| $r_d^*$ | Dimensionless radius of disperse droplet, $r_d / R_d$ |
| $u$ | Flow velocity (m/s) |
| $u^*$ | Dimensionless perturbed flow velocity, $u' / \bar{u}_d$ |
| $u'$ | Perturbed flow velocity (m/s) |
| $\hat{u}$ | Linearized perturbed flow velocity (m/s) |
| $\hat{u}^*$ | Dimensionless linearized perturbed flow velocity, $\hat{u} / \hat{u}^0_{z,\text{int}}$ |
| $\bar{u}$ | Average inlet flow velocity (m/s) |
| $\bar{u}_r$ | Inlet flow velocity ratio, $\bar{u}_c / \bar{u}_d$ |
| $t$ | Time (s) |

$t^*$ dimensionless time, $\hat{u}^0_{z,\text{int}} t / r_j^0$

$We_d$ Weber number of disperse flow, $2R_d \rho_d \bar{u}_d^2 / \sigma_{d,c}$

$z$ Axial distance (μm)

$z^*$ Dimensionless axial distance, $z / r_j^0$

Greek

$\phi$ Distance function of interface (μm)

$\kappa$ Interface curvature (m)

$\kappa'$ Perturbed interface curvature (m)

$\mu$ Liquid viscosity (Pa·s)

$\mu^*$ Dimensionless Viscosity , $\mu / \mu_d$

$\mu_r$ Viscosity ratio, $\mu_c / \mu_d$

$\xi$ Amplitude of interface perturbation (μm)

$\xi^*$ Dimensionless amplitude of interface initial wave, $u_d^*\big|_{r=r_j^o} /(i(\omega^* - k^*)$

$\rho$ Liquid density (kg/m$^3$)

$\rho^*$ Density ratio, $\rho_c / \rho_d$

$\sigma_{d,c}$ Interfacial tension, (N/m)

$\tau'$ Shear tensor

$\psi$ Perturbed stream-function

$\omega$ Wave frequency (1/s)

$\omega^*$ Dimensionless wave frequency, $r_j^0 \omega / u^0_{z,\text{int}}$

Superscript

*0* Basic flow

Subscript

*c* Continuous

*d* Disperse

DT Dripping-transition boundary

TJ Transition-jetting boundary

int Disperse-conitnuous liquids interface

*mb* Mass balance

*n* Liquid Identifier, (*c* = continuous or *d* = disperse)

*num* Numerical

*r* Radial

*z* Axial

# 1. INTRODUCTION

Micro-emulsion is a mixture of two immiscible liquids, one of which is dispersed in the form of micro-scale droplets in the other. The micro-emulsion is one of commonly encountered two phase's system. The disperse droplets in the continuous liquid have very strong interfacial tension due to their small radius (1 - 1000 μm). The strong interfacial tension encapsulates the disperse liquid within the droplets, and protects from the dynamically active or inactive continuous phase liquid. This capsulation ability of disperse droplets has been used for various industrial applications in the last century. For example, in medical applications emulsions are employed to encapsulate a bio-sample within the micro-droplets. Typical industrial applications include food, chemical, petroleum and pharmaceutical industries. In these applications, effective emulsion generators with good control of the size and formation frequency of the droplets are highly desirable.

In addition to the established applications, emulsions are attracting attention for micro-scale chemical processes. Because of the advances in controlling the sizes of droplets, emulsion droplets offer the advantage of greater quantitative control to micro-scale chemical reactions. For example, a controlled size of monodisperse droplets is highly desirable in Lab-on-a-chip (LOC) applications to improve the reaction efficiency of chemical reagents. Lab-on-a-chip (LOC) devices comprised of microchannels and sensors are invented for the analysis of micro-sized bio and chemical samples (*e.g.,* Manz, Graber, N., and Widmer, 1990; Munson et al., 2004; Brivio, Verboom, and Reinhoudt, 2006). When samples and chemical reagent solutions are injected into a LOC device together, the chemical reactions of samples with reagents proceed as they travel through the microchannel. The completely reacted samples with the reagents are finally detected by a

sensor, the downstream of a LOC device. In this process, however, the reagents included in the solution disperse through a microchannel while they are traveling within the liquid flow. This inevitable dispersion causes the reduction in the concentration of the reagent around a sample. As the result of this inevitable reduction, the detection efficiency of a sensor on the reacted sample could be reduced because of the sample reacting with an insufficient amount of the reagent. To overcome this limitation, emulsion droplets with a size slightly larger than that of the sample are used as a micro-container for completely suppressing the dispersion of chemical regents in a transport liquid. The impermeable interface between the disperse and continuous liquids has the role of a compartment for isolating reagents within droplets, corresponding to traditional chemist's flask. The continuous liquid flow, therefore, delivers samples completely reacted with highly concentrated reagent within a droplet to the designated place for detecting the reacted samples in a Lab-on-a-chip device (Kelly et al., 2007; Tewhey et al., 2009; Velve-Casquillas et al., 2010). This capsulation ability of droplets is also applicable into manufacturing homogenous micro-particles or vessels.

A controlled-size of monodisperse droplets is being demanded for manufacturing micro-vessels. Several experiments (Cygan et al., 2005; Yuyama et al., 2000; Carroll et al., 2008; Yang et al., 2009; Ziemecka et al., 2010) demonstrated that emulsion droplets can be solidified by chemical reaction at the interface without changing their initial shape and size. These particles can encapsulate a solution containing a specific material for its own needs. Such solidified emulsion of a specific core material encapsulated by a water-soluble shell is desirable to delivering drug, cosmetics and food additive materials within the human body. The solidified surface of emulsion droplets controls the release rates of the core

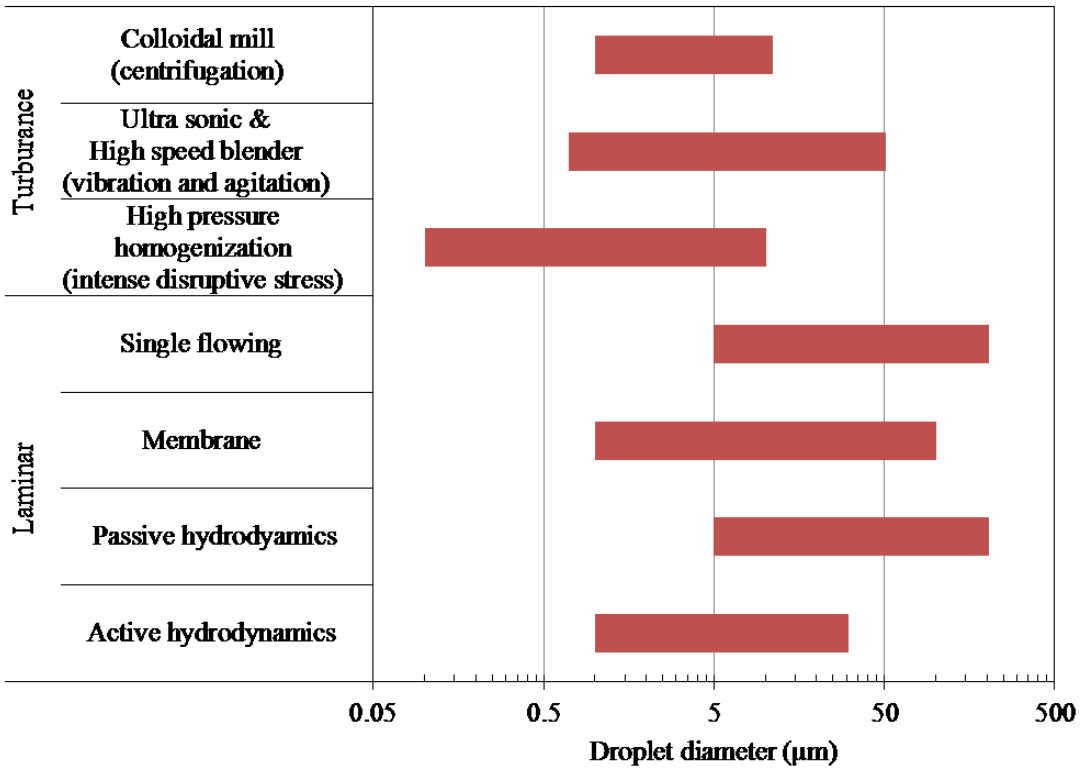


**Figure 1.1. Relative range of the disperse droplet diameters generated by various techniques (Akoh and Min, 2008).**

material at the targeted sites by retarding the dissolving progress with the controlled size of the water-soluble shell, as well as protects reactive core materials from chemical attack in the delivering process.

In all potential applications of micro-emulsion, controlling the size and monodispersity of the emulsion are a key. In the last decade, the process for emulsification has been the subject of numerous investigations to achieve a controlled-size of monodisperse droplets. The ranges of the disperse droplet diameter by the various emulsification techniques/methods of two immiscible liquids are cited in Figure 1.1 and discussed in the next subsection.

## 1.1. Emulsification Techniques for Two Immiscible liquids

Two immiscible liquids are emulsified by hydrodynamic forces induced by the motions of the two liquids and the interfacial tension force between them. Conventional techniques for emulsification use chaotic motions of two immiscible liquids caused by mechanical implementations, such as agitation, vibration, and centrifugation (Akoh and Min, 2008). Two immiscible liquids in a tank are initially separated by a homogeneous interface. This initial interface is disrupted by the strong liquids motions when an agitator mixes the liquids. The two liquids are mixed in an agitated tank, where one liquid is dispersed into the other as small droplets. The conventional techniques produce sub-micrometer droplets by increasing the mechanical energy for enhancing the chaotic motions of the liquids. In emulsifying two immiscible liquids, the strong chaotic motions produce highly polydisperse droplets (> 30 %). Such high polydispersity is undesirable in chemical processes demanding monodispersity.

To obtain monodisperse emulsion droplets, the single flowing (Zhang and Basaran, 1995; Homma et al., 2006; Jin, Gupta, and Stebe, 2006) and the membrane extrusion techniques (Kobayashi et al., 2002; Abrahamse et al., 2002; Vladisavljevic, Shimizu, and Nakashima, 2004; Kobayashi et al., 2004) have been developed. In the single flowing technique, at a constant flow rate a liquid is injected through a small capillary tube into the other immiscible liquid. While one liquid is injected from a capillary tube into another quiescent or dynamically inactive liquid, forms a pendent droplet that breaks off periodically from the tip of the capillary tube. This process of disperse droplets, formation occurs repeatedly by the competition between the hydrodynamic force induced by the injected liquid and the interfacial tension. This method has the advantage of obtaining monodispese droplets by controlling the hydrodynamic force of the injected liquid. Controlling the hydrodynamic force by the volumetric flow rate of the injected liquid can significantly reduce the polydisperisty of the emulsion to less than 10 % of the average size. However, the single flowing method is incapable of controlling the disperse droplet size due to the coalescence of the produced droplets in the quiescent continuous liquid.

The membrane extrusion technique (Figure 1.2a) focuses on increasing the production rate, as well as improving the consistency in the size of produced droplets. In this method, the disperse liquid, passing through homogenous micro-pores of a membrane, is injected into a cross-flow of the continuous liquid. At the interface between a membrane and the continuous liquid, droplets grow and then are swept away by the continuous liquid flow. A several micro size pores in a membrane can produce a fraction of micro size disperse droplets. However, the polydispersity of emulsion is ~16%, because the pressures driving the disperse liquid through each micro-pore of the membrane can not be directly

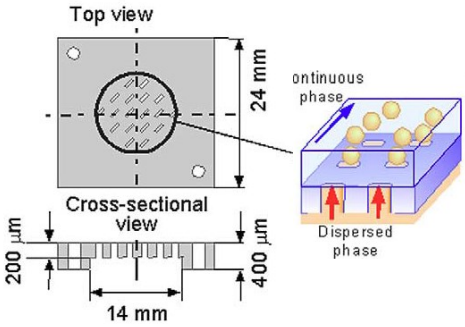


(a) Membrane Extrusion
(Kobayashi et al., 2004)

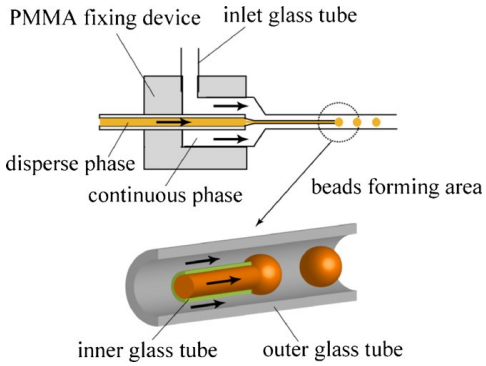


(b) Passive hydrodynamic method:
coaxial microtubes
(Gu et al., 2011)

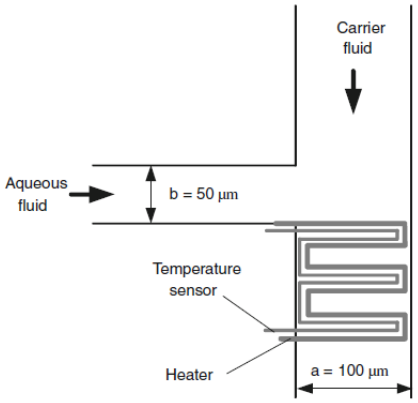


(c) Active hydrodynamic method:
thermal field
(Murshed et al., 2009)

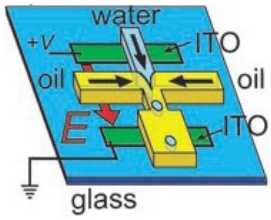


(d) Active hydrodynamic method:
electric field
(Link et al., 2006)

**Figure 1.2. Schematic diagrams of emulsification methods of two immiscible liquids.**

controlled.

To overcome some or all of the conventional technique limitations, a recent technique using co-flowing immiscible liquids in microchannels or microtubes has been proposed (Figure 1.2b). As the surface-area-to-volume ratio of a liquid exponentially increases with decreasing the hydraulic diameter, the liquid flow is dominated by the viscous force. This method uses the viscous force of co-flowing liquids to control the size of forming droplets (Passive hydrodynamic method). This technique not only achieves a good control of the droplet size, but also produces monodisperse droplets. The co-flowing techniques entail injecting a disperse liquid into a continuous immiscible liquid flow in a microtube or microchannel. The disperse liquid, injected at a constant flow rate grows, deforms, and eventually pinches off in a cyclic fashion at the tip of a microtube or microchannel by the result of a net force on the interface of the immiscible liquids. The generated droplets are continuously carried out the downstream by the constant flow motion of the continuous liquid.

Recently, the technology of using co-flowing immiscible liquids has been developed to enhance co-flowing method with an additional force field generated from an outer flow field (Active hydrodynamic method). Some research have shown that controlling the strength of an additional force field (Suryo and Basaran, 2006; Ting et al., 2006; Tan et al., 2008; Murshed et al., 2009) or an electric field (Link et al. 2006; Wang, Yang, and Li, 2009), produces various size droplets at a given flow rate of the co-flowing immiscible liquids in microchannels. These methods use the dimensional advantage of microchannels, where the micro-scaled hydraulic diameter of liquid flow response very fast to an external force. The force induced by an external thermal (Figure 1.2c) or electric

source (Figure 1.2d) actively involves the droplet's formation process, affecting the forces balance at the interface between the two immiscible liquids. This active hydrodynamic method of using an additional force field, however, is costly compared to the passive hydrodynamic method, because of the actuator embedded into the system for controlling and generating an additional force filed. Therefore, the passive hydrodynamic method for emulsification of co-flowing immiscible liquids, without an additional force field, is extensively used for producing disperse droplets. The next subsection presents various arrangements of immiscible liquids flows for producing disperse droplets with the hydrodynamic forces of co-flowing immiscible liquids.

## 1.2. Arrangements of Co-flowing Immiscible Liquids

Without an additional force field (passive hydrodynamic method), a good control of droplet size can be achieved using co-flowing immiscible liquids and by varying the transport properties and the injection flow rates of the continuous and disperse liquids. In techniques using co-flowing immiscible liquids (Figure 1.3), the sizes of forming disperse droplets can be effectively controlled by changing the injection flow rate of the continuous liquid, affecting the hydrodynamic drag force acting on the interface between immiscible liquids. Umbanhowar, Prasad, and Weitz (2000), and Cramer, Fisher, and Windhab (2004) have shown in their experiments that the polydispersity of the emulsion droplets using this method was less than 3%.

In the passive techniques for producing monodisperse emulsions, three arrangement of co-flowing immiscible liquids have been extensively used: T-shape microchannels (Garstecki et al., 2006; Xu et al., 2006; Menech et al., 2008; Gupta, Murshed, and Kumar, 2009; Zagnoni, Anderson, and Cooper, 2010), Flow-focusing

microchannels (Garstecki, Stone, and Whitesides, 2005; Carroll et al., 2008; Cubaud and Mason, 2008; Ziemecka et al., 2011; Liu and Zhang, 2011), and coaxial microtubes (Sakai et al., 2004; Serra et al., 2007; Gu, Kojima, and Miki, 2011). Figure 1.3 shows these arrangements for producing disperse droplets using co-flowing immiscible liquids.

The T-shape (Figure 1.3a) and Flow-focusing microchannels (Figure 1.2b) arrangements are invented to enhance droplet formation using the inertial force of the continuous liquid and the viscous drag acting on the interface. For example, in a T-shape microchannel, the inertia and viscous forces of the continuous liquid can generate disperse droplets by breaking the disperse liquid stream injected through a perpendicular microchannel to the continuous liquid flow. The flow-focusing microchannel uses the inertia and viscous forces of two streams of continuous liquid, injected from symmetric inlet microchannels. The injected continuous liquids squeezes and pinches off the disperse liquid stream in the junction area, producing disperse droplets (Figure 1.3b).

Using coaxial microtubes (Figure 1.3c) provides good control of the disperse droplet formation by the hydrodynamic drag force of the continuous liquid flow. Co-flowing immiscible liquids in coaxial microtubes could not directly take advantage of the inertial force of the continuous liquid for forming disperse droplets.

However, this arrangement eliminates the effect of wall wettability, on suppressing the interaction between the disperse liquid and the wall of the continuous liquid microtube. Furthermore, the low Reynolds number of the disperse liquid, due to micro-scale radius of the injection capillary, eliminates the effect of its inertia on the droplet formation. Therefore, co-flowing immiscible liquids in coaxial microtubes generate monodisperse droplets.

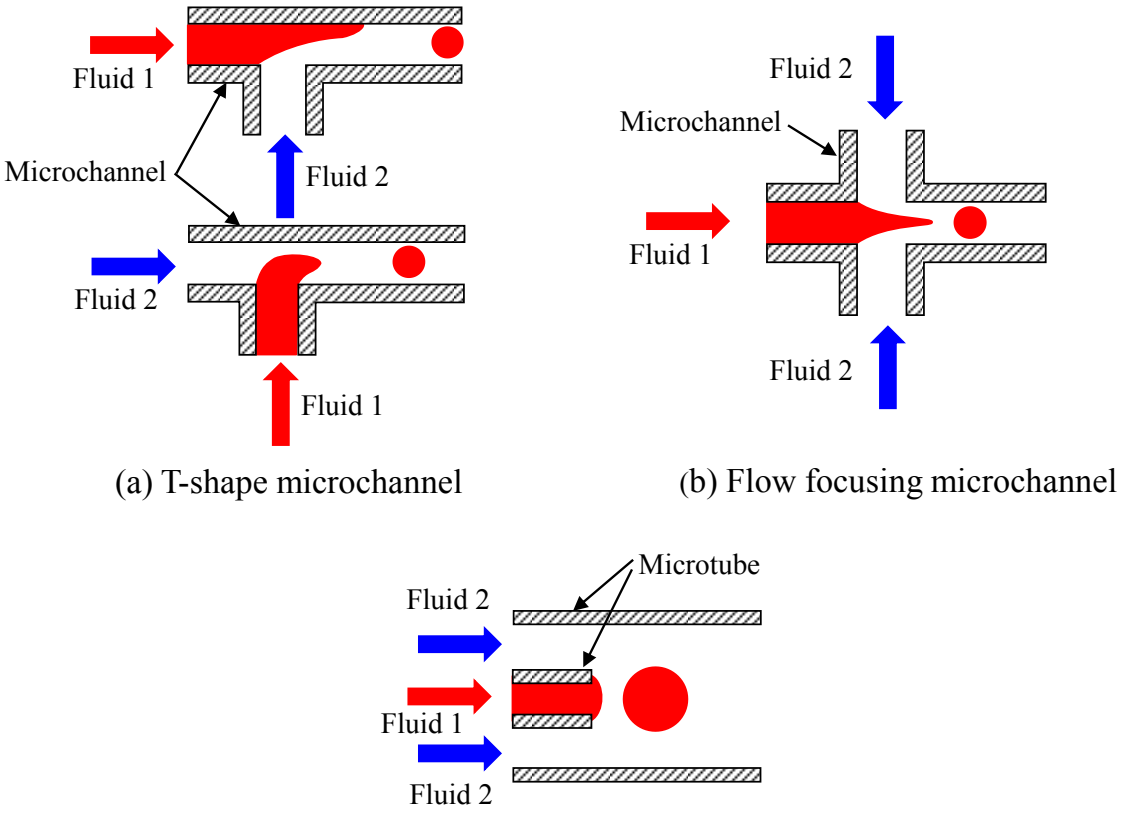


**Figure 1.3. Schematic diagrams of different co-flowing emulsion generators: T-shape microchannle (a), flow focusing microchannel (b), coaxial microtubes (c).**

## 1.3. Focus of Present Research

As mentioned in the previous section, using co-flowing immiscible liquids in coaxial microtubes is effective for generating monodisperse droplets. Recent studies have successfully demonstrated the effectiveness of this technique (Sakai et al., 2004; Cramer, Fisher, and Windhab, 2004; Serra et al., 2007; Gu, Kojima, and Miki, 2011). In coaxial microtubes, one liquid exiting from the inner microtube at very low Reynolds number ($Re_d < 1$) is dispersed as mono- or poly-disperse droplets in the other immiscible liquid flow. The physical properties affecting the droplet formation are the injection velocities and microtubes diameter of the disperse and continuous liquids, and the interfacial tension. The regimes of forming disperse droplets are: (a) dripping, in which the droplet detaches directing off the tip of the inner microtube, (b) transition, in which the break off of the primary droplet is followed by the formation of a number of tiny satellite droplets, and (c) jetting, in which the forming droplet detaches at the end of a stable jet of the disperse liquid, some distance downstream from the tip of the inner microtube. Monodisperse droplets are typically produced in the dripping regime. By contrast, the forming emulsion in the jetting regime could be highly polydisperse. Therefore, many of the reported studies on droplets formation using this arrangement have focused on the dripping and jetting regimes. The transition regime that tolls between dripping and jetting has been ignored or considered a part of dripping.

Table 1.1 provides a brief summary of some the reported studies investigating the dynamics of disperse droplet formation using co-flowing immiscible liquids in coaxial microtubes. The list in this table is not exhaustive, but representative of some previous research. The investigations listed in Table 1.1 have studied the effect of various

parameters (e.g. flow rates, viscosity, density, surface tension, dimensions of microtubes) on the dynamics of forming disperse droplets.

Reported results of experimental and numerical studies have enhanced the understanding of the dynamics of forming disperse droplets using co-flowing immiscible liquids in a coaxial microtubes. However, limited information on the parameters affecting the droplets formation has been provided. Thus, comprehensive investigation needs to be conducted to characterize the droplet formation for developing dimensionless quantities to use in predictive correlations of the radius and formation frequency of the monodisperse droplets, as well as developing a flow regimes map. Examples of these dimensional quantities are Capillary, Reynolds numbers, and the diameters of the coaxial microtubes for the co-flowing immiscible liquids.

In this research, the various parameters affecting the formation and the size and frequency of forming disperse droplets using co-flowing immiscible liquids in coaxial microtubes are investigated numerically. The investigated parameters include the interfacial tension, the velocity, viscosities of the continuous and disperse liquids, and the diameters of the coaxial microtubes. The main objective of the present work is to develop a flow regimes map and dimensionless correlations for the boundaries between the various regimes of forming droplets (dripping, transition and jetting), and developed dimensionless correlations for calculating the radius and formation frequency of disperse droplets in the dripping and transition regimes.

The transient momentum and continuity equations of the liquids, subject to the momentum jump condition at the interface, are solved to tracks the evolving interface between the co-flowing immiscible liquids in coaxial microtubes. A finite element

**Table 1.1. Summary of selected investigations of droplet formation in using co-flowing immiscible liquids in coaxial microtubes.**

| Reference | $\mu_d$ (Pa·s) | $\mu_c$ (Pa·s) | $\sigma_{d,c}$ (mN/m) | $R_d$ (μm) | $R_c$ (μm) | Formation regime |
|---|---|---|---|---|---|---|
| Serra et al. (2007) | 0.00072 | 0.35 - 1.45 | N/A | 55, 130 | 530 - 800 | Dripping |
| Gu et al. (2011) | 0.001 - 2.52 | 0.000294 - 0.073 | 1.42 - 42.8 | 55 - 114 | 185 - 260 | Dripping |
| Yang and El-Genk (2011) | 0.0078 - 0.124 | 0.0078 - 0.124 | 8 - 190 | 50 - 100 | 160 - 2020 | Dripping & Jetting |
| Hong and Wang (2007) | 0.001 | 0.00332 | 15 | 10 | 20 | Dripping & Jetting |
| Umbanhowar et al. (2000) | 0.0033 - 0.037 | 0.001 | 4.9 - 9.3 | 0.35 - 50 | N/A | Dripping |
| Utada et al. (2007) | 0.001 - 0.00935 | 0.001 - 0.0966 | 4 - 40 | 10 - 100 | 1000 | Dripping & Jetting |
| Ulmeanu (2008) | 0.001 | 0.0021 | 4.8 | 2 - 15 | N/A | Dripping & Jetting |
| Herrada et al. (2008) | 0.001 - 0.65 | 0.001 - 0.65 | N/A | 20, 50 | 275, 430 | Dripping & Jetting |
| Sakai et al. (2004) | N/A | 0.1455 | N/A | 150 - 470 | 1250 | Dripping & Jetting |
| Cramer et al. (2004) | 0.001 - 0.244 | 0.049 | 28.33 - 20.45 | 10, 50 | 500, 2000 | Dripping & Jetting |
| C.-Hernandez et al. (2009) | 0.0015 - 0.1 | 0.0015 - 0.1 | 40 | 20 - 30 | 500 | Jetting |
| Cramer et al. (2002) | 0.048 - 0.0485 | 0.046 - 0.486 | 8.66 - 9.92 | 500 - 1195 | 6500 | Jetting |

numerical method and the simulation capabilities in the commercial software COMSOL Multiphysics version 4.0 are used to perform numerical analysis.

## 1.4. Research Objectives

This research aims to perform parametric analysis for enhancing the current understanding of forming disperse droplets in various regimes, based on the use of co-flowing immiscible liquids in coaxial microtubes. The specific objectives of this research are:

1. Perform numerical calculations to simulate the processes of forming droplets using co-flowing immiscible liquids in coaxial microtubes. The present numerical analysis solves the transient momentum and continuity equations of the liquids, subject to the momentum jump condition at the interface, for tracking the evolving interface between the co-flowing immiscible liquids.
2. Validate the numerical solution methodology and implementation used in this study by comparing the calculated values of the disperse droplet radius and the conditions for shifting the regimes of forming droplets with reported values by Hua et al (2007). and Gu et al. (2011).
3. Perform a parametric analysis, which investigated the effects of the liquids' properties and injection velocities, the interfacial tension, and the radii of the coaxial microtubes on the regime of forming disperse droplets.
4. Develop dimensionless correlations, based on the results of the performed parametric analysis and the developed flow regimes map, to predict the boundaries between dripping, transition and jetting regimes. These correlations are also

validated by comparing with experimental measurements by others(Cramer, Fischer and Windhab, 2004; Gu, Kojima and Miki, 2011; Utada et al., 2007; Guillot et al., 2007; Herrada and Ganan-Calvo,2008)

5. Perform a parametric analysis on forming disperse droplets. The numerical simulations investigate the contributions of various parameters affecting the radius and frequency of monodisperse droplets in the dripping and transition regimes.
6. Develop correlations for predicting the size and formation frequency of forming monodisperse droplets by using the results of the parametric analysis. The developed correlations are validated by comparing with recently reported experimental measurements by investigators for water-salad oil flows in coaxial microtubes.
7. Perform linear stability analysis for predicting the boundary between the transition and jetting regimes and comparing the results with the developed flow regimes map and reported numerical results and experimental data.

The next chapter (Chapter 2) provides details on the forming droplets using co-flowing immiscible liquid in coaxial microtubes. This chapter also reviews published studies on the flow regimes of forming droplets, the prevailing parameters affecting on the sizes and formation frequencies of droplets. Chapter 3 provides the problem statements and presents the radii of coaxial microtubes and the ranges of the physical properties of the co-flowing immiscible liquids, including the densities and viscosities, and the interfacial tension. Chapter 3 also provides details of the numerical solution methodology and implementation, for tracking the evolving interface of co-flowing immiscible liquids in the coaxial microtubes. Chapter 4 reports the results of the numerical simulations on the

breakup of the disperse droplets and their breakup mechanisms for characterizing the conditions of the droplets formation regimes. This chapter also provides a flow regimes map for the forming disperse droplets. Chapter 5 presents and discusses the results of the performed linear instability analysis. Chapter 6 presents and discusses the results of a parametric analysis of the formation dynamics of monodisperse droplets and semi-empirical correlations for determining the dimensionless radius and formation frequency of the disperse droplets. Chapter 7 provides a summary and conclusions of the completed research and Chapter 8 discusses some future work to apply the developed correlations for forming droplets into a potential application.

# 2. BACKGROUND

The rapid growth in fabrication technologies for semiconductors over the past several decades has provided reliable techniques for constructing micro and nano-sized structures with highly accurate dimensions on substrate, such as silicones, glasses and polymers (Petersen, 1982; R.-Choudhury, 1997; Duffy et al., 1998). These technological advances could manufacture not only simple, but also complicated geometries of microchannels or microtubes for manipulating small amounts of liquid flows. As a benefit of these advanced manufacture technologies, emulsion generators comprised of microchannels or microtubes have been developed. Such devices can produce micro droplets by manipulating small amounts ($10^{-9}$ to $10^{-18}$ liters) of liquid flow.

The emulsion generator manipulating small amounts of liquid produces droplets with diameter ranging from tens to hundreds of micrometers. Such small size droplets are getting attention for use in the bio-chemical analysis, as a vessel where a small amount of chemical or bio-molecules reacts could be encapsulated. For the bio-chemical analysis, these emulsion generators are developed to control the size of droplets which each encapsulates a single bio-molecule (Table 2.1). The mixture of disperse liquid and bio-molecules injected into the continuous liquid flow in an emulsion generator, results in the single bio-molecules being in separate emulsion droplets, the diameter of which is controlled to match the dimension of a single bio-molecule. When adding analytical reagent in the dispersive liquid, this bio-molecule reacts within the flowing droplets. The reacted bio-molecules are detected downstream of the emulsion generator. Therefore, this process of continuous analysis is able to individually manipulate droplets at a very high-throughput (Chabert and Viovy, 2008; Koster et al. 2008; Brouzes et al., 2009).

**Table 2.1. Relative sizes of bio- and chemical molecules.**

| Molecules | Effective Size | Typical Ranges |
|---|---|---|
| Hydrogen | 0.1 nm | 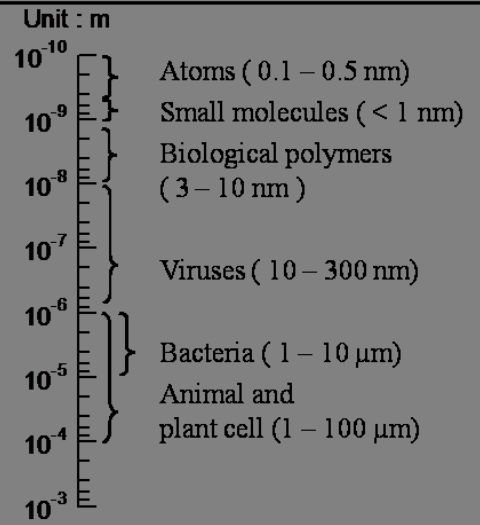 |
| Water ($H_2O$) | 0.27 nm | |
| Glucose ($C_6H_{12}O_6$) | 0.9 nm | |
| Hemoglobin | 6.5 nm | |
| Influenza virus | 130 nm | |
| Baker's yeast | 4 μm | |
| Red blood cell | 8 μm | |
| Skin cell | 30 μm | |
| Human egg | 130 μm | |



A coaxial microtubes is one of the most reliable emulsion generators. In coaxial microtubes, the disperse liquid injected by the inner microtube into the other co-flowing immiscible liquid forms disperse droplets. The continuous liquid flow transports these disperse droplets from the tip of the inner microtube, suppressing coalesces of the generated droplets in the continuous liquid microtube.

Disperse droplets are produced by the effects of the hydrodynamic forces induced by the two immiscible co-flowing liquids and the interfacial tension. However, droplet formation should be in the dripping regime to ensure that the sizes of the droplets are identical (Cramer et al., 2002; Cramer, Fisher, and Windhab, 2004; Serra et al., 2007; Ulmeanu, 2008; Cordero et al., 2011: Yang and El-Genk, 2011). The dripping regime, typically occurring at low injection velocities, produce monodisperse droplets. Increasing the flow rate of the liquids, the forming droplets in the dripping regime shift to the transition and then to the jetting regime. In contrast with the dripping regime, in the jetting

regime, the disperse liquid forms a long jet from the tip of the inner microtube and breaks off polydisperse droplets at the end of the disperse liquid jet, due to the propagating perturbations on its surface. This formation dynamics of the disperse droplets involving instability at the interface results in polydisperse droplets. From the reported experimental results (Cramer et al., 2002; Cramer, Fisher, and Windhab, 2004; Serra et al., 2007; Ulmeanu, 2008; Cordero et al., 2011), the dispersity of the produced droplets in the jetting regime was relatively higher polydispersity than that in the dripping regime. This heterogeneity in the droplet size, therefore, limits the use of droplets as a micro-reactor for the analysis process of a single bio-molecule.

Various researches have used co-flowing immiscible liquid in coaxial microtubes to produce monodisperse droplets. Despite the experimental and numerical work reported, additional work is needed to develop predictive correlations of the size and formation frequency of the droplets and the conditions for having monodisperse emulsion. The following sections provide a background and reviews published studies on forming droplets using co-flowing immiscible liquids in coaxial microtubes.

## 2.1. Forming Droplets in Coaxial Microtubes

The process of the droplet formation basically depends on the hydrodynamic forces induced by the flows of the two immiscible liquids and the interfacial tension. Therefore, the parameters affecting the droplet formation include: the viscosity and density of the disperse liquid, the inlet velocity of the disperse liquid, the viscosity and density of the continuous liquid, the inlet velocity of the continuous liquid, the interfacial tension, and the radii of the inner and outer microtubes. Depending of the different values of their parameters and liquids properties, the disperse liquid injected through the inner microtube

of a coaxial microtubes forms droplets in three distinct regimes, namely, dripping, transition and jetting.

### 2.1.1. Disperse Droplet Formation

The dripping regime, typically occurring at low injection velocities, produces monodisperse droplets. The pinch-off and eventual breakup of the droplets occur at the exit of the disperse liquid capillary nozzle by the interfacial tension force (Figure 1.3c). When the diameter of the continuous liquid microtube is much larger than that of the disperse liquid, the forming droplets are perfectly spherical (Figure 2.1a). The droplet radius decreases with increasing the injection rate of the continuous liquid.

The disperse droplet formation in the dripping regime (Figure 2.2) evolves in three consecutive stages: (1) static growth, (2) necking and (3) break off. These stages of droplet formation occur at the tip of the inner microtube. A cone-shaped interface, left by the detached droplet on the tip of the inner microtube starts a new cycle for a droplet (Figure 2.2a and d). In the static growth stage, the interface steadily grows, depending on the flow rate of the disperse liquid, and becomes a pendent droplet due to the accumulation of the disperse liquid (Figure 2.2b). As the drag force increases in proportion to the expanded interface, the evolved droplet reaching its critical size begins to neck due to the positive net force on the interface associated with the drag force of the continuous liquid and the interfacial tension force at the tip of the inner microtube (Figure 2.2c). In the final stage, the necking droplet rapidly pinches and is eventually detached when the drag force acting on the interface overcomes the surface tension force (Figure 2.2d). Through this repetitive process on droplets, the disperse liquid breaks into disperse droplets periodically in the

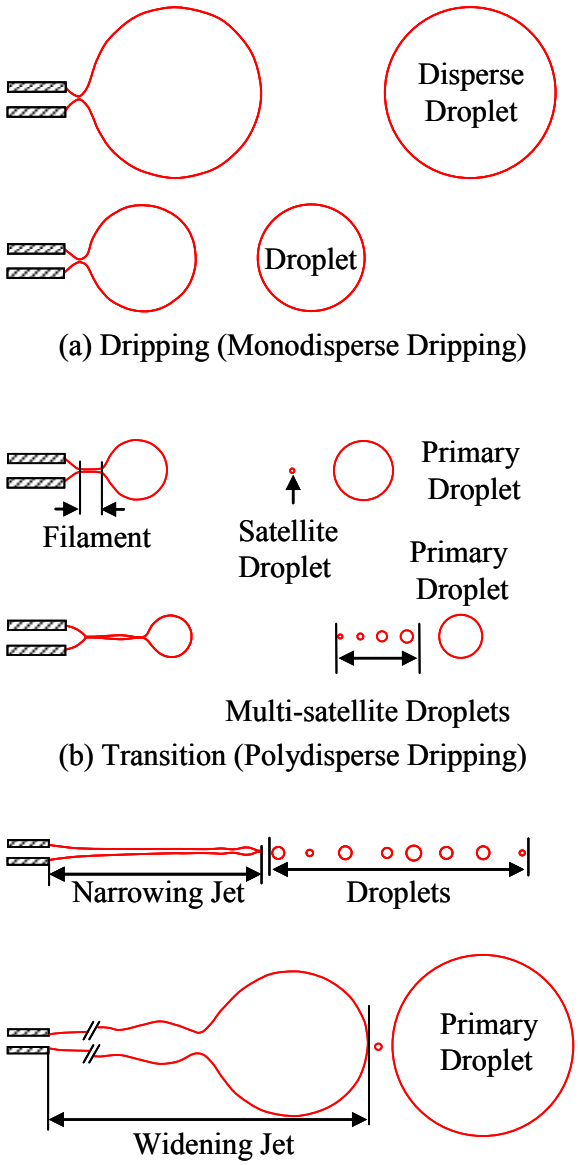


**Figure 2.1. Sketch of different droplet formations in various regimes: (a) monodisperse dripping, (b) polydisperse dripping, and (c)jetting(c).**

continuous liquid flow.

In this dripping regime, precise control of the size and the formation frequency of the forming droplets is generally achieved by varying the inlet flow rates of the co-flowing liquids, their physical properties, and/or the interfacial surface tension. For instance, increasing the flow rate of the continuous liquid decreases the size and increases the formation frequency of the droplets. Additionally, the formed droplets in the dripping regime are monodisperse. Umbanhowar, Prasad, and Weitz (2000), and Cramer, Fisher, and Windhab (2004) reported that the polydispersity (the standard deviation of the diameters divided by mean diameter) in the formed droplets were less than 3% in the dripping regime.

In the transition regime, occurring at higher injection velocities of immiscible liquids than in dripping regime, a disperse-liquid thread forms. It extends from the exit of the disperse liquid nozzle to the growing “primary” disperse droplet at the far end of the thread (Figure 2.1b). The thread could up as much as several droplet diameters long. Following the pinch-off of the “primary” droplet by interfacial tension, the liquid thread separates from the disperse liquid nozzle and becomes hydro-dynamically unstable. It then breaks off into a number of “satellite” droplets of miniature sizes, by a combination of hydrodynamic instability and interfacial tension (Hendrson, Pritchard, and Smolka, 1997; Zhang, 1999; Cramer, Fisher, and Windhab, 2002 and 2004; Serra, 2007; El-Genk and Yang, 2011a,b).

The average size of the primary droplet in the transition regime is typically smaller than in the dripping regime. The number and sizes of the satellite droplets depend on the injection velocities and physical properties of the co-flowing immiscible liquids. They also depend on the interfacial tension and the diameters of the coaxial microtubes

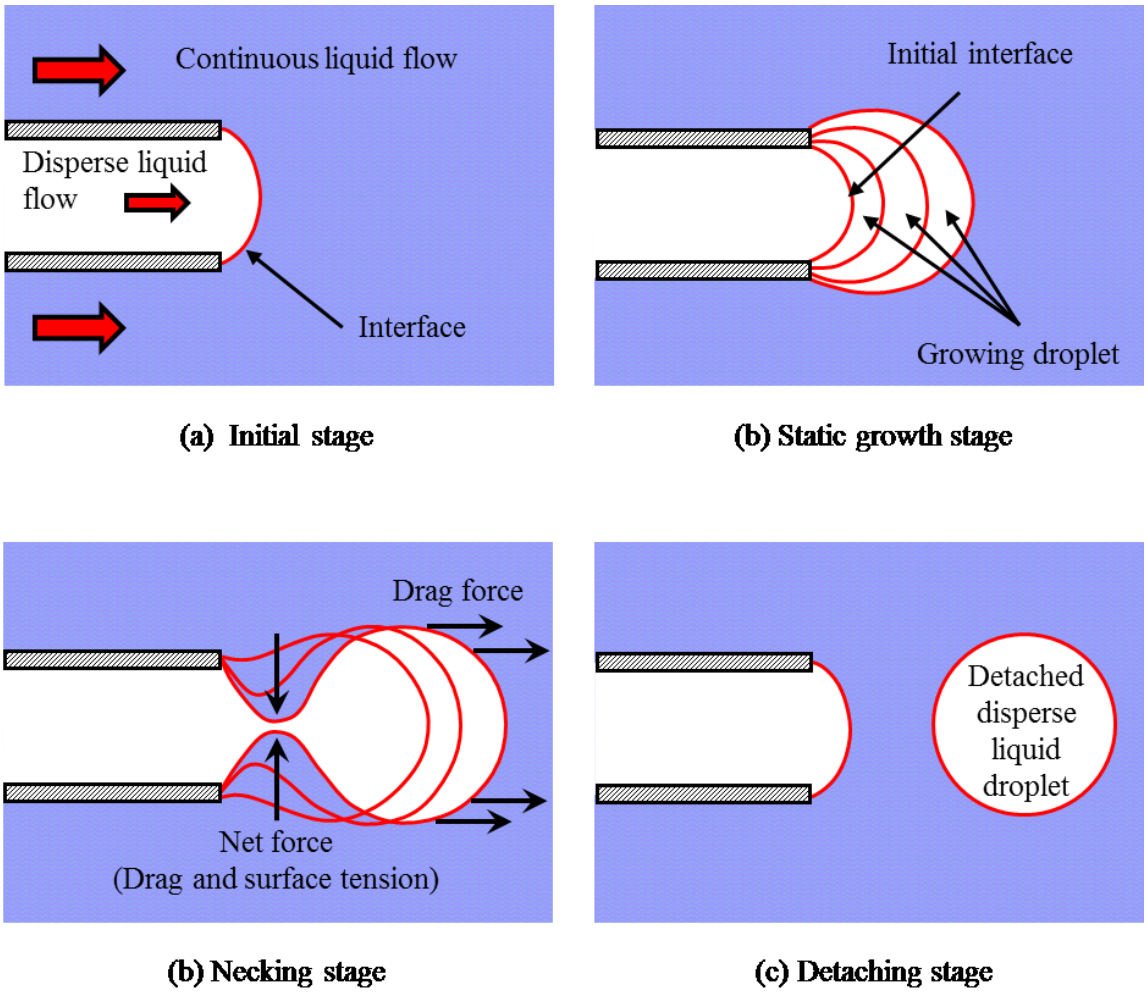


**Figure 2.2. Growth, necking and detachment (or pinch-off) of a disperse droplet at the tip of a microtube in a continuous coaxial flow of an immiscible liquid.**

(Cramer, Fisher, and Windhab, 2002; El-Genk and Yang, 2011a,b). Increasing the injection rate of the continuous liquid typically increases the length of disperse liquid thread, decreasing the size of the primary droplet but increasing the number and sizes of the satellite droplets (Figure 2.1b).

The shift to the jetting regime occurs by increasing the injection velocities of the co-flowing immiscible liquids and/or decreasing the interfacial tension. These conditions increase the length of the disperse-liquid thread. It does not break off, but eventually evolves into either a stable narrowing or widening jet (Figure 2.1c). Disperse droplets form and break off at the tip of these jets by the combined effect of viscous forces of the liquids, interfacial tension and hydrodynamic instability (Utada et al., 2007; C.-Hernandez et al., 2009; Guillot et al., 2007; Herrada and G.-Calvo, 2008; Colin and Tancogne, 2011).

The disperse droplets break off from the tip of disperse liquid jets is sequential at higher frequency than in the dripping and transition regimes. However, the size of the droplets depends on the type of the jet. A narrowing jet (Utada et al., 2007), with a decreasing diameter with distance from the tip of disperse-liquid microtube, produces relatively small, polydisperse droplets. A widening jet (Castro-Hernadez et al., 2009), with an increasing diameter with distance from the tip of disperse-liquid microtube (Figure 2.1c), forms larger droplets and, sometimes, one or a few tiny satellite droplets.

According to experimental results, an irregular breakup of droplets in the jetting flow regime leads to wide distribution in the size of the formed droplets. Cordero et al. (2011) and Ulmeanu (2008) measured the polydispersity of droplets by dividing the standard deviation of the volume and the diameter by its average value, respectively. They reported that their values were within 4 % to 20 %.

## 2.2. Relevant Dimensionless Parameters

The formation dynamics of droplets using co-flowing immiscible liquids in the coaxial microtubes depends on the hydrodynamic forces of the co-flowing immiscible liquids and the interfacial tension. The following dimensionless numbers are used to articulate the different parameters affecting the formation of the droplets, including Capillary number (*Ca*), Webber number (*We*), Bond number (*Bo*). These dimensionless numbers can quantify the relative importance of the hydrodynamic forces of co-flowing liquids to the interfacial tension. The formation of droplets results from the competition between the hydrodynamic force induced by the two co-flowing immiscible liquids, and the interfacial tension.

The capillary number, which describes the relative importance of the viscous force to the interfacial tension force, is expressed as:

$$Ca = \frac{\mu u}{\sigma} \tag{2.1}$$

Where $\mu$ is the dynamic viscosity of the fluid, $u$ is the characteristic velocity and $\sigma$ is the interfacial tension, The importance of the viscous shear and the interfacial tension can be quantitatively reflected by the capillary number. Webber number, which measures the relative importance of a liquid inertia to the interfacial tension, is expressed as:

$$We = \frac{\rho u^2 d}{\sigma} \tag{2.2}$$

In equation (2.2), $\rho$ is the fluid density, and $d$ is the characteristic length. When two immiscible liquids have large difference in their densities, the buoyancy forces induced by the density difference can encourage the process of forming droplets in the

coaxial microtubes. The Bond number quantifies the relative importance of the gravity and the interfacial tension to the interface between the two immiscible liquids. It is defined as:

$$Bo = \frac{\Delta\rho\, g\, d^2}{\sigma} \tag{2.3}$$

For co-flowing immiscible liquids in coaxial microtubes, the contribution of the gravitational force to droplet formation is negligibly small compared to hydrodynamic force of the liquids. Thus, values of the interfacial tension, inertia and the viscous forces determine the dynamics of forming disperse droplets. Other dimensionless parameters related to the liquid properties or the operating conditions should be also important in analyzing the dynamics of droplet formation. Such Reynolds number (*Re*), the ratio of inertia to viscous shear, is also used to characterize the dynamics of the forming disperse droplets.

## 2.3. Shift of Droplet Formation Regimes

Characterizing the conditions for shifting between the dripping, transition and jetting regimes (Figure 2.1) are important for engineering applications. The shift from the dripping flow regime, in which highly monodisperse droplets are generated (Figure 2.1a), to the jetting flow regime, in which polydisperse droplets are produced (Figure 2.1b and 2.1c), has been a subject of theoretical and experimental investigations (Cramer, Fisher, and Windhab 2004; Utada et al., 2007; Guillot et al., 2007; Herrada and G.-Calvo, 2008; Guillot, Colin, and Ajdari, 2008; Hernandez et al., 2009; Cordero Gallaire, and Baroud, 2011; Colin and Tancogne, 2011). The transition from the dripping to the jetting regime is the result of a competition between intrinsic hydrodynamic forces and instability of the interface between the continuous and disperses liquids. While the droplet formation in the

dripping regime depends on the force balance at the interface of the growing disperse droplet with the continuous liquid flow, the droplets formation in the jetting regime is characterized by the propagating instability on the surface of the disperse liquid jet. The individual effect of each parameter affecting the dynamics of the droplet formation is investigated by varying one parameter at a time, while keeping others fixed.

## 2.4. Monodisperse Droplets

The reported results of various experiments and numerical analysis showed that the forming droplets in the dripping regime are monodisperse, whereas the droplets in the jetting regime are highly polydisperse. Therefore, the forming droplets in the dripping regime are more suitable to practical applications where a precise control of the size, formation frequency and mono-dispersity of the droplets are required. Many researchers studied the dynamics of droplet formation in the dripping regime, and investigated potential parameters affecting the size of the forming droplets.

### 2.4.1. Effect of Liquids Flow Rates on Monodisperse Droplets

As mentioned in subsection 2.1, in co-flowing immiscible liquids, the inlet flow rates of the continuous and disperses liquid affect the size, formation frequency and the monodispersity of the droplets as well as the prevailing regime of forming droplets.

Umbanhowar, Prasad, and Weitz (2000) and Ulmeanu (2008) have conducted experiments using co-flowing immiscible liquids to investigate the effect of the continuous liquid flow rate on the size and mono-dispersity of the forming droplets. In their experiments, they injected a disperse liquid into the continuous liquid rotating at a constant angular velocity to provide co-flowing conditions. Umbanhowar, Prasad, and Weitz (2000)

suggested that the drag force of the continuous liquid associated with the velocity and the viscosity affects the droplet's size, when the injection rate of the disperse liquid is small. Ulmeanu (2008) confirmed that increasing the velocity of the continuous liquid decrease the droplet's size, while increasing the flow rate of the disperse liquid increases the size of the droplet. The transition of the droplet formation from dripping to jetting occurs when the flow rate of the disperse liquid increases. In this regime, the forming droplets are inconsistent in size.

Cramer, Fisher, and Windhab (2004) and Utada et al. (2007), have experimentally investigated the effects of the inlet velocities of the continuous and disperse liquids on the droplet formation. They built emulsion generators comprised of a microtube and a coaxial microchannel. To generate coaxial, co-flowing immiscible liquid flow, they placed a microtube at the centerline of the microchannel where the velocity of the continuous liquid is at the highest. Cramer, Fisher, and Windhab (2004) have found that the monodisperse droplets are generated only in the dripping regimes. While keeping the inlet velocity of the disperse liquid constant, increasing the inlet velocity of the continuous liquid reduces the size of the disperse droplets and produces satellite droplets. The volume fraction of these satellite droplets is not negligibly small at high flow rates of the continuous liquid. However, the forming primary droplets at such high flow rate are highly monodisperse (with less than 3% polydispersity). They also reported that jetting regime of the disperse liquid occurs when the diameter of the droplets decrease to as much as the diameter of the inner microtube, because of the higher flow rate of the continuous liquid.

The experimental results of Cramer, Fisher, and Windhab (2004) and Utada et al. (2007) have shown that narrowing jets generally occurs at a relatively low disperse liquid

velocity, at high increasing the viscosity of the continuous liquid or low interfacial tension. The results also showed that increasing disperse liquid velocity causes jetting to occur at low continuous liquid velocity. Cramer, Fisher, and Windhab (2004) and Utada et al. (2007) did not provide, however, a specific criterion or the conditions of the jetting regime. Some researches (Gu, Kojima, and Miki, 2011; Serra et al., 2007; Sakai et al., 2004; Yang and El-Genk, 2011a, b; Hua, Zhang, and Lou, 2007; Hong and Wang, 2007) have experimentally and numerically investigated the effect of the inlet velocities of immiscible liquids on the droplet formation in coaxial microtubes.

Gu, Kojima, and Miki (2011), Serra et al. (2007) and Sakai et al. (2004) have produced various sizes of monodisperse droplets in coaxial microtubes by changing the flow rates of the continuous and disperse liquids. Gu, Kojima, and Miki (2011) have reported that the flow rate of the disperse liquid does not affect the size of the forming droplet. However, increasing the flow rate of the disperse liquid increases the frequency of droplet formation due to the increased growth rate of the pendent droplet at the tip of the inner microtube. They concluded that the droplet's size is decided by the net force between the drag force induced by the continuous liquid flow and the interfacial tension. Serra et al. (2007) suggested that the minimum size of monodisperse droplets is about 1.5 times the inner microtube's diameter. They also proposed a correlation for predicting the relative radius of monodisperse droplet to the radius of the inner microtube, $r_d/R_d$, using an empirical constant, $c$, the capillary number ratio of the continuous liquid to the disperse, $Ca_c/Ca_d$.

$$\frac{r_d}{R_d} = c\left(\frac{Ca_c}{Ca_d}\right)^{-0.22} \tag{2.6}$$

The reported experimental results for emulsions using co-flowing immiscible liquids have contributed greatly to the understanding of the effects of the different parameters on the monodisperse droplet formation. Experiments, however, have inherent limitations because they use intrusive measurement techniques and the imprecise measurements of the droplet diameters less than 80 μm (Cramer, Fisher, and Windhab, 2004). Therfore, numerical simulation can be used to gain an understanding of the prevailing processes and quantify the effects of the different parameters. Numerical simulations, though are not a substitute for experimental investigations, and relatively less expensive time consuming. They are useful for gaining insight into the formation dynamics of the disperse droplets and characterizing the flow fields of the continuous and disperse liquids and the transition of disperse droplets. Therefore, the experimental findings are complemented with the interpretation of results of well executed numerical analyses.

For droplet formation using co-flowing immiscible liquids in coaxial microtubes, different numerical methods have been used to solve the transient Navier-Stokes equations and track the droplet growth and the topology of the interface between the dispersed and co-flowing immiscible liquid. These methodologies include the boundary element method (BEM) (Zhang and Stone, 1997), the volume-of-fluid (VOF) (Hirt and Nichols, 1981; Suryo and Basaran, 2006), the continuum surface force (CSF) (Brackbill, Kothe, and Zemach, 1992), and the front tracking methods (Hua, Zhang, and Lou, 2007). In addition, commercial software such as FLUENT (Hong and Wang, 2007; Vempati, Panchagnula, and Neti, 2007) and COMSOL Multiphysics (Yang and El-Genk, 2011) have been used to investigate the same system.

Zhang and Basaran (1995) and Zhang (1999) have studied, both experimentally and numerically, the dynamics of forming disperse liquid droplet in quiescent and co-flowing immiscible liquids. Hong and Wang (2007) numerically investigated the formation dynamics of the droplets, focusing on the effect of the ratio of the injection rates of the liquids on the size of the forming droplet. Their results suggested that the effect of flow rate of the dispersed liquid barely affects the diameter of the droplet, when the ratio of the flow rates of the disperse to the continuous liquid is greater than 0.1. The numerical results of Yang and El-Genk (2011a,b) suggested that the effect of the disperse liquid flow rate on the size of forming droplet is negligible when inlet Reynolds number and Weber number of the disperse liquid are much less than unity. Their results also showed that increasing the diameter ratio of the outer microtube to the inner microtube increases the droplet size at constant injecting rate of the disperse and continuous liquids.

### 2.4.2. Effect of Liquids Properties on Monodisperse Droplets

A few studies have systematically investigated the effects of the physical properties of the liquids and interfacial tension on droplet formation. Cramer, Fischer and Winhab (2004) experiments by injecting various concentrations of κ-Carrageenan aqueous solution and an aqueous solution of polyethylene glycol (PEG) into sunflower oil flow. Their results showed that the viscosity of the disperse liquid does not affect the size of forming droplets, when the inlet Reynolds number is less than unity. They also investigated the effect of the interfacial tension on the droplet formation. Results showed that increasing the interfacial tension increases the size of forming droplet.

Gu, Kojima, and Miki (2011) have experimentally investigated the size of forming droplet by injecting different dispersive liquids (alginate sodium aqueous solutions or

ethanol) into corn or salad oil. They discussed the effect of the viscosities of the disperse and the continuous liquid, and the interfacial tension on the disperse droplets in the dripping regime. Their results showed that increasing the interfacial tension or decreasing the viscosity of the continuous liquid increases the size of droplets. They confirmed that the size of formed droplets barely changes by changing the viscosity of the disperse liquid. The experimental studies, investigating the effects of physical properties of liquids and interfacial tension, have inherent limitations. This is because of using additives for controlling the interfacial tension or the liquid viscosity (Cramer, Fischer, and Windhab, 2004; Serra et al., 2007; Utada et al., 2007; Herrada, G.-Calvo, and Guillot, 2008; C.-Hernandez et al., 2009; Gu, Kojima, and Miki, 2011). The additives affect not only the targeted property of liquid, but also the rest of physical properties including the density, the viscosity and the interfacial tension. Instead, numerical simulation can manipulate the interfacial tension or the liquid viscosity while keeping other physical properties of liquids constant (Suryo, and Basaran, 2006; Hong, and Wang, 2007; Hua, Zhang, and Lou, 2007; Yang and El-Genk, 2011a,b).

Hua, Zhang, and Lou (2007) have numerically simulated the flow of two immiscible liquids in coaxial microtubes and discussed effects of the continuous liquid viscosity and the interfacial tension. They reported that the diameter of the forming disperse droplet, at fixed flow rates of the liquids, decreases as the viscosity of the continuous liquid increases. They indicated that higher viscosity of the continuous liquid results in higher viscous drag force on the interface. Furthermore, increasing the viscous drag force by increasing the viscosity of the continuous liquid can develops a disperse liquid jet at the tip of the capillary nozzle. Yang and El-Genk (2011a,b) have numerically

investigated the effects of a wide range of liquid viscosities and interfacial tension on the disperse droplet size. Their results showed that increasing the viscosity of the disperse liquid slightly reduces the size of forming droplets.

## 2.5. Summary and Discussion

Co-flowing liquids in coaxial microtubes is a most attractive method for generating monodisperse droplets. However, monodispersity is typically obtained in the dripping regime, where droplets pinch off at the exit of the disperse liquid microtube. Reported research has focused on forming droplets in the dripping regime, assuming the transition regime a part of the dripping regime. The dynamics of forming disperse droplets depend on many parameters. These are the average flow rates of the continuous and disperse liquids; dynamic viscosities and densities, the diameters of the coaxial microtubes and the interfacial tension. The limited results have contributed to the understanding of the effects of various parameters on the size and formation frequencies of disperse droplets in the dripping, transition and jetting regimes. Table 2.2 summarizes the conditions and characteristics of forming droplets in the various regimes of dripping, transition and jetting.

The effect of the continuous liquid drag force on the interface has been investigated using different average inlet velocities and/ or viscosities. Some research groups investigated the effects of the interfacial tension and the drag force induced by the continuous liquid flow, using various combinations of liquids with or without surfactant additives. The viscous drag and the inertial force of the disperse liquid have also been investigated by changing the flow rates and the viscosity of the disperse liquid. In contrast

**Table 2.2 Regimes of forming disperse droplets using co-flowing immiscible liquids.**

| Item | Flow Regime | | | |
|---|---|---|---|---|
| | ***Dripping*** | ***Transition*** | **Jetting** | |
| | | | ***Narrow*** | ***Wide*** |
| **Condition** | Moderate injection velocities, high interfacial tension, low viscous drag | Higher injection velocities and lower interfacial tension | High injection of continuous liquid and interfacial tension | Low injection of continuous liquid and surface tension |
| **Emulsion** | Monodisperse droplets, with infrequent formation of a very tiny satellite droplet | Monodisperse primary droplets, followed by tiny satellite droplets | Polydisperse droplets of small size, rare satellite droplets formation | Monodisperse large droplets with tiny satellite droplets |
| **Primary droplets break off** | Pinch-off by surface tension near exit of the disperse liquid microtube | Pinch-off by surface tension at far end of thin short disperse liquid thread | Hydrodynamic instability at far end of stable disperse liquid jets | |
| **Satellite disperse droplets** | Rare, depending on conditions | Form by breakup of disperse liquid thread by surface tension and instability | Infrequent, following break off of primary droplets | |
| **Formation frequency of primary droplets** | Lower than transition and narrow jetting, but higher than wide jetting | Higher than dripping and wide jetting, but lower than narrow jetting | Very high | Very low |
| **Primary droplet size** | Larger than in transition and narrow jetting, but lower than wide jetting | Much smaller than in dripping and wide jetting regimes | Smallest | Largest |

to the reported results on the effects of the viscous drag of the continuous liquid and the interfacial tension, there were controversial results related to the effect of the viscous force of the disperse liquid on the size of forming droplets. Some researchers (Cramer, Fischer, and Windhab, 2004; Gu, kojima, and Miki, 2011) have reported that increasing the flow rate or the viscosity of disperse liquid does not affect the size of forming droplets. Conversely, Serra et al. (2007), Hong and Wang (2007), and Yang and El-Genk (2011a,b) have reported that the viscous force of the disperse liquid affects the size of the forming droplets, even though the inlet Reynolds number of the disperse liquid is less than unity.

A few researchers have focused on the droplet formation regimes. Assuming the transition (polydisperse dripping) regime a part of the dripping regime, these studies have investigated the effects of physical properties and flow rates of liquids, and interfacial tension on the shift between dripping, transition and jetting. Utada et al. (2007) and Castro-Hernadez et al. (2011) have used dimensionless groups to characterize the droplet formation regimes. However, they did not provide a specific criterion in terms of the dimensionless groups they suggested. A theoretical approach using linear instability analysis has also been used to characterize the droplet formation regime in the jetting regime. In spite of the fact that mathematical formation for an instability analysis of the interface has been simplified by using creeping flow approximation, the instability analysis involves solving complicated algebraic equations and criterion for identifying the transition regime.

In this chapter, a description of droplet formation regimes and a brief discussion of droplet formation dynamics are provided. The reported work analyzing droplet formation in the dropping and the jetting regime are also reviewed. The next chapter provides details

on the present numerical analysis, the problem statement and the radii of coaxial microtubes and presents the ranges of the physical properties of the co-flowing immiscible liquids used in the present research.

# 3. NUMERICAL ANALYSIS

This chapter presents the problem statements including the radii of coaxial microtubes and the ranges of the physical properties of the co-flowing immiscible liquids, and the numerical solution methodology for tracking the evolving interface between the co-flowing immiscible liquids in coaxial microtubes. The numerical solution is validated by comparing the calculated values of the disperse droplet radius and the conditions for shifting the regimes of forming droplets with reported values by Hua et al (2007). and Gu et al. (2011).

Numerical analysis is performed to simulate the formation of disperse droplets of an incompressible and Newtonian liquid at the tip of a microtube with an inner radius, $R_d$, in a co-flowing immiscible, incompressible and Newtonian liquid in a coaxial microtube of a larger radius $R_c$ ($R_c > R_d$) (Figure 3.1). The disperse liquid has a dynamic viscosity, $\mu_d$, and a density, $\rho_d$, and the continuous liquid has a dynamic viscosity, $\mu_c$, and density, $\rho_c$. The numerical analysis investigated the effects of the different parameters on the characteristics and the regimes of forming disperse droplets, as well as the formation frequency and radius of monodisperse droplets. These parameters are the interfacial surface tension ($\sigma_{d,c}$) and the velocities ($\overline{u}_d$ and $\overline{u}_c$), viscosities ($\mu_d$ and $\mu_c$), and radii of the microtubes ($R_d$ and $R_c$) for the co-flowing immiscible liquids. The ranges of parameters investigated in the present numerical analysis are listed in Table 3.1.

## 3.1. Problem Statement

Figure 3.1a depicts the coaxial microtubes used in this numerical analysis. The disperse liquid injected at a constant volumetric flow rate, $Q_d$, emerges from the tip of the inner coaxial microtube into the continuous liquid injected also at a constant, but different

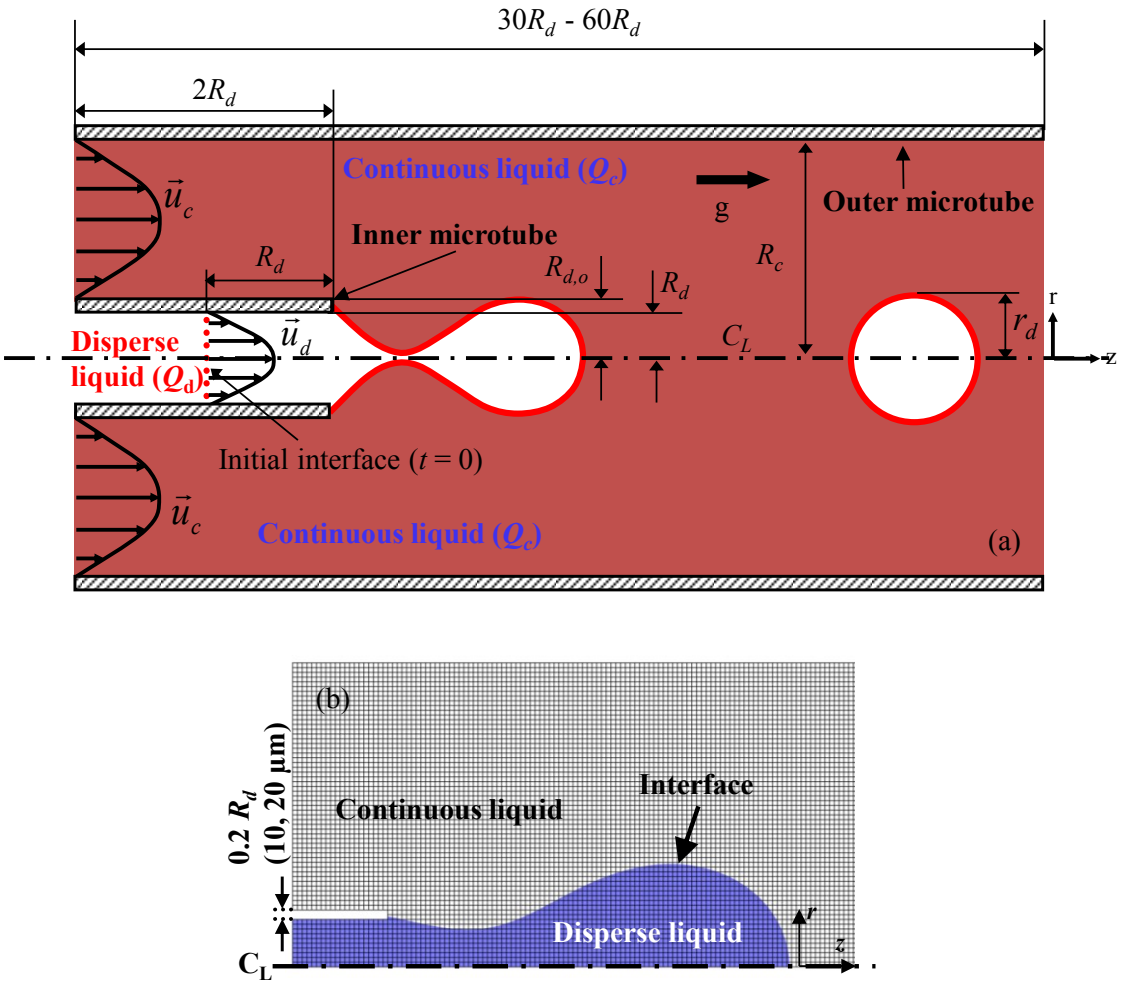


**Figure 3.1. A schematic of a disperse droplet forming in a co-flowing immiscible liquid in a coaxial tubes (a) and a discretized computation domain (b).**

rate, $Q_c$, in the outer coaxial microtube. Fully developed laminar velocity profiles are applied to the co-flowing liquids at the entrance of the coaxial microtube. The length of computation domain ($30R_d$ to $60R_d$) selected in the present numerical simulations is sufficiently long for simulating at least 3 cycles of the forming droplets, including initial formation, growth and pinch off in the dripping, transition and jetting regimes. The numerical analysis in the present study uses two radii of the inner microtube with 50 μm and 100 μm for injecting the disperse liquid. Various radii (160 to 2020 μm) of the outer microtube are also used for injecting the continuous liquid. The wall thickness of the inner microtubes is the inner tube diameter of 10 % (Figure 3.1b). Comparing to the tube inner diameter, such thickness is sufficiently thin to neglect the effect of the wall thickness on the forming droplets (Zhang, 1999; Zhang and Basaran, 1995).

Generally, small diameters of the inner microtube in the coaxial microtubes imply that the inertia of the disperse liquids flow is small due to a large surface-area-to-volume ratio of the inner and outer microtubes. Therefore, the effect of the inertia of the disperse liquid on the droplet formation may be negligible. In this numerical analysis, the flow rate of the disperse liquid is low ($Re_d < 1$ and $We_d << 1$) enough to avoid forming a disperse liquid jet by the inertial force of the disperse liquid. Jetting of the disperse liquid depends on the inlet flow rates of the disperse and continuous liquids, the physical properties of both liquids, and the value of the interfacial tension, as shown later in the chapter 5.

The direction of the gravitational force, g, in Figure 3.1 of the computational domain is aligned with the center line, $C_L$, of the coaxial microtubes. In the jetting regimes, various lengths of outer microtubes are considered to provide enough space for droplet's breakup at the end of a formed disperse liquid jet. Viscous heat dissipation (El-Genk and

**Table 3.1. Ranges of properties and parameters investigated in numerical simulation.**

| Parameter | Value / Range | Units |
|---|---|---|
| Inner microtube radius, $R_d$ | 50 - 100 | μm |
| Outer microtube radius, $R_c$ | 160 - 2020 | μm |
| Disperse liquid viscosity, $\mu_d$ | 0.0031 - 0.124 | Pa·s |
| Continuous liquid viscosity, $\mu_c$ | 0.0075 - 0.124 | Pa·s |
| Disperse/ continuous liquid density, $\rho_d / \rho_c$ | 1000 / 1000 | kg/m$^3$ |
| Interfacial tension, $\sigma_{d,c}$ | 0.01 - 0.0961 | N/m |
| Disperse liquid rate/ velocity, $Q_d / \overline{u}_d$` | 0.0487 - 2.4347 / 0.0062 - 0.31 | μl/s / m/s |
| Continuous liquid rate/ velocity, $Q_c / \overline{u}_c$ | 0.1924 - 9900 / 0.00037 - 2.48 | μl/s / m/s |
| Microtube radius ratio, $R^*$ | 3.2 - 20.2 | – |
| Disperse liquid Reynolds number, $Re_d$ | 0.02 - 1 | – |
| Disperse liquid Capillary number, $Ca_d$ | 0.0016 - 0.3844 | – |
| Continuous liquid Capillary number, $Ca_c$ | 0.0003 - 0.55 | – |
| Disperse liquid Weber number, $We_d$ | 0.0002 - 0.1602 | – |

Yang, 2008, 2009) is neglected and a non-slip condition is assumed at all liquid-solid interfaces. The densities and the viscosities of the co-flowing liquids, as well as the interfacial tension remain unchanged. In the numerical simulation, the density of both liquids and interfacial tension are kept a constant, and the ratio of density is unity to eliminate the effect of the buoyancy force ($Bo = 0$). The values and range of the dominant parameters investigated in the present numerical simulation are listed in Table 3.1. The listed rages of the parameters are carefully selected, considering the ranges of the parameters used in the reported numerical and experimental works on the droplet formation using co-flowing immiscible liquids in coaxial microtubes.

## 3.2. Governing Equations and Numerical Methodology

The present numerical simulations solve the transient momentum balance and continuity equations for the two co-flowing immiscible liquids (Figure 3.1), subject to the prevailing momentum jump condition at the surface of the evolving disperse droplet. The calculated results include: (a) the flow fields of the continuous liquid and inside the growing disperse droplet; (b) the local rate of momentum transfer and movement of the droplet surface as functions of the local curvature and (c) the droplet formation, growth and eventual pinch off. The momentum jump condition across the interface between the growing disperse droplet and the co-flowing continuous liquid is incorporated into the numerical solution using the Level set method (Olsson, Kreiss, and Zahedi, 2007; Gada and Sharma, 2009; Comsol, 2010). The multiphase flow model in COMSOL Multiphysics commercial software, version 4.0a (Comsol, 2010) uses this method for predicting the motion of the interface and the shape of the disperse droplet during its growth to an eventual pinch off.

The momentum balance and continuity equations for the two co-flowing incompressible, Newtonian, and immiscible liquids in a gravitational field (Figure 3.1) are given as:

(a) Continuity Equations:

$$\nabla \cdot \vec{u}_c = 0, \quad and \ \nabla \cdot \vec{u}_d = 0 \tag{3.1}$$

(b) Momentum Balance Equations:

$$\begin{aligned} \rho_c \frac{\partial \vec{u}_c}{\partial t} + \rho_c \vec{u}_c \cdot \nabla \vec{u}_c &= -\nabla p + \mu_c \nabla^2 \vec{u}_c + \rho_c g + F\delta \\ \rho_d \frac{\partial \vec{u}_d}{\partial t} + \rho_d \vec{u}_d \cdot \nabla \vec{u}_d &= -\nabla p + \mu_d \nabla^2 \vec{u}_d + \rho_d g + F\delta \end{aligned} \tag{3.2}$$

In equations (3.2), the interfacial force, *F*, exerted onto the interface between the two immiscible liquids can be confined to the interface by the delta function, $\delta$, which is unity at the interface and zero elsewhere in the computation domain. The interfacial force, *F*, in the momentum balance equations (3.2) obtained from the application of the momentum jump condition at the interface. This condition, equation (3.3a), equates the difference in hydrodynamic stresses exerted onto the interface by the co-flowing liquids to the normal stress associated with the local curvature of the interface and interfacial surface tension as:

$$\vec{n} \cdot \left[\tau_c - \tau_d\right] = F \tag{3.3a}$$

$$F = \sigma_{d,c}\ \vec{n}\ (\nabla \cdot \vec{n}) = \sigma_{d,c}\ \vec{n}\ \kappa \tag{3.3b}$$

In equation (3.3a), $\tau_c$ and $\tau_d$ are the shear stress at the interface due the continuous and disperse liquids flows and $\vec{n}$ is a normal vector to the interface. In equation (3.3b), $(\nabla \cdot \vec{n})$ is replaced by the curvature at the interface, $\kappa$, based on the principal radii of curvature. The motion of the impermeable surface of the disperse droplet is described by the advection equation at the interface between the co-flowing immiscible liquids:

$$\frac{\partial \phi}{\partial t} + \vec{u}_{\text{int}} \cdot \nabla \phi = 0 \tag{3.4}$$

In this equation, $\phi(r,z)$ is a scalar function that indicates the surface of the disperse droplet. The momentum balance and continuity equations are expressed in a dimensionless form as:

$$\nabla \cdot u^* = 0 \tag{3.5}$$

$$0.5\,\rho^*\,\text{Re}_d\,\frac{\partial u^*}{\partial t^*} + \rho^* u^* \cdot \nabla u^* = -\nabla p^* + \mu^* \nabla^2 u^* + \rho^* g^* + \frac{1}{Ca_C\ \mu_r\ u_r}\,\vec{n}\,\kappa^*\,\delta. \tag{3.6}$$

These equations are solved numerically, subject to the condition of non-slip at walls of the coaxial microtubes and assuming axisymmetric coaxial flows of the continuous and disperse immiscible liquids (Figure 3.1). In addition, the isothermal coaxial liquid flows are assumed fully developed, with average velocities determined from the volumetric flow rates at the inlet of the coaxial microtubes (Figure 3.1). The length of the inner coaxial microtube is taken to be 2 times its inner radius ($L_d = 2\,R_d$) (Figure 3.1).

At the start of the transient simulation, $t = 0$, disperse liquid fills the inner microtube half way and the continuous liquid fills the rest of the computation domain. The initial flat interface between the two liquids is located a distance $R_d$ from the tip of the inner microtube (Figure 3.1). Equations (3.5) and (3.6) are solved simultaneously with the dimensionless form of equation (3.4), expressed as:

$$\frac{\partial \phi^*}{\partial t^*} + u^*_{\text{int}} \cdot \nabla \phi^* = 0. \tag{3.7}$$

The numerical solution of those coupled nonlinear equations tracks the movement and the evolution of the surface and the breakup of droplets at the tip of the inner microtube or the disperse liquid jet in the dripping, transition and jetting regimes (Figure 2.1).

### 3.3. Solution Methodology (Level Set Method)

The Level Set Method for implementing the momentum jump condition in the numerical solution at the interface between the co-flowing immiscible liquids (Olsson, Kreiss, and Zahedi, 2007; Gada and Sharma, 2009; Comsol, 2010), uses the function $\phi(r,z)$ to indicate the normal distance from the moving and evolving interface, or the surface of the disperse droplet, throughout the computation domain. In order to deal with non-linearity of the momentum jump condition at the interface, equation (3.3b), without causing a numerical instability, a function $H_\phi$ is introduced and assigned values of 0 and 1, for the disperse and continuous liquids, respectively, thus:

$$\begin{cases} H_\phi = 0, & \text{if } \phi < 0 \quad \text{Continuous liquid} \\ H_\phi = 0.5, & \text{if } \phi = 0 \quad \text{Interface} \\ H_\phi = 1, & \text{if } \phi > 0 \quad \text{Dipersive liquid} \end{cases} \tag{3.8}$$

Based on the these notations, equation (3.7) can be rewritten in terms of the function, $H_\phi$, as;

$$\frac{\partial H_\phi}{\partial t} + u^*_{\text{int}} \cdot \nabla H_\phi = 0 \tag{3.9}$$

The solution of this equation gives the exact motion of the interface. However, in order to implement it numerically, while avoiding possible solution instability, equation (3.9) is expressed as:

$$\gamma \nabla \cdot \left( \varepsilon H_\phi - H_\phi \left(1 - H_\phi\right) \frac{\nabla H_\phi}{\left|\nabla H_\phi\right|} \right) = 0 \tag{3.10}$$

The parameter, $\gamma$, determines the level of stabilization or the amount of reinitialization for the Level Set Method (Olsson, Kreiss, and Zahedi, 2007; Gada and Sharma, 2009; Comsol, 2010). The appropriate value of the parameter, $\gamma$, which is a problem specific, ensures the stability of the numerical solution and the correct prediction of the movement of the interface. The interface separating the growing disperse droplet from the continuous liquid flow is treated as a very thin layer, $\varepsilon$, with average liquid properties and a linear change in momentum across ( $H_\phi$ from 0 to 1). The liquid properties within the interface layer expressed in terms of those of the continuous and disperse liquids, are:

$$\begin{aligned} \rho &= \rho_c + \left(\rho_d - \rho_c\right) H_\phi \\ \mu &= \mu_c + \left(\mu_d - \mu_c\right) H_\phi \end{aligned} \tag{3.11}$$

Also, the unit normal vector to the interface, $\vec{n}$ and the curvature of the interface, $\kappa$, are expressed as:

$$\vec{n} = \frac{\nabla H_\phi}{\left|\nabla H_\phi\right|}, \qquad \kappa = \nabla \cdot \frac{\nabla H_\phi}{\left|\nabla H_\phi\right|} \tag{3.12}$$

The numerical solution of equation (3.10) uses an implicit method to ensure the stability of the simulation. The thickness of the interface layer, $\varepsilon$, is taken equal to the numerical mesh size (5 μm) and the stability, or reinitialization parameter, $\gamma$, is taken as:

$$\gamma = \frac{Q_c + Q_d}{\pi R_c^2} \tag{3.13}$$

In the present numerical simulations, the used mesh grid for the computation domain of the co-flowing immiscible liquids in the coaxial microtubes (Figure. 3.1) is comprised of quadrilateral elements of a uniform size (5 μm × 5 μm). The total number of the numerical mesh elements used, which increases commensurate with radius and length of the continuous liquid microtube, varied from 9,560 to 60,650. The selected length of the computation domain provides enough distance, from the tip of the disperse liquid inner microtube, to obverse the formation and breakup of at least 2 disperse droplets, including the first one.

Using a finer grid, with a larger number of smaller quadrilateral elements, insignificantly changes the results of the simulation, including the diameter and the formation frequency of the disperse droplet, but markedly increases the computation time. With the size and the number of the numerical mesh elements used in the present simulations, the solution fully converges with < 1% in the volume change of the formed primary droplets traveling along the continuous liquid microtube. The mass balance of the disperse liquid for forming the droplets also is within 6% error. This error is mostly due to the formation of very tiny satellite droplets in the computation domain that are difficult to account for in the overall mass balance. The numerical simulations are performed using a cluster of 8 quad core processors (2.27 GHz Xeon) and 120 GB of memory. The real computation time for the simulations varied from 72 to 168 hours per case, depending on the size of the computation domain, radii and lengths of the co-axial microtubes and the selected properties of the disperse and continuous liquids.

The results of the present numerical simulations are validated by comparing the obtained values of the disperse droplet radius with those reported by Hua, Zhang, and Lou

(2007), and Gu, Kojima, and Miki (2011). The results of the comparisons with the reported values are detailed in the next section.

### 3.4. Validation of Numerical Solutions

To validate the results of the present numerical simulations, the calculated values of the radius of forming disperse droplets, $r_{d,num}$, are compared in Figure 3.2 with the reported numerical and experimental values, $r_{d,ref}$, by Hua, Zhang, and Lou (2007), and Gu, Kojima, and Miki (2011). Table 3.2 lists the conditions used in the references for this comparison.

The numerical methodology used in the present research is capable of simulating from the dripping to the jetting regime. In Figure 3.2 comparing the numerical results with Hua et al.'s results spanning the dropping, transition and jetting regimes, the satellite droplets form at the intermediate values of the continuous liquid's inlet velocity, $\bar{u}_c$ (or the disperse droplet radius), while the formation of monodisperse droplets in the same regime prevails at low inlet velocity (or large disperse droplet radius). At high values of $\bar{u}_c$, the jetting regime prevails, producing smaller polydisperse droplets. The transition from the monodisperse to the polydisperse of primary droplets in Figure 3.2 is calculated to occur at $Q_c$ = 78 μl/s (or $\bar{u}_c$ = 0.31 m/s), the same as those reported by Hua et al. (2007).

In addition to Hua et al. (2007), the numerical simulations are also performed with the same conditions Gu et al. (2007) used in their experiments for forming monodisperse water droplet in co-flowing salad oil. The results of the numerical simulation demonstrate the validation of the present numerical methodology again, by the comparison of forming droplet's sizes in Figure 3.2. The results of the transient numerical calculations also successfully demonstrate that monodisperse droplets are produced through the cyclic

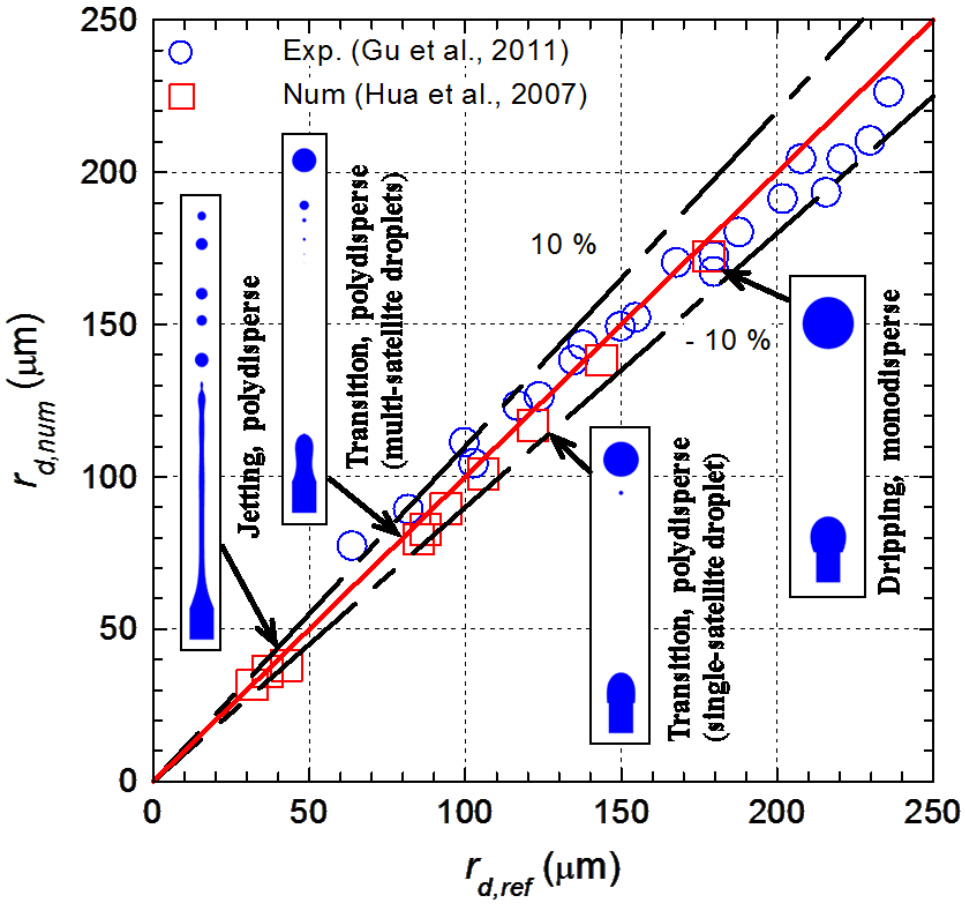


**Figure 3.2. Comparisons of present numerical calculations of droplet radii with those of Hua et al.(2007) and Gu et al. (2011) in coaxial mirotubes.**

**Table 3.2. Values of properties and parameters in listed references below for validation of the present numerical analysis.**

| **Numerical analysis - Hua, Zhang, and Lou (2007)** | | |
|---|---|---|
| Inner micro-tube radius, $R_d$ | 80 | μm |
| Inner microtube wall thickness | 20 | μm |
| Outer microtube radius, $R_c$ | 300 | μm |
| Disperse liquid flow rate, $Q_d$ | 0.98 | μl/s |
| Disperse liquid injection velocity, $\bar{u}_d$ | 0.028 | m/s |
| Continuous liquid flow rate, $Q_c$ | 15.74 – 118 | μl/s |
| Continuous liquid velocity, $\bar{u}_c$ | 0.063 – 0.47 | m/s |
| Disperse / continuous liquid viscosity, $\mu_d / \mu_c$ | 0.031 / 0.047 | Pa·s |
| Disperse / continuous liquid, $\rho_d / \rho_c$ | 1000 / 800 | kg/m$^3$ |
| Interfacial tension, $\sigma_{d,c}$ | 0.098 | N/m |
| **Experimental analysis - Gu, Kojima, and Miki (2011)** | | |
| Inner microtube radius, $R_d$ | 35 - 94 | μm |
| Inner microtube wall thickness (assumed) | 20 | μm |
| Outer micro-tube radius, $R_c$ | 235 - 260 | μm |
| Water flow rate, $Q_d$ | 0.046 | μl/s |
| Water injection velocity, $\bar{u}_d$ | 0.0017 – 0.0119 | m/s |
| Salad oil flow rate, $Q_c$ | 0.83 – 8.333 | μl/s |
| Water injection velocity, $\bar{u}_c$ | 0.004 – 0.051 | m/s |
| Water / Salad oil viscosity, $\mu_d / \mu_c$ | 0.001 / 0.0675 | Pa·s |
| Water / Salad oil density, $\rho_d / \rho_c$ | 1000 / 940 | kg/m$^3$ |
| Interfacial tension, $\sigma_{d,c}$ | 0.0393 | N/m |

processes of the dropping formation including static growth stage, necking, and detaching.

The good agreement in Figure 3.2 confirms the soundness of the present numerical methodology and the fidelity of the simulations. In next chapters 4 and 5, the results of the performed numerical analysis of co-flowing immiscible liquids in co-axial microtubes are presented and discussed. The numerical results of a parametric analysis, covering wide ranges of liquid properties and operation conditions discussed in the following chapters, are used to develop correlations for common boundaries between the dripping, transition and jetting regimes. In addition, the results of the numerical and parametric analyses are also used to develop correlation for predicting the dimensionless radius and formation frequency of monodisperse droplets.

# 4. FLOW REGIMES MAP FOR FORMING DROPLETS

The condtions leading to the formation of dispese droplets using co-flowing immiscible liquids in coaxial microtubes depends on the prevailing flow regimes. The regimes for forming disperse droplets are: dripping (or monodisperse dripping), transition (or polydisperse dripping) and jetting (Figure 2.1). Shifting from one regime to the other occurs by changing the injection velocities and physical properties of the liquids, the interfacial tension and/or the diameters of the coaxial microtubes. The resulting changes affect the sizes, formation frequency of the disperse droplets, and the boundaries between the various regimes.

This chapter presents and discusses the results of the numerical calculations simulating the processes of disperse droplets formation using co-flowing immiscible liquids. The results show the effects of changing the liquids properties and operation parameters on the prevailing flow regime of forming disperse droplets and the size and formation frequency of the droplets. In addition, the condition for boundaries between the flow regimes is identified. The investigated parameters ($\overline{u}_d$, $\overline{u}_c$, $\mu_{\mathrm{d}}$, $\mu_{\mathrm{c}}$, $R_d$, $R_d$, and $\sigma_{\mathrm{dc}}$) are varied one at a time, while keeping others at their baseline values listed in Table 4.1. The numerical results are used to generate motion picture movies to help characterize the formation dynamics; growth and break off of disperse liquid droplets in the dripping, transition and jetting regimes (Figure 2.1). A flow regimes map and dimensionless correlations of the boundaries between these regimes are developed based, on the numerical results.

**Table 4.1. Base values of properties and parameters in performed numerical simulations.**

| Parameter | Values | Units |
|---|---|---|
| Inner microtube radius, $R_d$ | 50 | μm |
| Outer microtube radius, $R_c$ | 320 | μm |
| Disperse liquid viscosity, $\mu_d$ | 0.031 | Pa·s |
| Continuous liquid viscosity, $\mu_c$ | 0.031 | Pa·s |
| Disperse/ continuous liquid density, $\rho_d / \rho_c$ | 1000 / 1000 | kg/m$^3$ |
| Interfacial tension, $\sigma_{d,c}$ | 0.02 | N/m |
| Disperse liquid rate/ velocity, $Q_d / \overline{u}_d$` | 0.243 / 0.31 | μl/s / m/s |
| Continuous liquid rate/ velocity, $Q_c / \overline{u}_c$ | 9.622 / 0.031 | μl/s / m/s |
| Microtube radius ratio, $R^*$ | 6.4 | – |
| Disperse liquid Reynolds number, $Re_d$ | 0.1 | – |
| Continuous liquid Reynolds number, $Re_c$ | 0.52 | |
| Disperse liquid Capillary number, $Ca_d$ | 0.0481 | – |
| Continuous liquid Capillary number, $Ca_c$ | 0.0481 | – |
| Remolds number ratio, $Re_d/Re_d$ | 0.1923 | |
| Disperse liquid Weber number, $We_d$ | 0.00481 | – |

## 4.1. Forming Droplets in Dripping (Monodisperse Dripping) Regime

The images in Figure 4.1 illustrate the evolution of disperse droplets during their successive stages of formation in the dripping (or monodisperse dripping) regime at 0.0256 of $Ca_c$. The images in this figure are for the following parameters: $R_d$ = 50 μm, $R_c$ = 320 μm ($R^*$ = 6.4), $\bar{u}_d$ = 0.031 m/s and $Re_d$ = 0.1, $\bar{u}_c$ = 0.0248 m/s, $Ca_c$ = 0.001 and $Re_c$ = 0.416, and $\sigma_{d,c}$ = 0.03 N/m. At these conditions, monodisperse droplets form in the dripping regime. Though the thickness of the inner microtube wall ($R_{d,o}$ - $R_d$) has a negligible effect on the disperse droplet's radius, it may affect the initial development of the disperse liquid pendent forming at the tip of the microtube.

The flat interface located initially midway inside the inner microtube (at $t$ = 0) (Figure 4.1) acquires a parabolic shape and then moves forward, driven by constant injection of the disperse liquid, to the tip of the inner microtube. When a parabolic interface emerges from the tip of the inner microtube (≤ 2 ms into the simulated transient, Figure 5.1), the combined effect of the disperse liquid's inertia and interfacial tension, $\sigma_{d,c}$, causes the parabolic interface to evolve into a disperse spherical pendent that steadily grows in size with time. This occurs in Figure 4.1 after ~4 ms from the start of the transient. As the disperse liquid pendent grows in size, the interfacial tension increasingly dominates the shape and movement of its surface. The induced viscous drag by the continuous liquid flow on the enlarging pendent droplet accelerates its forward motion, and then initiates necking close to the tip of the inner microtube (at ~62 ms in Figure 4.1). Following the pinch off of the disperse droplet occurs close to the tip of the inner microtube, a second cycle (at ~70 ms in Figure 4.1) of forming another disperse droplet begins. In Figure 4.1, the detached

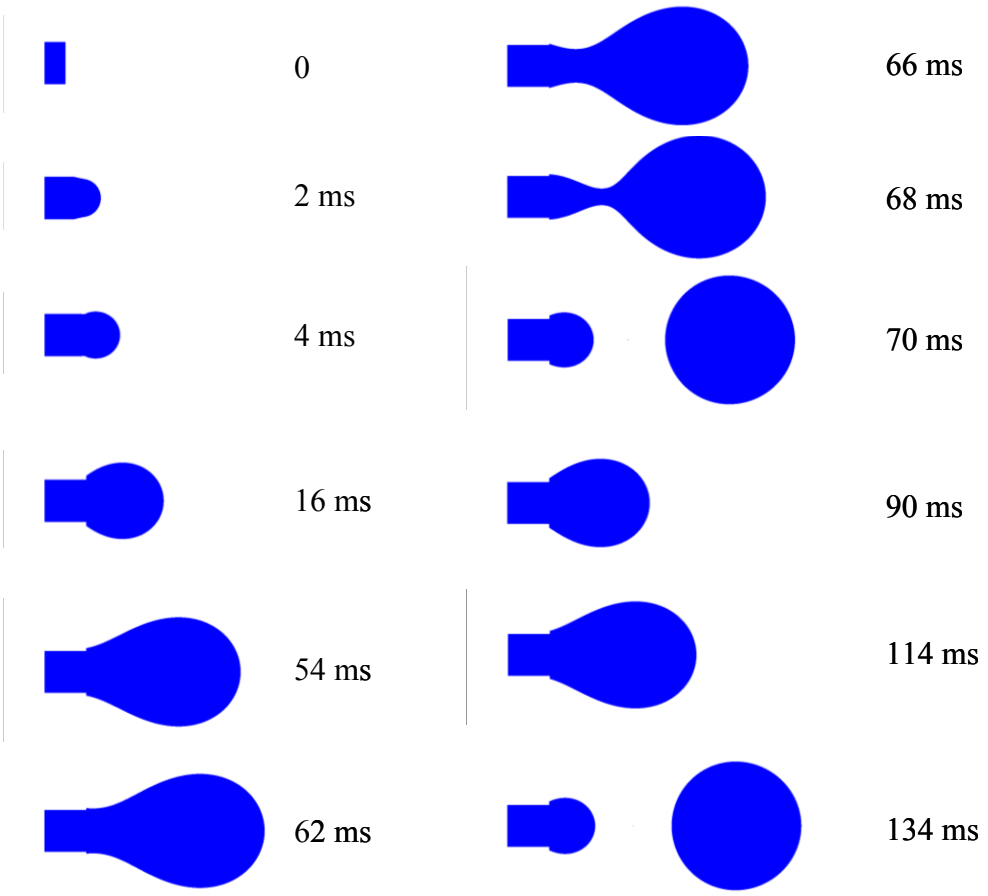


**Figure 4.1. Successive images of cyclical formation of droplet in the dripping regime ($R_d$ = 50 µm, $R_c$ = 320 µm , $\bar{u}_d$ = 0.031 m/s, $\bar{u}_c$ = 0.0248 m/s, $\mu_d$ and $\mu_c$ = 0.031 Pa·s, $\rho_d$ and $\rho_c$ = 1000 kg/m$^3$, and $\sigma_{d,c}$ = 0.03 N/m).**

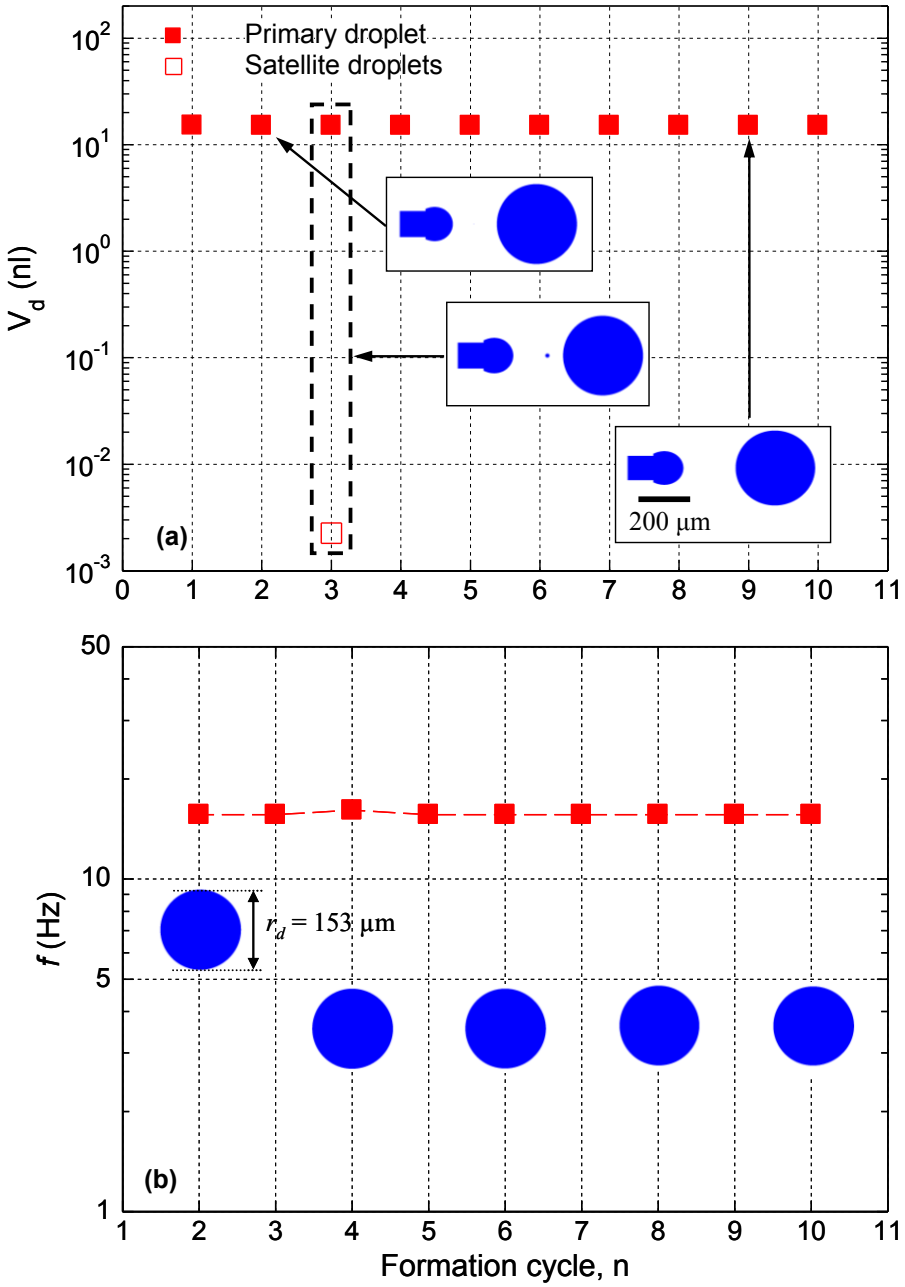


**Figure 4.2. Changes in the volume of droplet (a) and formation frequency (b) in the dripping regime ($R_d$ = 50 μm, $R_c$ = 320 μm , $\bar{u}_d$ = 0.031 m/s, $\bar{u}_c$ = 0.0248 m/s, $\mu_d$ and $\mu_c$ = 0.031 Pa·s, $\rho_d$ and $\rho_c$ = 1000 kg/m$^3$, and $\sigma_{d,c}$ = 0.03 N/m).**

droplet remains perfectly spherical and not constrained by the outer microtube wall. The forming cycle of the disperse droplets, for the conditions in Figure 4.1, repeats at a consistent frequency of 15.625 Hz, excluding the first droplet. With the fine mesh numerical grid used in the present simulations no numerical instabilities are encountered during the formation cycle of the disperse droplets, including pinch off.

Such consistency in the size and formation frequency of monodisperse droplets in the dripping regime is demonstrated in Figures 4.2a and 4.2b. These figures plot the volume and frequency of the forming droplets, respectively, for the conditions used in Figure 4.1. The disperse droplets have exactly the same size (or radius), irrespective of the formation cycle. They are perfectly spherical with an identical volume of 15.1 nl and radius, $r_d$, of 152.5 μm (Figure 4.2a). The droplets are also monodisperse, despite the formation of a single tiny satellite droplet in the third formation cycle of the simulation that is 0.015% of the volume of the primary droplet (Figure 4.2a). No other satellite droplets are formed in the rest of the simulated cycles. For all the droplets, except the first, the formation frequency is constant 15.6Hz (Figure 4.2b).

## 4.2. Forming Droplets in Transition (Polydisperse Dripping) Regime

Increasing the injection velocity of the continuous liquid, $\overline{u}_c$, from 0.0248 to 0.1085 m/s, while keeping all other parameters in Table 3.1 constant, shifts the formation of the disperse droplets from the dripping to the transition regime (Figures 4.3 and 4.4). The volume of the primary droplets decreases but their average frequency of formation increases, excluding the first droplet (Figures 4.4a and 4.4b). Increasing the injection velocity of the continuous liquid also extends a short and thin filament or *"thread"* of the disperse liquid. It extends from the exit of the inner microtube to the evolving primary

droplet at the opposite end (Figure 4.3). The disperse droplet breaks off by necking the filament under the effect of interfacial tension. Following the primary droplet's pinch off, the thin disperse filament breaks off at the exit of the disperse liquid microtube and becomes hydro-dynamically unstable. It then breaks up into one or more tiny satellite droplets, under the combined effect of interfacial tension and hydrodynamic perturbations of the surface of the filament. The total volume of the forming satellite droplets is negligibly small (< 2.5% of the primary droplet) (Figure 4.4a).

As images in Figure 4.3, the interfacial shear exerted by the continuous liquid flow at a high injection rate develops a very thin filament of the disperse liquid that extends axially, while the forming droplet is in the necking stage. This occurs in Figure 4.3 at 10.5 ms in the simulation cycle of the disperse droplet. In dripping, following the droplet's pinch off at the end of the very short disperse liquid filament, the filament retracts to the tip of the inner microtube. Shortly thereafter, another disperse droplet begins to grow into the continuous liquid co-axial flow. However, increasing the flow rate of the continuous liquid increases the filament length of the disperse liquid. This filament of the disperse liquid breaks up into satellite droplets with very small radii by the perturbation of the interface, following the primary droplet's pinch off (at ~12.6 ms in Figure 5.3). The formation of the primary and satellite droplets occurs repetitively. Therefore, the process depicted in Figure 4.3 for forming disperse liquid droplets is identified as the transition (often referred to as polydisperse dripping) regime, while the process presented in Figure 4.1 is referred to as the dripping (or monodisperse dripping) regime.

Figures 4.4a and 4.4b show the changes in the volume and formation frequency of the forming droplets in the transition regime (Figure 4.3). As shown in Figure 4.4a, the

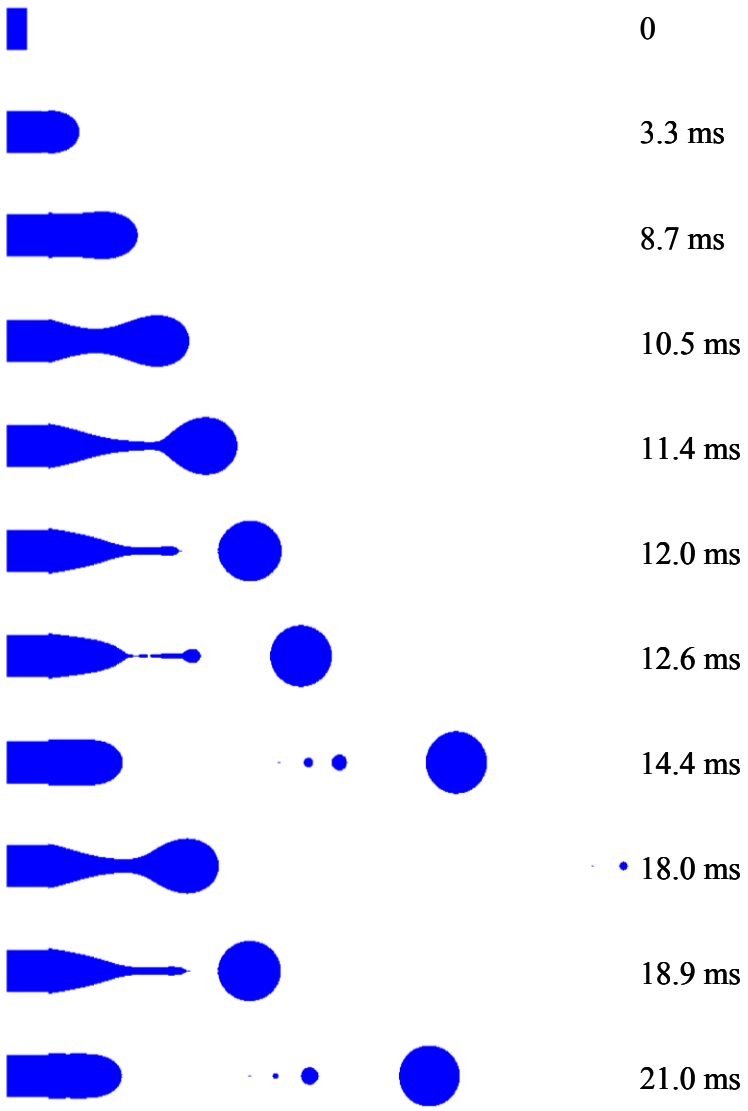


**Figure 4.3. Successive images of cyclical formation of droplet in the transition regime ($R_d$ = 50 µm, $R_c$ = 320 µm , $\bar{u}_d$ = 0.031 m/s, $\bar{u}_c$ = 0.1085 m/s, $\mu_d$ and $\mu_c$ = 0.031 Pa·s, $\rho_d$ and $\rho_c$ = 1000 kg/m$^3$, and $\sigma_{d,c}$ = 0.03 N/m).**

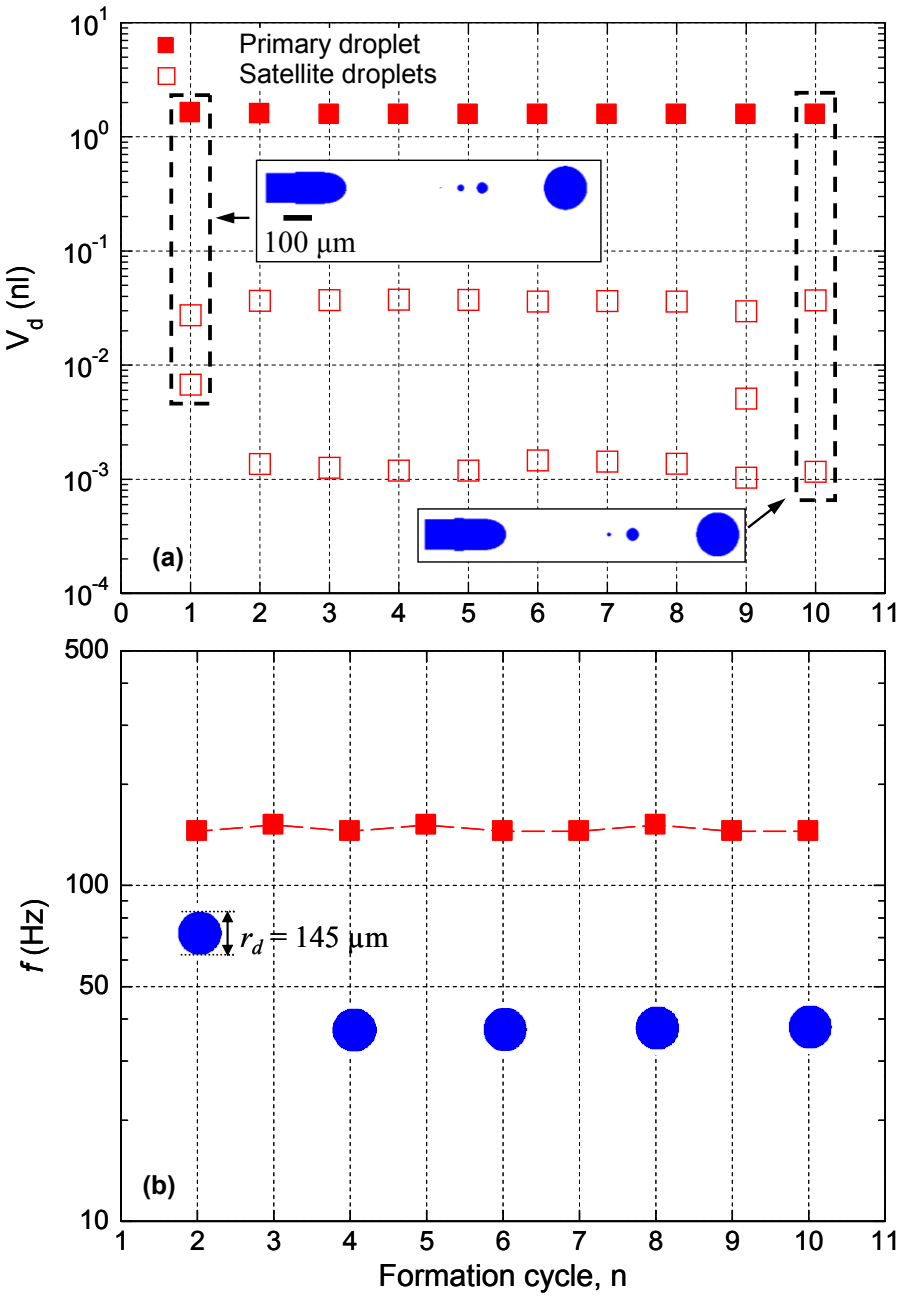


**Figure 4.4. Changes in the volume of droplet (a) and formation frequency (b) in the transition regime ($R_d$ = 50 μm, $R_c$ = 320 μm , $\bar{u}_d$ = 0.031 m/s, $\bar{u}_c$ = 0.1085 m/s, $\mu_d$ and $\mu_c$ = 0.031 Pa·s, $\rho_d$ and $\rho_c$ = 1000 kg/m$^3$, and $\sigma_{d,c}$ = 0.03 N/m).**

formation of the primary disperse droplet is associated with a couple of satellite droplets of different, but much smaller volumes. The total volume of the satellite droplets is negligibly small (< 2.5% of the primary droplet). The primary droplets are also perfectly spherical but of much smaller volume than in the dripping regime (Figure 4.2a). The volume of the primary droplet in Figure 4.4a is 1.57 nl and the corresponding radius, $r_d$ = 72.5 μm. The average formation frequency of the primary droplet in Figure 4.4b is 147.1 Hz, excluding that of the first droplet. This frequency in almost an order of magnitude higher than that calculated in the dripping regime of 15.6 Hz (Figure 4.2b). It is worthy to note that the inconsistent sizes of satellite droplets slightly affect the formation frequency of the primary droplets. The formation frequency of the primary droplet in the 2$^{nd}$ to 10$^{th}$ cycle fluctuates between 144.9 and 151.5 Hz (within 1.5 to 3 % of the average frequency).

The results presented from Figure 4.1 to 4.4 clearly demonstrate the difference between dripping (monodisperse dripping) and transition (polydisperse dripping) with satellite droplet's formation. They also prove that the formation of satellite droplets does not much affect the size of the primary droplets, but slightly changes its formation frequency.

### 4.3. Forming Droplets in Jetting Regime

Further increase in the injection velocity of the continuous liquid, $\bar{u}_c$, to 0.1116 m/s, while keeping all other parameters in Table 3.1 constant, shifts the formation of the disperse droplet to the jetting regime (Figures 4.5 and 4.6). In this regime, polydisperse droplets break off at the tip of a stable disperse liquid jet by the propagation of growing perturbations along the jet surface (hydrodynamic instability). The narrowing jet in Figure 4.5 produces droplets of inconsistent volumes, and at inconsistent frequencies.

Figure 4.5 illustrates the break-off of disperse droplets at the tip of a narrowing jet in the jetting regime. The sequential images in Figure 4.5 show that in the $6^{th}$ formation cycle (~36.6 ms), the disperse liquid starts to form a stable narrowing jet, suppressing the breakup of the satellite droplets. The length of this stable jet increases up to ~1540 μm thereafter. This stable jet does not have a constant length after being fully developed (after 52.8 ms), which implies that the size and frequency of the forming droplets is inconsistent due to the nonlinear growth of the perturbations along the interface. The changes in the volume and frequency of the forming disperse droplets are plotted in Figure 4.6a and 4.6b. The volumes of the droplets generated by narrowing jets (Figure 4.6a) are much smaller and the corresponding formation frequencies are much higher than in the transition regime. In the first 5 cycles, the volume of the produced disperse droplets, before establishing a stable narrowing jet, decreases and the formation frequency increases graduating with the number of cycles.

After the formation of a stable narrowing jet ($n \geq 6$), the average size of the disperse droplets continues to decrease and at an increasing frequency (Figures 4.6a and 4.6b). As these figures show, the disperse droplets produced by a narrowing jet are highly polydisperse. During the simulated cycles 6 - 18, the average volume of the disperse droplets oscillates between 0.198 to 0.806 nl, with an average radius of ~ 14 to 58 μm. The average formation frequency of the droplets in the last 13 cycles is 634.1 Hz, oscillating but steadily increasing from ~ 200 Hz in the 6th cycle to over 1000 Hz in the 17th cycle and ~ 900 Hz in the $18^{th}$ and last cycle simulated (Figure 4.6b).

While the results presented in Figures 4.5 and 4.6 are for a narrowing jet, those delineated in Figures 4.7 and 4.8 are for a widening jet. The values of the parameters for the

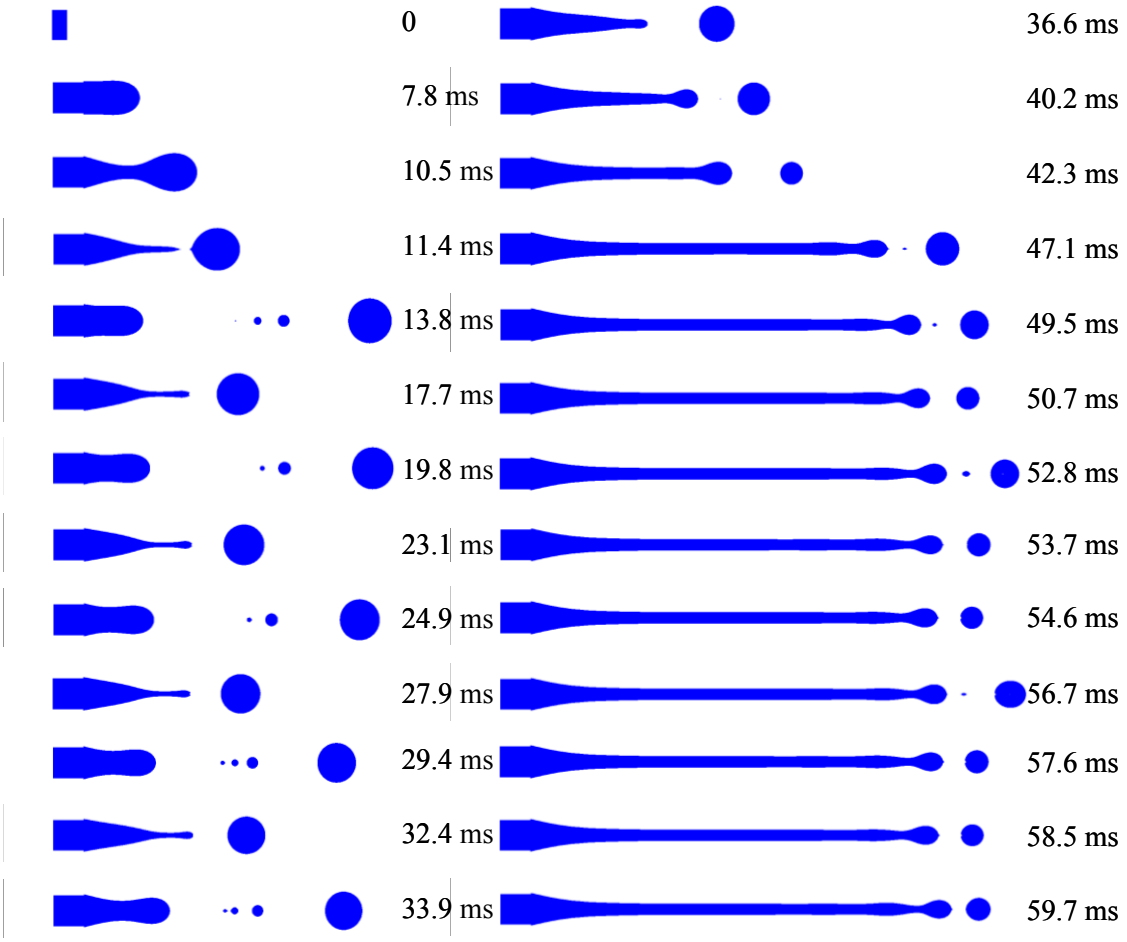


**Figure 4.5. Successive images of cyclical formation of droplet in the jetting (narrowing jetting) regime ($R_d$ = 50 µm, $R_c$ = 320 µm , $\bar{u}_d$ = 0.031 m/s, $\bar{u}_c$ = 0.1116 m/s, $\mu_d$ and $\mu_c$ = 0.031 Pa·s, $\rho_d$ and $\rho_c$ = 1000 kg/m$^3$, and $\sigma_{d,c}$ = 0.03 N/m).**

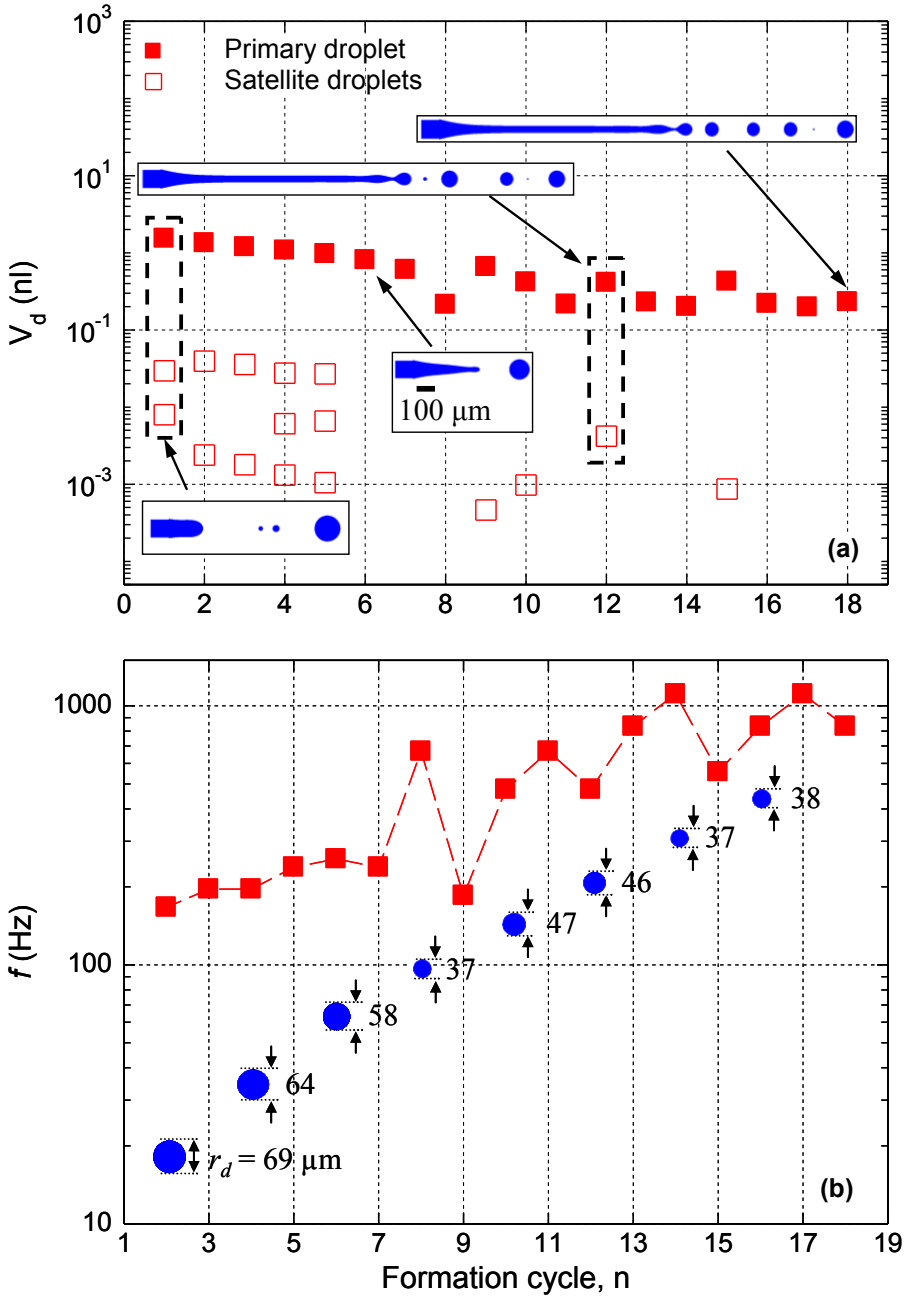


**Figure 4.6. Changes in the volume of droplet (a) and formation frequency (b) in the jetting (narrowing jetting) regime ($R_d$ = 50 μm, $R_c$ = 320 μm , $\overline{u}_d$ = 0.031 m/s, $\overline{u}_c$ = 0.1116 m/s, $\mu_d$ and $\mu_c$ = 0.031 Pa·s, $\rho_d$ and $\rho_c$ = 1000 kg/m$^3$, and $\sigma_{d,c}$ = 0.03 N/m).**

results presented in these figures are different from those for the results presented in Figures 4.5 and 4.6 for a narrowing jet. The radius of the continuous liquid microtube increased to $R_c$ = 510 μm (or $R^*$ = 10.4), the injection velocities of the continuous and disperse liquids decreased to $\bar{u}_c$ = 0.00525 m/s and $\bar{u}_d$ = 0.07 m/s, the dynamic viscosities of both liquids increased to 0.06 Pa·s, and the interfacial tension significantly decreased to $\sigma_{d,c}$ = 0.008 N/m. As for a narrowing jet, the break off of the disperse droplets at the tip of a widening jet is by growing and propagating perturbations of the interface. The results in Figures 4.7 and 4.8 demonstrate the characteristics of the disperse emulsion produced by a stable widening jet, including the volume and the formation frequency of the primary disperse droplets. Sequential images in Figure 4.7 depict the droplet formation cycles for a widening jet. The images in Figure 4.7 show the formation of a stable widening jets with a larger diameter than the disperse liquid microtube. The jet diameter increases with distance from the exit of the microtube. Unlike a narrowing jet, that takes a few cycles to become fully established, a widening jet is stable from the first cycle (~ 285 ms). The length of the widening jet increases somewhat in early cycles, reaching ~2190 μm by the 5$^{th}$ cycle (~ 945 ms) and remains unchanged thereafter (Figure 4.7).

Unlike a narrowing jet, the primary disperse droplets produced in sequential cycles by a widening jet have much larger and closer, but not identical sizes (Figure 4.8a). This is attributed to the large inventory of disperse liquid in a widening jet, compared to a narrowing jet. Consequently, the frequency of forming disperse droplets by a widening jet is significantly lower than by a narrowing jet (Figures. 4.6b and 4.8b).

As shown in Figure 4.8a, the volume of the primary droplet decreases somewhat with the number of cycles, from 98.63 nl ($r_d$ ~286.5 μm) in the 1$^{st}$ cycle to 85.57 nl ($r_d$

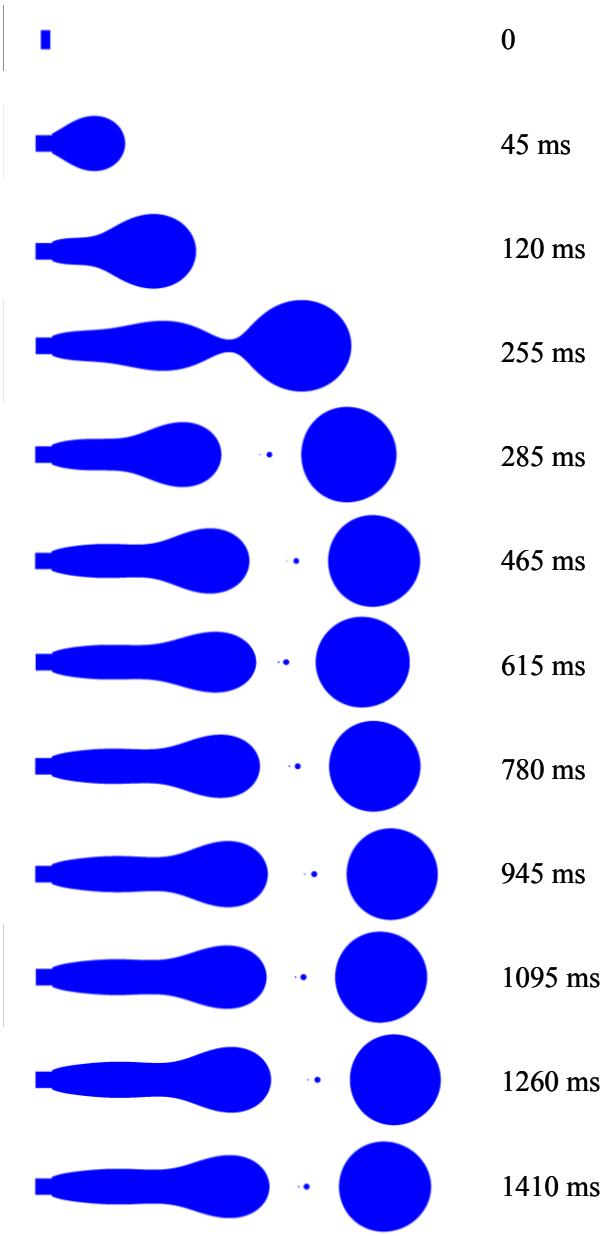


**Figure 4.7. Successive images of cyclical formation of droplet in the jetting (widening jetting) regime ($R_d$ = 50 µm, $R_c$ = 510 µm, $\bar{u}_d$ = 0.07 m/s, $\bar{u}_c$ = 0.00525 m/s, $\mu_d$ and $\mu_c$ = 0.06 Pa·s, $\rho_d$ and $\rho_c$ = 1000 kg/m$^3$, $\sigma_{d,c}$.= 0.008 N/m).**

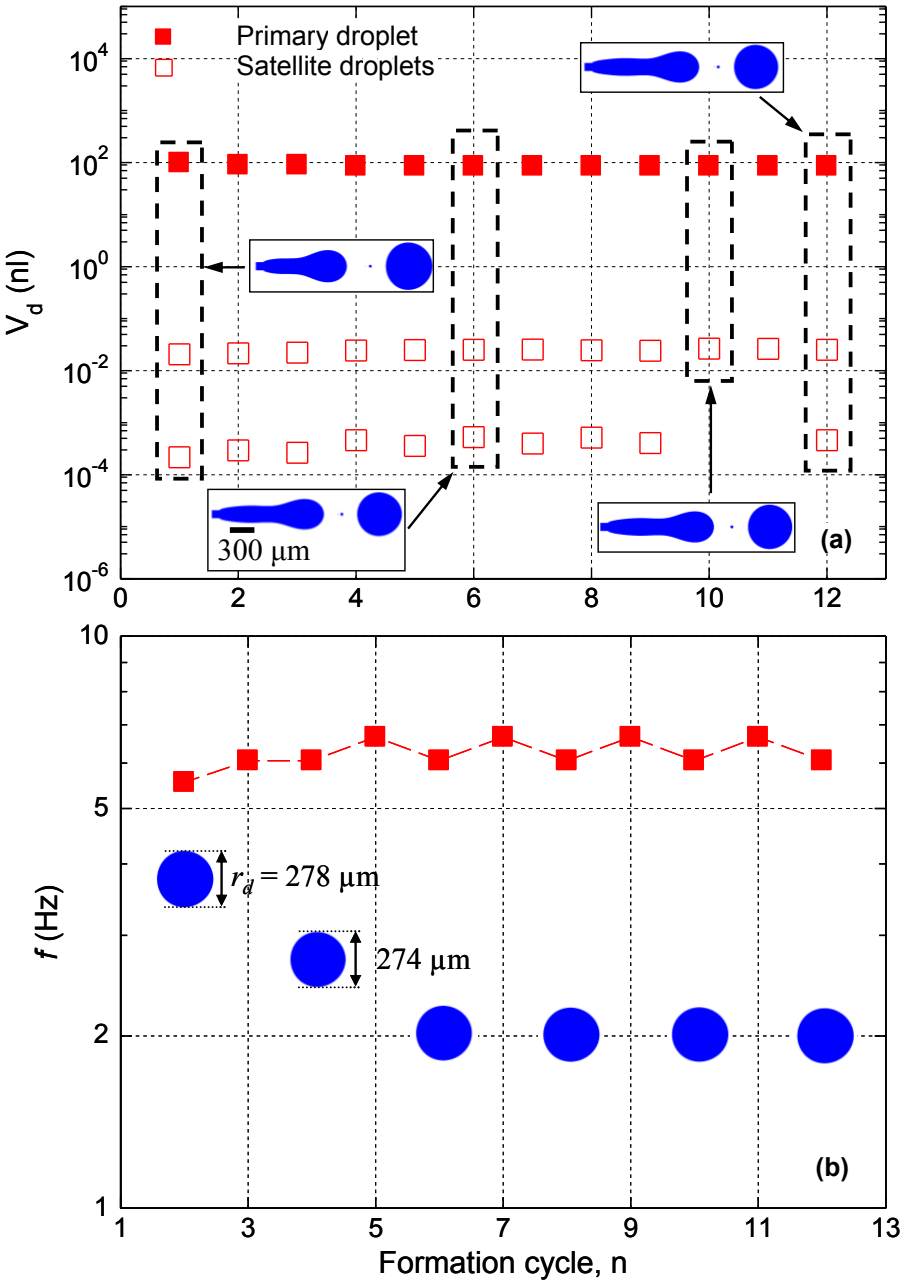


**Figure 4.8. Changes in the volume of droplet (a) and formation frequency (b) in the jetting (widening jetting) regime ($R_d$ = 50 µm, $R_c$ = 510 µm, $\bar{u}_d$ = 0.07 m/s, $\bar{u}_c$ = 0.00525 m/s, $\mu_d$ and $\mu_c$ = 0.06 Pa·s, $\rho_d$ and $\rho_c$ = 1000 kg/m$^3$, $\sigma_{d,c}$.= 0.008 N/m).**

~273.2 μm) in the 5th cycle. After this cycle, the disperse droplets have identical volumes of ~ 85.54 nl ($r_d$ ~273.2 μm). In all the simulated cycles of forming disperse droplets by a widening jet, only one or two very small satellite droplets forms after the primary droplets break off. The results in Figure 4.8b show that the break-off of the primary disperse droplets is associated with little variations in their formation frequency for the mean value (-3.3% to 12.9%). The frequency of forming disperse droplets by a widening jet is very low (Figure 4.8b), increasing from ~ 6 Hz in the 2nd cycle to ~ 7 Hz in the 5th cycle, and remains constant thereafter.

The results presented in Figures 4.1 - 4.8 are not inclusive, but only examples of the effect of the various parameters listed in Table 3.1 on the regimes and dynamics of forming disperse droplets using co-flowing immiscible liquids in coaxial microtubes. These parameters are the injection velocities, dynamic viscosities and microtubes diameters of the continuous and disperse liquids and the interfacial tension. Other combinations of these parameters could also be used to establish the different formation regimes of disperse droplets. The present numerical simulations show that the diameter of the disperse droplets, forming by a widening jet, is larger than in the dripping regime and by a stable narrowing jet. The polydispersity is absent in the dripping regime, highest in the jetting regime with a narrowing jet, but much less in the transition regime.

Figure 4.9 shows selected frames of the developed motion picture movies, based on the results of the present numerical simulations. They visually illustrate the different regimes of forming disperse droplets as well as the characteristics of the droplets. Note that the images in Figure 4.9a are for different conditions than in Figure 4.9b. The conditions for both figure are expressed in term of two dimensionless quantities, namely: the capillary

number of disperse liquid, $Ca_d$, and the product of the ratios of dynamic viscosities and injection velocities (or dynamic forces) of the continuous and disperse liquids, $\mu_r \bar{u}_r$. The shift from the dripping to the transition and from the latter to the jetting regime in Figure 4.9a is achieved by decreasing the interfacial tension (or increasing $Ca_d$), while keeping other base case parameters in Table 4.1 constant. In Figure 4.9b, the shifts among the three regimes of forming disperse droplets are accomplished by increasing the injection velocity of the continuous liquid, while keeping all other base case parameters in Table 4.1 constant. Comparing the images in Figure 4.9 indicates that widening jets form at higher $Ca_d$ (lower interfacial tension) (Figure 4.9a), while narrowing jets form at much higher interfacial tension and injection velocity of the continuous liquid (Figure 4.9b).

The following section presents and discusses the results of a parametric analysis, which investigated the effects of the liquids' properties and injection velocities, the interfacial tension, and the radii of the co-axial microtubes on the regime of forming disperse droplets. The obtained results are used to develop a flow regimes map and determine the conditions as well as develop dimensionless correlations for the common boundaries between the various regimes.

## 4.4. Parametric Analysis

In the present numerical simulations, the injection rates of the disperse liquid are very low ($We_d << 1$, $Re_d < 1$). Therefore, the dominant forces for the formation of disperse droplets are the dynamic forces of the continuous and disperse liquids and the interfacial tension. A parametric analysis is carried out by changing the various parameters ($\bar{u}_d$, $\bar{u}_c$, $\mu_d$, $\mu_c$, $R_d$, $R_c$ and $\sigma_{d,c}$) in the ranges listed in Table 3.1, and the results are presented in Figures

4.10 - 4.14. Increasing the injection velocity of the continuous liquid extends the dripping regime, shifts the formation of disperse droplets from dripping to transition and then to jetting regime (Figures 4.10a and 4.10b). The extent of the transition region increases as the interfacial surface tension increases, causing the shift from the jetting regime to occur at higher injection velocities of the continuous liquid. In Figure 4.10b, increasing the interfacial tension from 0.01 to 0.0961 increases the injection velocity of the continuous liquid for shifting from the dripping to the transition regime, from 0.0124 m/s to 0.124 m/s, and from 0.0248 m/s to 0.682 m/s for shifting from the transition to the jetting regime. Other properties that affect the boundaries between the regimes of forming disperse droplets are the dynamic viscosities of the liquids. The results of the effects of these properties are given in Figures 4.11a and 4.11b.

Figures 4.10a and 4.10b show the effects of increasing the injection velocities of disperse and continuous liquids and the interfacial tension on the prevailing regime of forming disperse droplets. The results also show the conditions for the boundaries between the three regimes of forming disperse droplets, namely: dripping, transition and jetting. The jetting regime results include both narrowing and widening jets (Figure 4.9). Figure 4.10a shows that increasing the injection velocity of either the continuous or the disperse liquid extends the dripping regime, and shifts the formation of disperse droplets to the transition, then to the jetting regime. In general, increasing the injection velocity of the disperse liquid increases the dynamic viscous and inertial forces. However, since the inlet Reynolds number of the disperse liquid in the present simulations (Table 3.1) is less than unity, the viscous force of disperse liquid is more important than its inertia for the formation of disperse droplets in the various regimes.

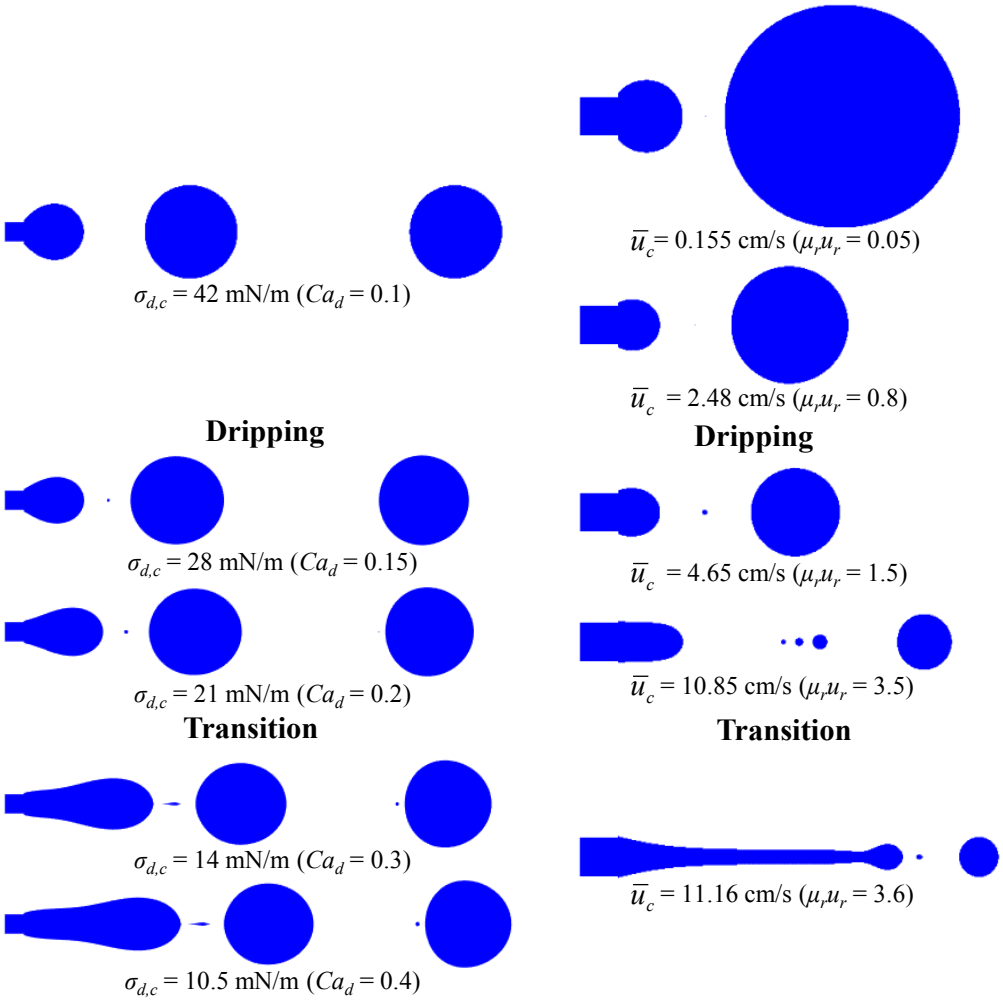


**Figure 4.9. Formation of disperse droplets in the various regimes.**

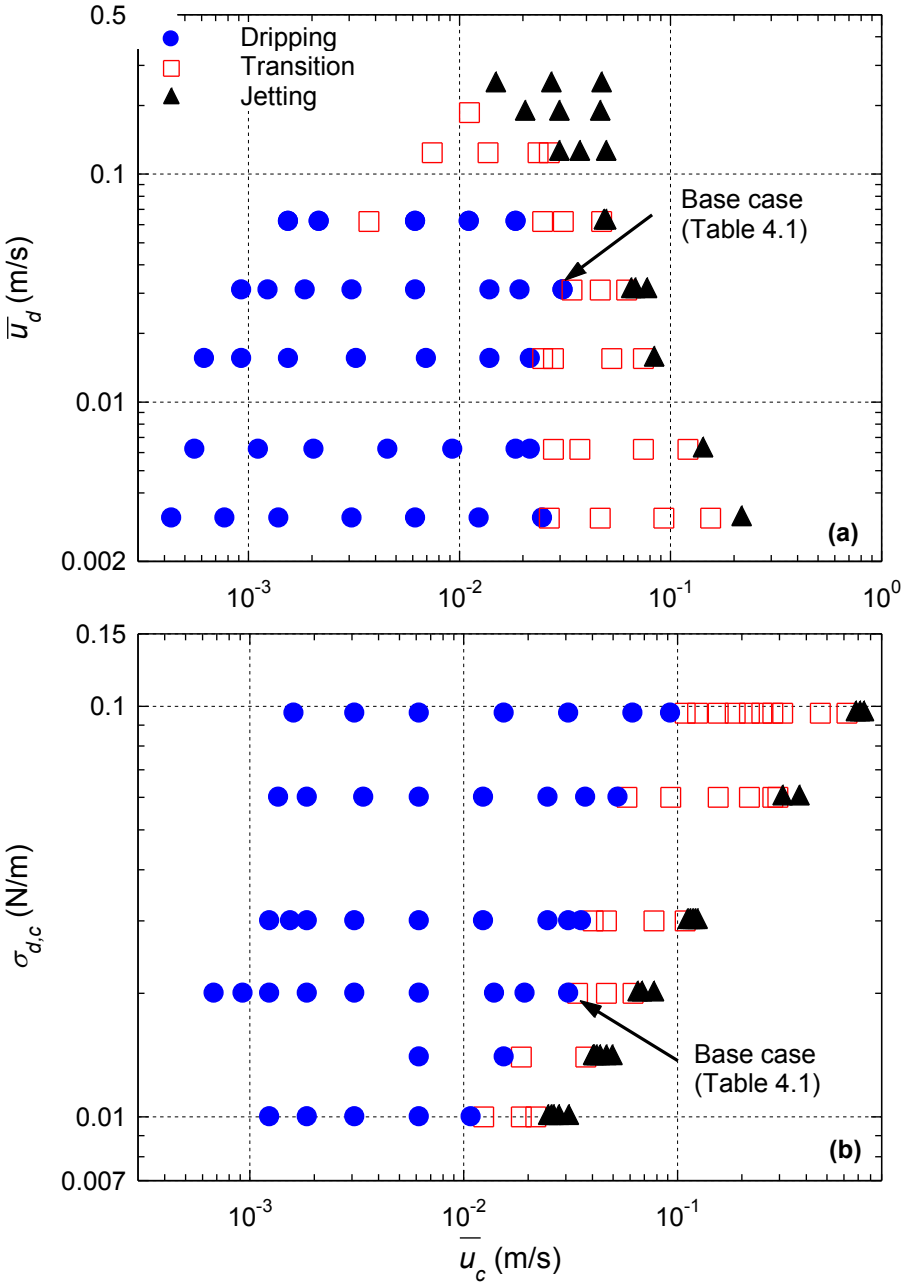


**Figure 4.10. Effects of changing injection velocities of the disperse and continuous liquids (a) and the interfacial tension (b) on the formation of disperse droplets.**

The results presented in Figures 4.11a and 4.11b confirm that increasing the injection velocity of the continuous liquid shifts the formation of the disperse droplets from the dripping to transition and then to the jetting regime. Figure 4.11a shows the boundary between the dripping and the transition regimes is independent of the dynamic viscosity of the disperse liquid < 0.031 Pa·s and that the shift from dripping to the transition regime occurs when the injection velocity of the continuous liquid, $\overline{u}_c$, is ~ 0.031 m/s. Similarly, increasing the dynamic viscosity of the continuous liquid, $\mu_c$, increases the drag exerted onthe interface between the co-flowing liquids, decreasing the continuous liquid velocity for shifting from the transition to the jetting regime (Figure 4.11b). This figure shows that the dynamic viscosity of the continuous liquid has a pronounced effect on the boundaries among the regimes of forming disperse droplets. Increasing the dynamic viscosity of the disperse liquid from 0.0078 to 0.124 Pa·s decreases the injection velocity of the continuous liquid for shifting from the transition to the jetting regime by about 69% (Figure 4.11a). The results in Figure 4.11b show that increasing the dynamic viscosity of the continuous liquid from 0.0078 to 0.124 Pa·s decreases the injection velocity of the continuous liquid for shifting from the transition to the jetting regime by about 75%. The results of the performed parametric analysis are used in the next section to develop a flow regimes map and dimensionless correlations for the boundaries between the three regimes of forming disperse droplets.

### 4.4.1. Flow Regimes Map

The compiled numerical results for the range of parameters listed in Table 3.1, including $R_d$ = 50 μm and $R^*$ = 6.4 (or $R_c$ = 320 μm), are used to develop the flow regimes

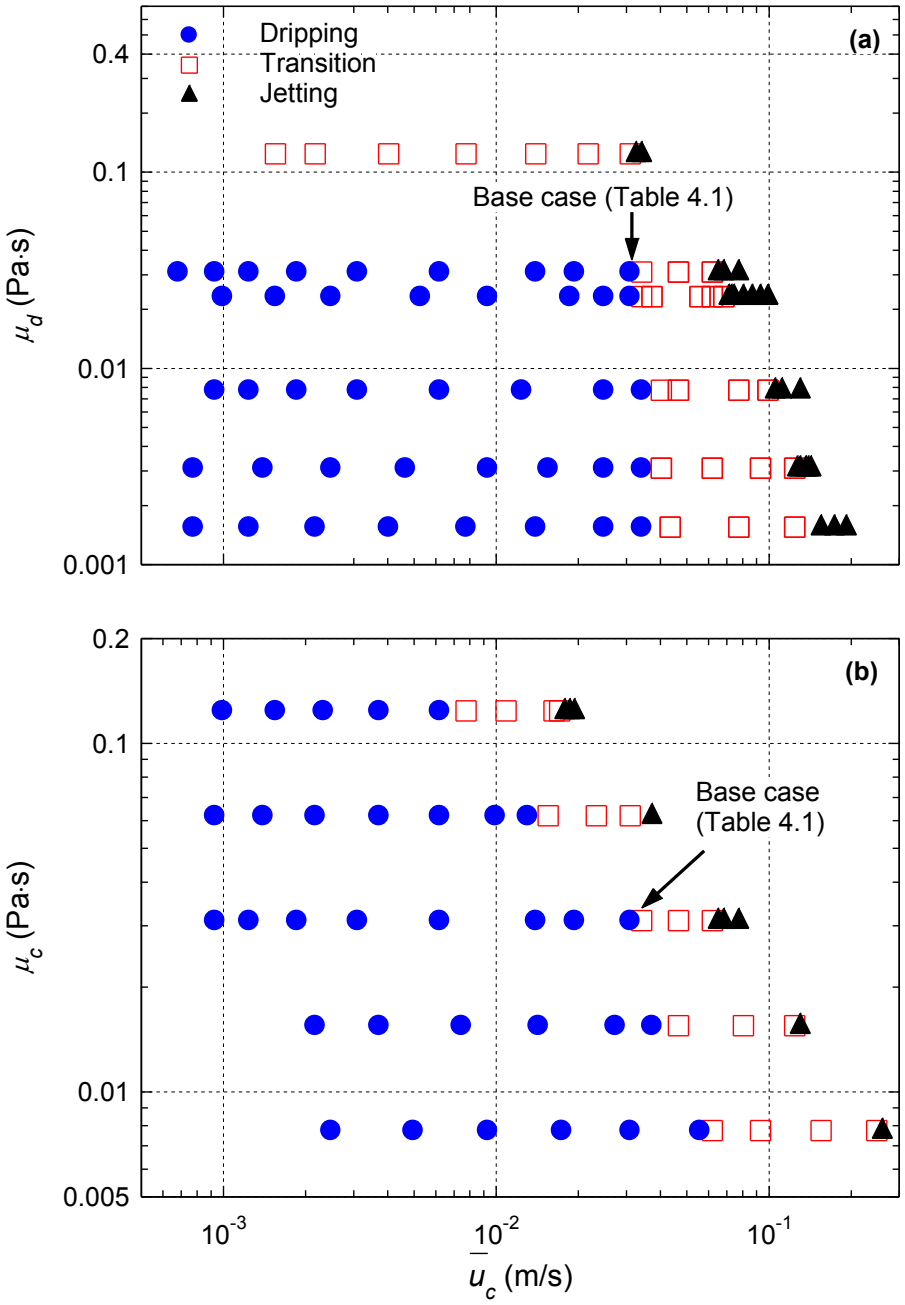


**Figure 4.11. Effects of disperse and continuous liquids' viscosities (a) and the interfacial tension (b) on the formation of disperse droplets.**

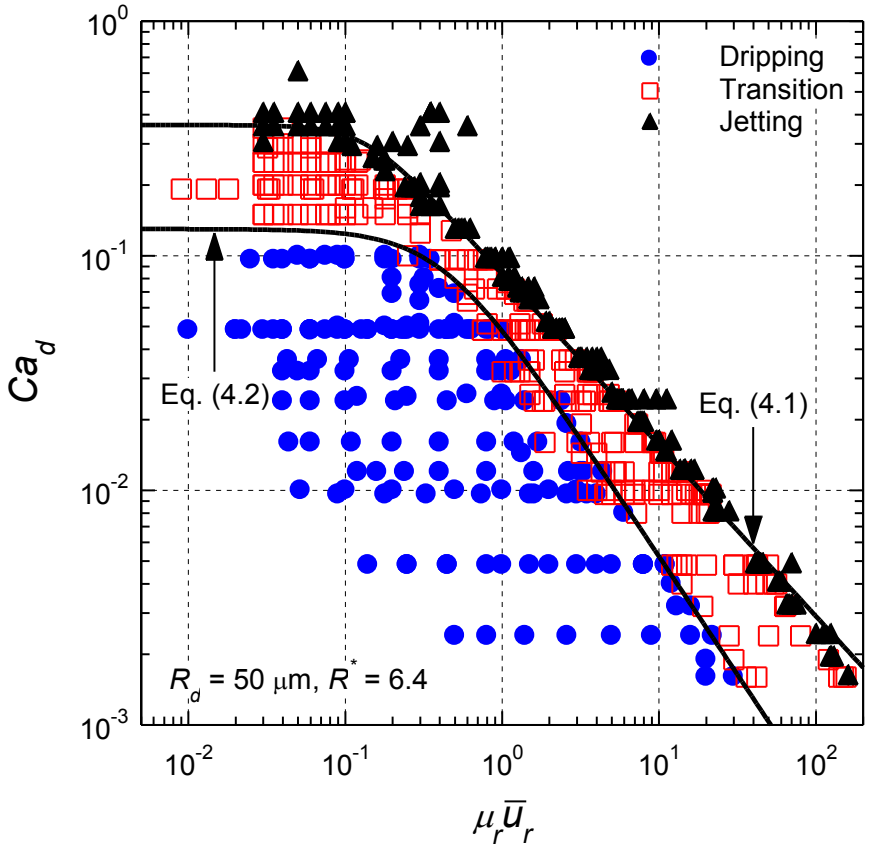


**Figure 4.12. A flow regimes map for the formation of disperse droplets in the regimes of dripping, transition and jetting.**

map in Figure 4.12. This figure plots the capillary number of disperse liquid, $Ca_d$, versus the ratio of the dynamic forces of the continuous and disperse liquids, $\mu_r \bar{u}_r$. The results for the jetting regime are indicated in Figure 4.12 by solid triangle symbols and those for the transition regime are indicated by open square symbols. The dripping regime results are represented by solid circle symbols in Figure 4.12. This figure also includes the developed dimensionless correlations (equations (4.1 and 4.2)) (Solid line) for the boundaries separating dripping, transition and jetting regimes. Figures 4.13a and 4.13b present the portions of the results in Figure 5.12, for $Ca_d \geq 0.09$ and $Ca_d \leq 0.09$, respectively.

The results in Figures 4.12 and 4.13 show that increasing the dynamic forces, $\mu_r \bar{u}_r$, moves the boundaries between the three regimes to lower values of $Ca_d$. For $Ca_d > 0.1$, transition regime dominates, extending to $Ca_d \sim 0.36$. At higher $Ca_d$ values, the jetting regime dominates. The boundary between transition and jetting regimes, at lower values of $\mu_r \bar{u}_r$, corresponds to a constant $Ca_d = \sim 0.35$. The values of the capillary number of disperse liquid at the boundary between transition and jetting regimes, $Ca_{d,TJ}$, are correlated, in terms of the dimensionless dynamic forces of the continuous and disperse liquids, $\mu_r \bar{u}_r$, and the ratio of the disperse and continuous flow microtubes radii, $R^*$, as:

$$Ca_{d,TJ} = 0.014 R^{*1.75} \left(1 + 0.01 \left(R^{*2} \mu_r \bar{u}_r\right)^{2.7}\right)^{-0.27} \qquad (4.1)$$

The first term on the right hand side of this correlation ($0.014\ R^{*1.75}$) is the highest $Ca_d$ beyond which the boundary between transient and jetting regimes is independent of $\mu_r \bar{u}_r$ (Figure 4.12).

Similarly, the developed dimensionless correlation for the boundary between transition and dripping regimes is given as:

$$Ca_{d,DT} = 0.14\left(1 + 4.63\mu_r \bar{u}_r^{\,1.74}\right)^{-0.58} \tag{4.2}$$

In this correlation, the capillary number of disperse liquid, $Ca_d$, along that boundary is independent of the microtubes radii and solely depends on the ratio of the dynamics forces for the co-flowing liquids, $\mu_r \bar{u}_r$.

Figures 4.12 and 4.13 show good agreement between the numerical results and the developed dimensionless correlations for the flow regimes boundaries, equations (4.1 and 4.2). The complete flow regimes map in Figure 4.12 incorporates a total of 574 data points, including 167 data points in the dripping regime, 237 in transition regime and 170 in the jetting regime. The boundary between the transition and jetting regimes is independent of the ratio of the dynamic forces, $\mu_r \bar{u}_r$, when $Ca_d > 0.36$ (Figure 4.13a). For these Capillary numbers, the jetting regime is dominated by widening jets (Figure 4.9a). For $\mu_r \bar{u}_r < 0.03$. The capillary number of the disperse liquid along the boundary between dripping and transition regimes is constant and equal to ~0.14. When $Ca_d < 0.35$, increasing the ratio of the dynamic forces, $\mu_r \bar{u}_r$, decreases the corresponding values of $Ca_d$ along the boundary between transition and jetting regimes (Figure 4.13b). For lower capillary numbers corresponding to $\mu_r \bar{u}_r > 0.4$ (Figure 4.13b), the width of the transition regime slightly increases with decreasing $Ca_d$, whereas the jetting regime is dominated by narrowing jets (Figure. 4.9b).

Figures 4.12 and 4.13 and the developed dimensionless correlations (equations (4.1 and 4.2)) show that the common boundaries between dripping, transition and jetting regimes strongly depend on both $Ca_d$ and $\mu_r \bar{u}_r$. The results also demonstrate the good

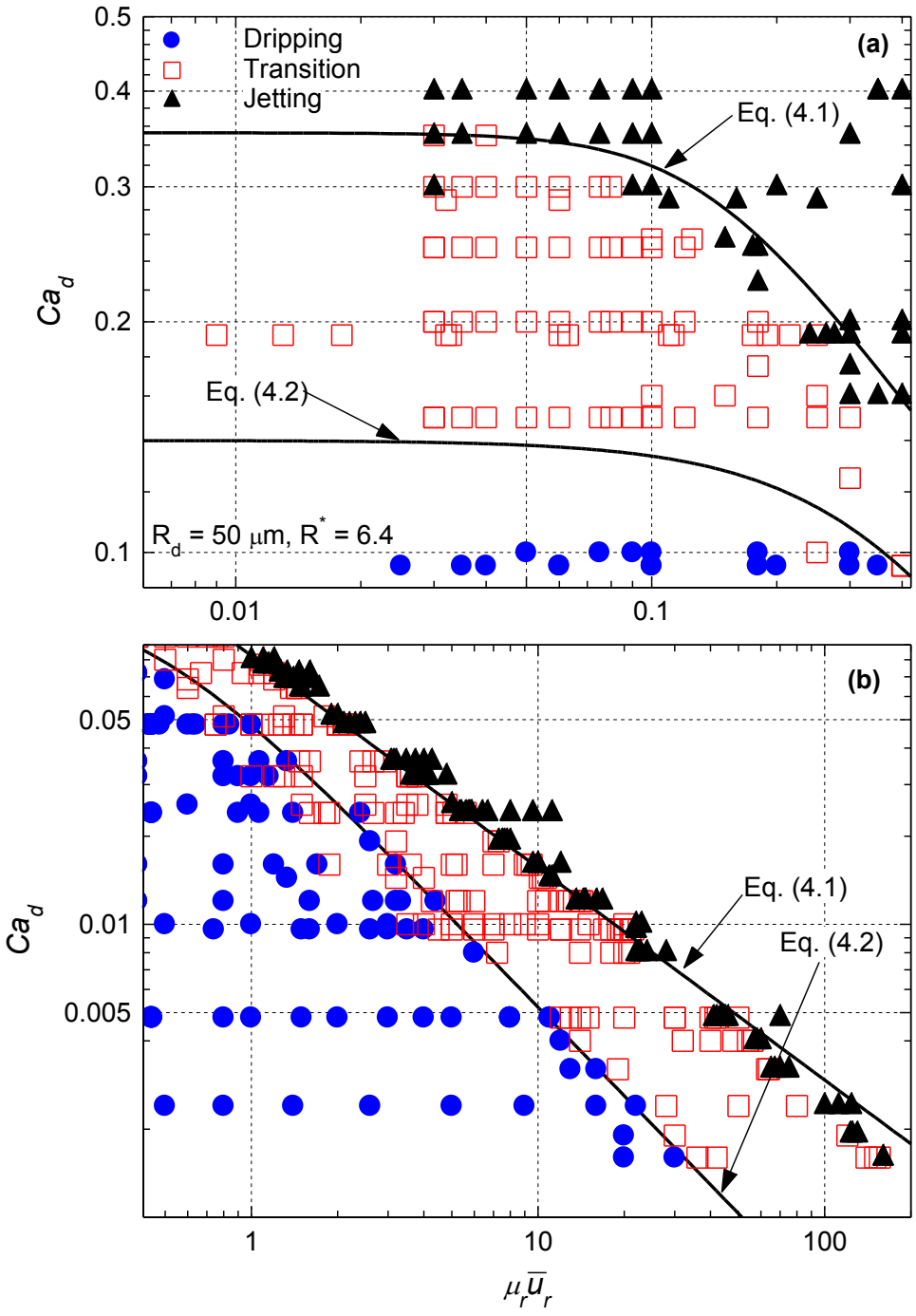


**Figure 4.13. Developed dimensionless flow regimes map: (a) at low viscous force ratios and (b) at high viscous force ratios.**

agreement between the present numerical results and the developed correlations for the the flow regimes boundaries (equations (4.1 and 4.2)) and the soundness of the developed flow regimes map.

Figures 4.12 and 4.13 also confirm that the dimensionless quantities, $Ca_{d,}$ and $\mu_r \overline{u}_r$ are the proper choices for constructing the flow regimes map. However, these dimensionless parameters do not include the ratio of the coaxial microtubes radii, which is included in equation (4.1) and omitted from equation (4.2). The boundary between transition and jetting regimes depends on the ratio of the microtubes radii, $R^*$ (equation (4.1)), while that between dripping and transition regimes is independent of $R^*$ (equation (4.2)). The effect of $R^*$ on the boundary between transition and jetting regimes is investigated and the results are presented and discusses next.

### 4.4.2. Effect of Microtube Radii

The numerical results delineated in Figure 4.14a and 4.14b are for the base case parameters in Table 4.1, but different radii of the continuous liquid microtube, $R_c$ and two radii of the disperse liquid microtube, $R_d$. Figure 4.14b shows that the boundary between the transition and jetting regimes is independent of the radius of disperse liquid microtube, $R_d$, but strongly depends on that of the continuous liquid microtube, $R_c$, or the radii ratio, $R^*$. Increasing $R^*$, moves the boundary between transition and jetting outward to higher $Ca_d$ and dynamics forces ratio, $\mu_r \overline{u}_r$ (Figure 4.14a). There is a value of $Ca_{d,}$ beyond which that boundary becomes independent of $\mu_r \overline{u}_r$; it increases with increasing $R^*$. This value is ~ 0.1 at $R^*$= 3.2, and ~ 0.8 at $R^*$ = 10.2. The shift in the boundary between transition and jetting regimes with increasing $R^*$ is much smaller at higher $\mu_r \overline{u}_r$ (> 0.3 for $R^*$= 3.2 and >

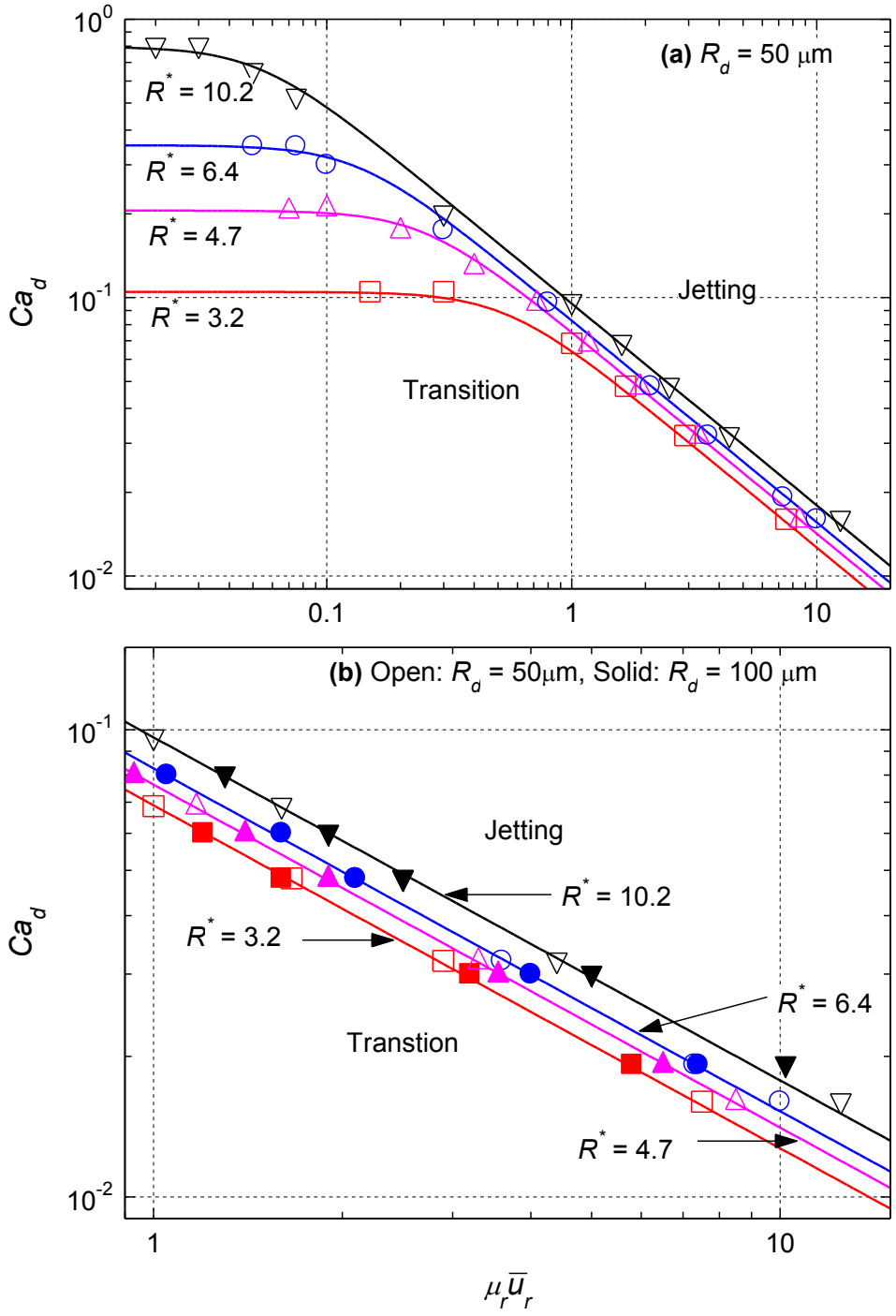


**Figure 4.14. Effect of microtubes radii on the boundary between transition and jetting regimes for forming disperse droplet.**

0.03 for $R^*$= 10.2). Increasing $R^*$, expands the transition regime toward the boundary with the jetting regime. For example, increasing $R^*$ 3 times, from 3.2 to 10.2, increases the capillary number of the disperse liquid for the boundary between transition and jetting regimes by about 8 times. Similarly, when $Ca_d$ is less than its value for the boundary between transition and jetting regimes, the ratio of dynamic forces $\mu_r \bar{u}_r$, along that boundary increases with increasing $R^*$. At $Ca_d$ = 0.016, increasing $R^*$ from 3.2 to 10.2 changes the value of $\mu_r \bar{u}_r$ for shifting from transition to jetting from 7.5 to 12.5 (Figure 4.14b). Figure 4.14b also shows that for same $R^*$, the radius of the disperse liquid microtube, $R_d$, (50 μm and 100 μm), does not affect the boundary between transition and jetting regimes. However, this boundary strongly depends on $R^*$ or the radius of the continuous liquid, $R_c$.

The effect of $R^*$ on the boundary between transition and jetting regimes is indicated by the first term of the dimensionless correlation in equation (4.1). This term ($0.014\ R^{*1.75}$) is the value of $Ca_d$ beyond which the boundary between transient and jetting is independent of $\mu_r \bar{u}_r$ (Figures 4.12 and 4.14a). When normalized relative to this term, equation (4.1) is simply rewritten as:

$$Ca^*_{d,TJ} = \left(1 + 0.01\left(R^{*2}\mu_r \bar{u}_r\right)^{2.7}\right)^{-0.27} \qquad (4.3)$$

In this equation, $Ca^*_{d,TJ}$, the normalized Capillary number of the disperse liquid = $Ca_d$/ ($0.014\ R^*$).

Figure 5.15a compares the present numerical calculations, for different ranges of the parameters in Table 3.1, with the developed dimensionless correlation (equation (4.3))

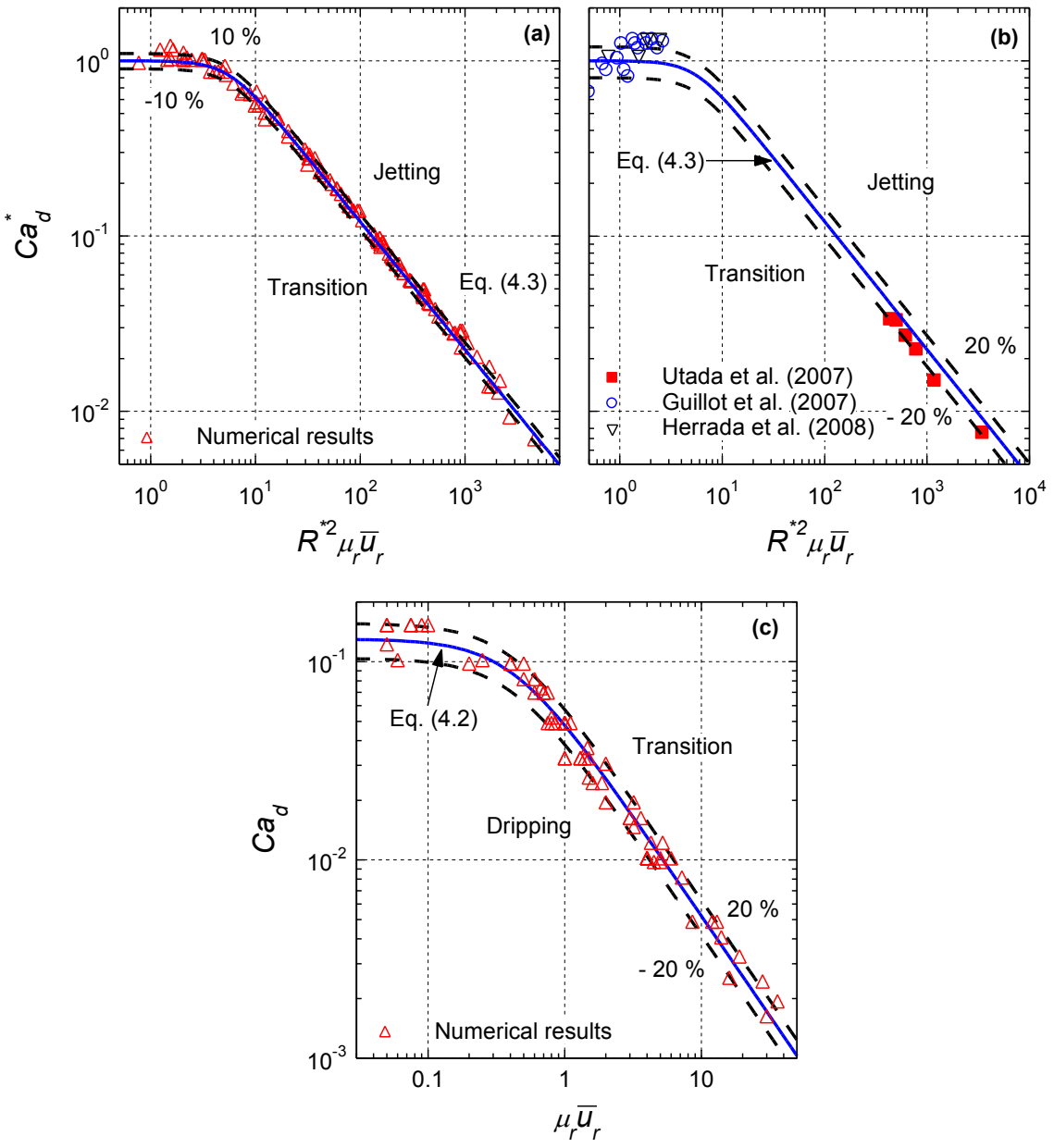


**Figure 4.15. Comparisions of present correlations for flow regimes boundaries with numerical results (a and c) and experimental results (b).**

for the boundary between transition and jetting. Figure 4.15b compares this correlation with the reported experimental results for different immiscible liquids (Utada et al., 2007; Guillot et al., 2007; Herrada et al., 2008). As Figures 4.15a and 4.15b show, equation (4.3) is in good agreement with both the present numerical and the reported experimental results, to within $\pm$ 10% and $\pm$ 20%, respectively. Figure 4.15c compares the present numerical results for $R^*$ = 3.2, 4.7, 6.4, 10.2, 12.2 with the developed dimensionless correlation for the boundary between dripping and transition (equation (4.2)). The numerical results in Figure 4.15c agree with equation (4.2) to within $\pm$20%.

Unlike the boundary between transition and jetting (Figures 4.15a and 4.15b), that between dripping and transition is independent of $R^*$ (Figure 4.15c and equation (4.2)). This is because the breakup of disperse droplets in dripping regime depends on the dynamics forces of the co-flowing liquids and the interfacial tension forces. This continues to be the case in the transition regime, where the length of disperse liquid thread (Figure 4.3) is relatively short to affect the primary droplet's break off. On the other hand, in the jetting regime the radius of the continuous liquid microtube, $R_c$, affects the length, radius and type of disperse liquid jets, and hence the droplets' formation, volume and frequency.

## 4.5. Validation of Developed Correlations

To further examine the fidelity and accuracy of the present numerical simulations, the developed correlation in equations (4.2) and (4.3) are compared in Figures 4.16a and 4.16b with the experimental data of Cramer et al. (2004), Gu et al. (2011), Utada et al. (2007), Guillot et al (2007) and Herrada et al (2008). The data of Cramer et al. is for disperse aqueous solution of κ-Carrageeenan and sunflower oil in co-axial microtubes with

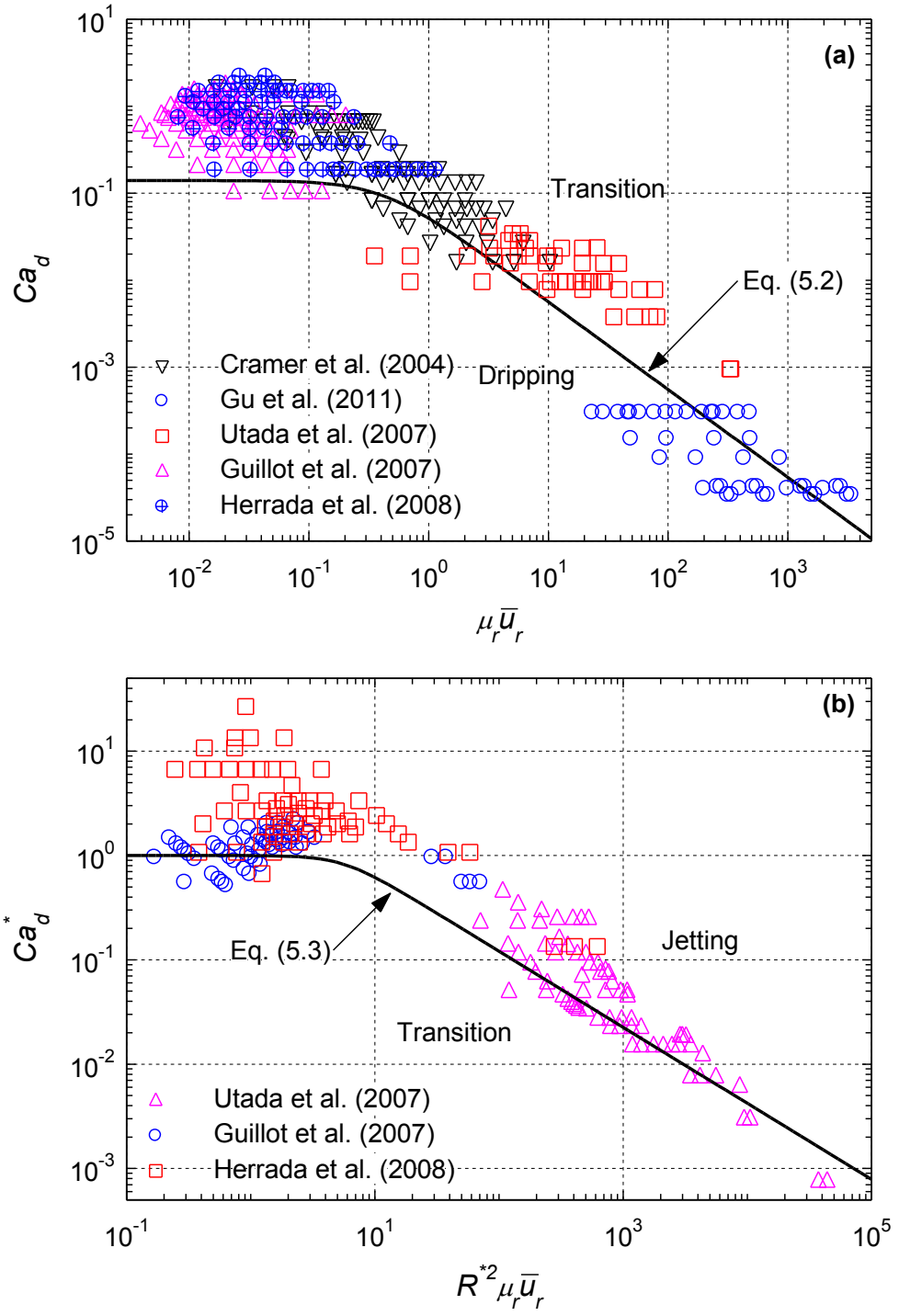


**Figure 4.16. Applications of present correlations of boundaries to reported experimental data for: (a) the dripping regime and (b) the jetting regime (b).**

$R^*$ = 44.44. The experimental data of Gu et al. is for disperse aqueous solution of sodium alginate and salad oil in co-axial microtubes with different radii ratios, $R^*$ = 2.5 - 6.7. The experimental results of Utada et al, for disperse ionized water and PDMS (Polydimethylsiloxane) oil in co-axial microtubes, are for $R^*$ = 10. The experimental data of Guillot et al. and Herrada et al. is for disperse aqueous solution of glycerine and silicone oil, with and without surfactant (Sodium Dodecyl Sulfate), in coaxial microtubes with $R^*$ = 13.8.

Figures 4.16a and 4.16b show a spread in the reported experimental data by the different investigators in the dripping, transition, and jetting regimes. Nonetheless, the developed dimensionless correlation in equation (4.2), for the boundary between dripping and transition (Figure 5.16a), is consistent with the trend displayed by the experimental data. Similarly, the correlation in equation (4.3) for the boundary between transition and jetting is consistent with the experimental data in Figure 4.16b. The spread in the experimental data in Figures 4.16a and 4.16b partially stems from the fact that researchers had focused in their experiments in the jetting regime and considered transition and dripping are a single regime, which is shown in the present analysis not to be the case.

A reported regimes map by Utata et al. (2007), based on their experimental results, identifies the boundary between transition and jetting (Figure 4.17). The figure compares their results with the present correlations (equations (4.1 and 4.2)). Utata et al. (2007) did not explicitly identify the transition regime, considering it a part of dripping regime. The present correlation (equation (4.1)) for the boundary between transition and jetting agrees well with the experimental data of Utata et al. (2007). It confirms the fidelity of the present numerical results, the solution methodology and the constituent equations used in the

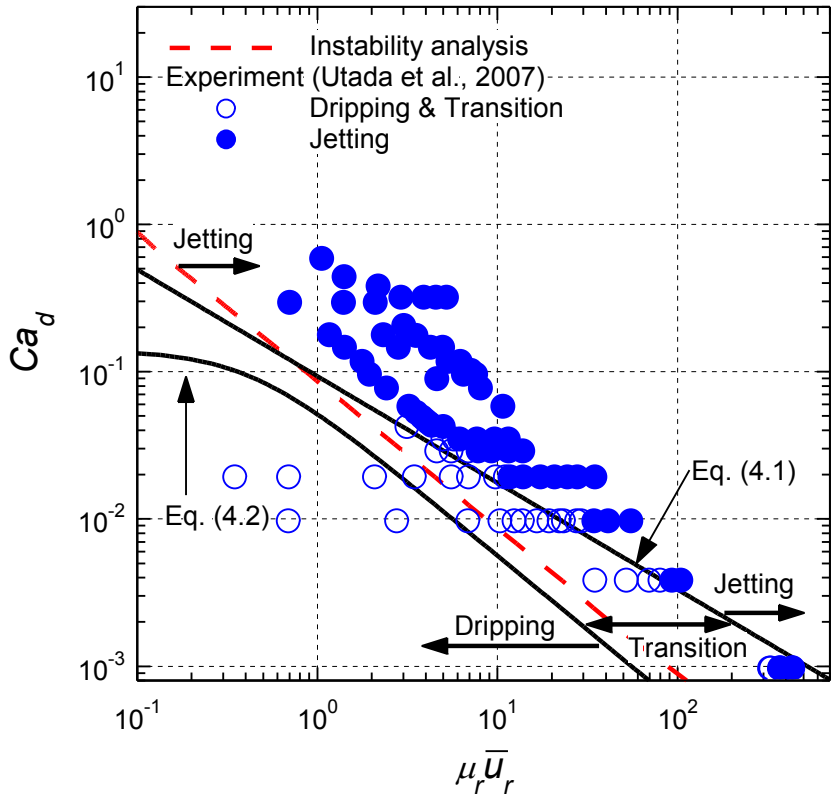


**Figure 4.17. Comparisions of developed correlations of boundaries between dripping, transition and jetting regimes, with results of instability analysis and experimental data (Utada et al., 2007)..**

numerical simulations. In addition, this agreement confirms the appropriate choices of the dimensionless parameters in equations (4.1 and 4.2) for the boundaries between dripping, transition and between transition and jetting. The linear instability analysis predictions of that boundary are consistently lower than the experimental results, but higher than the present correlation (equation (4.2)) for the boundary between dripping and transition. Linear instability analysis (Chapter 5), which neglects the inertia of co-flowing liquids and the secondary perturbation of the interface, are lower than the present correlation (equation (4.1)) for $Ca_d < 0.1$, but higher at higher values of $Ca_d$. Figure 4.17 shows that, at high dynamics force ratios, $\mu_r \bar{u}_r > 1.0$, the predicted boundary between transition and jetting by the instability analysis are lower than both the present correlations and the experimental data of Utata et al. (2007). However, the difference decreases as the dynamics force ratio decreases. For $\mu_r \bar{u}_r < 1.0$, the instability analysis predicts higher $Ca_d$ values than the present correlation (equation (4.1)) for the boundary between transition and jetting.

## 4.6. Summary

This chapter presented the numerical simulation results for forming disperse droplets using co-flowing immiscible liquids in coaxial microtubes, and the investigation effects of the injection velocities, inner diameters of microtubes and physical properties of the liquids and the interfacial tension on the characteristics and the regime of forming the droplets. The numerical results are used to develop flow regimes map and dimensionless correlations for the boundaries between the dripping, transition and jetting regimes. These correlations are in good agreement, within $\pm$10%, with the present numerical results and within $\pm$20% of the reported experimental measurements by different investigators for different immiscible liquids. These include ionized water and PDMS

(Polydimethylsiloxane) oil with $R^* = 10$, and aqueous solutions of glycerine into silicone oil flow with and without surfactant (Sodium Dodecyl Sulfate) with $R^* = 13.8$. In the next chapter, the focus is on linear instability analysis and its predictions of the boundary between transition and jetting regime.

# 5. HYDRODYANMIC LINEAR INSTABILITY ANALYSIS

In this chapter, linear instability analysis is applied to the prediction of the boundary between the transition and jetting regimes of forming disperse droplets using co-flowing immiscible liquid in coaxial microtubes. The constituent equations, assumptions and the solution methodology for the present linear instability analysis are identical to those of Herrada, G.-Calvo, and Guillot (2008), but used to compile a comprehensive data base for developing a dimensionless representation of the flow regimes boundary of interest. The governing equations are presented and the assumptions for the analysis are stated. The results of the linear instability analysis are compared to the developed dimensionless correlation in the previous chapter (equation 4.1) for the boundary between the transition and jetting regimes as well as with the reported experimental data of Utada et al. (2007) for co-flowing ionized water and PDMS oil in coaxial microtubes.

## 5.1. Introduction

More than a century ago, Rayleigh (1879 and 1892) was conducted a linear instability analysis for the breakup of a liquid jet in air. In his analysis, the displacement of the axisymmetrically perturbed interface is caused by an amplifying sinusoidal wave, $\xi = \xi_0 e^{i(kz-\omega t)}$, having a wavenumber ($k$), frequency ($\omega$) and a small initial amplitude ($\xi_0$). He had theoretically investigated the conditions for the breakup of an inviscid and viscous liquid jet. The analytical investigation assumed that an initially unperturbed surface of infinitely long jet could become unstable due to the growth of linear perturbations along the jet surface with time.

Tomotika (1935) extended Rayleigh's instability analysis to co-flowing immiscible liquids by considering the effect of the continuous liquid viscosity. Rayleigh (1879 and 1892) and Tomotika (1935) used real and complex numbers for a sinusoidal wave function, $e^{i(kz-\omega t)}$, where $k$ is a real number, the frequency is a complex number ($\omega = \omega_r - \omega_i i$ ). The sinusoidal wave function of the surface perturbations can be expressed as: $e^{\omega_i t} e^{i(k z - \omega_r t)}$ . This work has been the foundation of recent development and application of linear instability analysis to co-flowing immiscible liquids in coaxial microtubes.

Hydrodynamic instability analysis has been used to predict the conditions for the jetting regime for forming disperse droplets. This is done by considering the spatial and temporal growth of the amplitude of a surface perturbation (Keller, Rubinow, and Tu, 1973; Leib and Goldstein, 1986a and 1986b; Huerre and Monkewitz, 1990; Saarloos, 1988, 2003; O'Donnel, Chen, and Lin, 2001; Guillot et al., 2007; Guillot, Colin, and Ajdari, 2008; Herrada, G.-Calvo, and Guillot, 2008). The analysis considers formation of a disperse droplet is the result of the superimposed waves. It states that the exponential amplitude growth of the interface (or surface) perturbations depends on the imaginary parts of both the frequency and the wave number ($k = k_r + k_i$, and $\omega = \omega_r + \omega_i$). Thus, the amplitude of the interface perturbation increases exponentially, not only with time, but also with axial location along the interface separating the disperse and continuous liquids (Figure 5.1). According to the linear instability theory, the breakup of a disperse droplet from a stable disperse liquid jet could be caused by either an absolute or a convective instability, depending on the spatial and temporal growth of the amplitude. In the absolute instability, interface disturbances grow and propagate upstream, eventually causing a pinch-off the disperse droplet at or close to the exit of the inner microtube (Figure 2.1a). On the other

hand, the breakup of disperse droplets at the far end of a stable liquid jet is caused by convective instability. The preferential downstream propagation of growing surface perturbations for convective instability eventually pinches off the disperse droplets at the tip of a long disperse-liquid jet (Figure 2.1c). Guillot et al. (2007), Guillot, Colin, and Ajdari (2008), and Herrada, G.-Calvo, and Guillot (2008) analytically derived the dispersion relation between the complex frequency and the wave number in the creeping flow approximation that the inertial force of the liquids flow is negligibly small compared with its viscous force.

In their linear instability analysis, Guillot et al. (2007) radially averaged the flow and the perturbation of the co-flowing liquids and neglected their inertia. The results of their instability analysis generally agree with flow regimes maps by plotting the flow rate of the disperse versus that of continuous liquids. At low flow rates of the disperse liquid, the predicted flow rates of the continuous liquid by the linear instability analysis at the boundary between transition and jetting are much higher than their experimental results. The results and flow map of Guillot et al. (2007) is of limited use due to the absence of representative dimensional quantities to extent the validity of results to other liquids. The experiments of Guillot et al. (2007) employed disperse aqueous solution of 50wt% glycerin and silicon oil as the continuous liquid. These liquids have viscosities of 55 mPa.s and 235 mPa.s. The radii of the capillaries for injecting the continuous and disperse liquids varied from 20-50 μm and 200-500 μm, respectively.

Herrada et al. (2008) have developed an axisymmetric instability model, similar to that of Guillot et al (2007), but accounted for the disperse and continuous liquids' inertia. They considered 3-D perturbed liquid flows and compared the results of their instability

analysis with their experiment. They developed a flow regimes map in terms of the flow rate of liquids similar to Guillot et al. (2007). The predicted flow rates of the continuous liquid by the instability analysis, only high flow rate of the disperse liquid, agree with the experimental results and not formulating the flow regimes map in terms of applicable dimensionless quantities, limit the applicability of their results. In their experiments, Herrada et al. (2008) varied the diameter of disperse liquid microtube from 40-100 μm and that of the continuous liquid microtube was either 550 or 860 μm. This experiments used three pairs of disperse and continuous liquids (water with a viscosity of 1.0 mPa.s and hexadecane with a viscosity of 3 mPa.s, water-glycerin solution with a viscosity of 55 and silicone oil with a viscosity of 235 mPa.s, and water-glycerin solution with a viscosity 650 mPa.s and silicone with a viscosity of 235 mPa.s). They controlled the interfacial tension in the experiments by adding sodium dodecyl sulfate to the aqueous solutions and Span-80 to the hexadecane.

Utada et al. (2007) and Castro-Hernandez et al. (2009) have introduced a flow regimes maps to characterize the boundary between the dripping and jetting regimes, assuming the transition regime is a part of the dripping regime (Figure 2.1b). These flow regimes map are based on the capillary number of the continuous liquid, $Ca_d$, and the Weber number of the disperse liquid, $We_d$. When the exerted viscous and inertial forces of the co-flowing immiscible liquids on the interface outweigh that of interfacial tension, a disperse-liquid jet forms. Narrowing jets (Figure 2.1) occur when the viscous shear of the continuous liquid helps overcoming the effect of the interfacial tension. On the other hand, widening jets (Figure 2.1) occur when the viscous shear of the disperse liquid increases. The inertial force disperse liquid is negligibly small ($Re_d < 1$).

Castro-Hernadez et al. (2009) have conducted experiments to further investigate the criteria of Utada et al. (2007) for the transition from the dripping to the widening jetting regime. However, they did not perform instability analysis to predict the boundary for the jetting regime. Their results indicated that such transition occurs at lower a Weber number of the disperse liquid, $We_d$, than indicated by Utada et al. (2007). Castro-Hernandez et al. (2009) confirmed that only when Reynolds number of disperse liquid $Re_d > 1.0$, Weber number, $We_d$, could be used to indicate the shift into the jetting regime.

To simplify the procedures complex mathematical formulations for an analytical application of the linear instability to predicting the boundary for the jetting regime, several assumptions were made. These include neglecting higher order perturbations of the interface, creeping flow condition, and neglecting the radial component of the interface perturbations.

Considering the transition regime as a part of the dripping regime, the linear instability analysis has been used to predict the boundary between the dripping and jetting regimes. The next section presents the constituent equations for linear instability, initial and boundary conditions, and the dispersion relation for predicting this boundary.

## 5.2. Hydrodynamic Instability Analysis

The hydrodynamic analysis treats the instability of the interface between co-flowing immiscible liquids in co-axial microtubes. The disperse flow in the form of an initially cylindrical jet. This analysis, based on the evolution of normal mode perturbations of the interface (Figure 5.1), predicts the conditions for the break up of disperse droplets at the tip of the jet. The analysis assumes an infinite cylindrical thread of the disperse liquid as "*a basic flow*" in a coaxial flowing continuous liquid and treats the perturbed interface

with the linear perturbation equation (Figure 5.1). The initial interface of the basic flow grows or decays depending on the hydrodynamic drag and inertia forces of the co-flowing liquids and the interfacial tension. The growth and decay of the perturbed interface is characterized by traveling linear waves ($e^{i(kz-\omega t)}$).

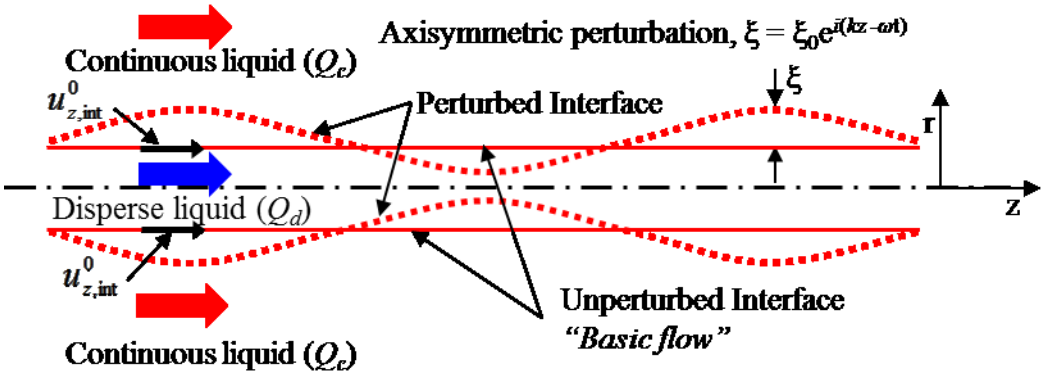


**Figure 5.1. A schematic of the growth of propagating perturbations along the surface of disperse liquid jet in a co-flowing continuous liquid.**

The hydrodynamic analysis examines the stability of the interface, using commercial algebra software, Mathematica 8.0, for solving the constituent equations and the dispersion relation. This analytical approach predicts the conditions for forming a stable jet and the break up disperse droplets in the jetting regime. The perturbed velocity and pressure of the basic disperse liquid flow are expressed as:

$$u_n = u_n^0 + u_n', \tag{5.1a}$$

$$p_n = p_n^0 + p_n', \tag{5.1b}$$

$$\kappa = \kappa' + \kappa^0 = \kappa' - \frac{1}{r_j^0}. \tag{5.1c}$$

In these equations, $u_n^0$ and $p_n^0$ are the velocity and the pressure vector of the basic flow, $u_n'$ and $p_n'$ are the vectors for the perturbations in the velocity and the pressure, respectively,

and $\kappa^0$ and $\kappa'$ are the basic curvature and the induced perturbation in the curvature of the interface between the co-flowing disperse and continuous liquids (Figure. 5.1).

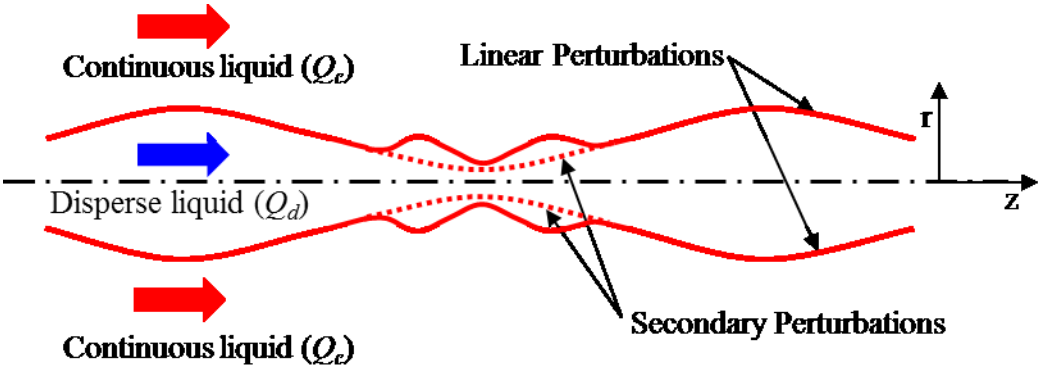


**Figure 5.2. Schematic sketch of the growth of propagating linear and secondary perturbations along the surface of disperse liquid jet in a co-flowing continuous liquid.**

The momentum balance and continuity equations of the coaxial flowing immiscible liquids, equations (3.1 and 3.2), can be expressed in terms of the basic and perturbation quantities, by substituting for the velocity and pressure of the flows using equations (5.1a - 5.1c). The interfacial tension force term in equation (3.2) is one of the boundary conditions in this analysis. The interfacial tension is kept constant, which is not applicable in the case of added surfactant to the disperse liquid. The gradient of the surfactant along the interface would stimulate Marangoni convection, altering the results and complicating the linear instability analysis. For simplicity, the present analysis also neglects the effect of the secondary perturbation and radial velocity components of the interface (Figure 5.2). These assumptions, although simplify the problem statement for obtaining a closed form analytical solution, could affect the predictions of the boundary between transition and jetting regimes. The perturbations along the disperse liquid jet surface are characterized by

a linear wave function. The next section presents and discusses the governing equations and boundary conditions for implementing the hydrodynamic linear instability analysis.

### 5.2.1. Governing Equations and Boundary Conditions

The continuity and the momentum balance equations of the co-flowing liquids are:

$$\nabla \cdot u_n' = 0 \tag{5.2}$$

$$\rho_n \frac{\partial u_n'}{\partial t} + \rho_n \left( u_n' \cdot \nabla u_n^0 + u_n^0 \cdot \nabla u_n' + u_n' \cdot \nabla u_n' \right) = -\nabla p' + \mu_n \nabla^2 u_n' + \rho_n g \tag{5.3}$$

The radial location of the interface in the flow domain, $r_j$, and the perturbed velocities and pressures of the continuous and disperse are expressed in cylindrical coordinates ($r$, $z$). The initial interface of the basic flow grows or decays depending on the hydrodynamic drag and inertial forces induced from the liquids flows and the interface tension force. The radial location of the interface in the flow domain, $r_j$, and the perturbed velocities and pressures of the continuous and disperse liquids are expressed in cylindrical coordinates ($r$, $z$) as:

$$\begin{aligned} r_j(z,t) &= r_j^0 + \xi\, e^{i(kz-\omega t)} \\ u_n'(r,z,t) &= \hat{u}_n(r)\, e^{i(kz-\omega t)} \\ p_n'(r,z,t) &= \hat{p}_n(r)\, e^{i(kz-\omega t)} \end{aligned} \tag{5.4}$$

In these equations, $r_j^0$ is the radial location of the interface of the basic disperse liquid flow, $k$ is the wave number, $\omega$ is the frequency, and $\xi$ is the small initial amplitude of the perturbed interface ($\xi << 1$) (Figure 5.1).

Equation (5.4) is substituted into equations (5.2) and (5.3) and the resulting equations are linearized by neglecting the squares and dot product of the perturbed velocity components as well as the gravity force. The obtained momentum balance and continuity equations for the co-flowing immiscible liquids can be expressed as:

(a) Momentum balance equations in the radial coordinate, *r*:

$$-\rho_n \omega i \hat{u}_{r,n} + \rho_n k i u^0_{z,n} \hat{u}_{r,n} = -\frac{\partial \hat{p}_n}{\partial r} + \mu_n \left( \frac{1}{r} \frac{\partial}{\partial r} \left( r \frac{\partial \hat{u}_{r,n}}{\partial r} \right) - k^2 \hat{u}_{r,n} - \frac{\hat{u}_{r,n}}{r^2} \right) \tag{5.5a}$$

(b) Momentum balance equations in the axial coordinate, *z*:

$$-\rho_n \omega i \hat{u}_{z,n} + \rho_n k i u^0_{z,n} \hat{u}_{z,n} + \rho_n \hat{u}_{r,n} \frac{\partial u^0_{z,n}}{\partial r} = -ik\hat{p}_n + \mu_n \left( \frac{1}{r} \frac{\partial}{\partial r} \left( r \frac{\partial \hat{u}_{z,n}}{\partial r} \right) - k^2 \hat{u}_{z,n} \right) \tag{5.5b}$$

(c) Continuity equations:

$$ik\hat{u}_{z,n} + \frac{1}{r} \frac{\partial \left( r\hat{u}_{r,n} \right)}{\partial r} = 0 \tag{5.6}$$

The creeping flow approximation omits the inertial terms on the left hand side of the momentum balances equations (5.5a and 5.5b). The simplified momentum balance equations, expressed in a dimensionless form are given as.

$$-\frac{\partial \hat{p}^*_n}{\partial r^*} + \frac{\mu^*_n}{\mathrm{Re}_{\mathrm{int}}} \left( \frac{1}{r^*} \frac{\partial}{\partial r^*} \left( r^* \frac{\partial \hat{u}^*_{r,n}}{\partial r^*} \right) - k^{*2} \hat{u}^*_{r,n} - \frac{\hat{u}^*_{r,n}}{r^{*2}} \right) = 0 \tag{5.7a}$$

$$-ik^* \hat{p}^*_n + \frac{\mu^*_n}{\mathrm{Re}_{\mathrm{int}}} \left( \frac{1}{r^*} \frac{\partial}{\partial r^*} \left( r^* \frac{\partial \hat{u}^*_{z,n}}{\partial r^*} \right) - k^{*2} \hat{u}^*_{z,n} \right) = 0 \tag{5.7b}$$

Similarly, equation (5.6) is expressed as:

$$ik^{*}\hat{u}^{*}_{z,n}+\frac{1}{r^{*}}\frac{\partial\left(r^{*}\hat{u}^{*}_{r,n}\right)}{\partial r^{*}}=0 \tag{5.8}$$

Equation (5.4), expressed in dimensionless form is given as:

$$\begin{aligned} r_j^{*}(z,t) &= 1+\xi\, e^{i\left(k^{*}z^{*}-\omega^{*}t^{*}\right)} \\ u_n'^{*}(r,z,t) &= \hat{u}_n{}^{*}(r)\, e^{i\left(k^{*}z^{*}-\omega^{*}t^{*}\right)} \\ p_n'^{*}(r,z,t) &= \hat{p}_n{}^{*}(r)\, e^{i\left(k^{*}z^{*}-\omega^{*}t^{*}\right)} \end{aligned} \tag{5.9}$$

The axial and radial perturbation velocities, expressed in terms of the stream-function, $\psi$, are given as:

$$\hat{u}^{*}_{z,n}=\frac{1}{r^{*}}\frac{\partial}{\partial r^{*}}\left(r^{*2}\psi_n\right) \tag{5.10a}$$

and,

$$\hat{u}^{*}_{r,n}=-ik^{*}r^{*}\psi_n \tag{5.10b}$$

Substituting these equations, which satisfy the continuity equations (5.8), and eliminating the perturbed pressure, the perturbed flow field gives the following expressions for the stream-functions of the disperse and continuous liquid flows, as:

(a) Disperse liquid:

$$\begin{aligned} \psi_d = \frac{1}{r^{*}}\{&C_1I_1(k^{*}r^{*})+C_1I_3(k^{*}r^{*})+C_2K_1(k^{*}r^{*})+C_2K_3(k^{*}r^{*})\} \\ &+C_7I_0(k^{*}r^{*})+C_8K_0(k^{*}r^{*}) \end{aligned} \tag{5.11a}$$

(b) Continuous liquid:

$$\begin{aligned} \psi_c = \frac{1}{r^{*}}\{&C_3I_1(k^{*}r^{*})+C_3I_3(k^{*}r^{*})+C_4K_1(k^{*}r^{*})+C_4K_3(k^{*}r^{*})\} \\ &+C_5I_0(k^{*}r^{*})+C_6K_0(k^{*}r^{*}) \end{aligned} \tag{5.11b}$$

In these equations, $C_1 - C_8$ are arbitrary constants. The perturbed radial velocity and the gradient of the axial perturbed velocity of the disperse liquids along the centerline of the

flow domain ($r^*$ = 0), are zero due to symmetric condition (i.e. $\hat{u}^*_{r,d}\big|_{r^*=0} = 0$ , and $\partial \hat{u}^*_{z,d} / \partial r^* = 0$ ). Therefore, modified Bessel functions of the second kind ($K_0$ ($k^* r^*$), $K_1$ ($k^* r^*$), and $K_3$ ($k^* r^*$)) in the stream-function of disperse liquid (equation (5.11a)) drop out. The third order, modified Bessel function of the first and second kind ($I_3$ ($k^* r^*$), and $K_3$ ($k^* r^*$)) for both liquids are negligible (Herrada, G.-Calvo, and Guillot, 2008), thus eliminated from equations (5.11a and 5.11b). The final simplified stream-function equations for the disperse and continuous liquids are expressed as:

(a) Disperse liquid:

$$\psi_d = \frac{1}{r^*} C_1 I_1(k^* r^*) + C_2 I_0(k^* r^*) \tag{5.12a}$$

(b) Continuous liquid:

$$\psi_c = \frac{1}{r^*} \{C_3 I_1(k^* r^*) + C_4 K_1(k^* r^*)\} + C_5 I_0(k^* r^*) + C_6 K_0(k^* r^*) \tag{5.12b}$$

In order to determine the six coefficients in equations (5.12a and 5.12b), six additional equations are needed. They are obtained from the applying the following three boundary conditions: (a) Non-slip condition at the wall, (b) continuity of the flow field at the interface, and (c) the momentum jump condition at the interface. The radial velocity of the continuous flow at the wall of the outer microtube is zero, $\hat{u}^*_{r,c}\big|_{r^*=R_c^*} = 0$ and there is non-slip at the wall, $\hat{u}^*_{z,c}\big|_{r^*=R_c^*} = 0$ . Applying these boundary conditions into equation (5.12b) gives the following two equations for the continuous liquid flow:

$$\begin{aligned} &C_3 k^* I_0\left(k^* R_c^*\right) + C_5\left(2I_0\left(k^* R_c^*\right) + k^* R_c^* I_1\left(k^* R_c^*\right)\right) \\ &\quad - C_4 k^* K_0\left(k^* R_c^*\right) + C_6\left(2K_0\left(k^* R_c^*\right) - k^* R_c^* K_1\left(k^* R_c^*\right)\right) = 0 \end{aligned} \tag{5.13a}$$

$$\begin{aligned} &- C_5 i k^* R_c^* I_0\left(k^* R_c^*\right) - C_3 i k^* I_1\left(k^* R_c^*\right) \\ &\quad - C_6 i k^* R_c^* K_0\left(k^* R_c^*\right) - C_4 k^* K_1\left(k^* R_c^*\right) = 0 \end{aligned} \tag{5.13b}$$

Additional two equations are obtained from the continuity of the flow field at the interface between the two co-flowing liquids ($r^* = 1$). At this interface, the perturbed velocities of disperse and continuous liquids are equal (i.e., $\hat{u}^*_{r,d} = \hat{u}^*_{r,c}$ and $\hat{u}^*_{z,d} = \hat{u}^*_{z,c}$). Substituting these conditions together with equations (5.12a) and (5.12b) into equations (5.10a) and (5.10b), gives:

$$\begin{aligned} &-C_1 ik^* I_1(k^*) + C_3 ik^* I_1(k^*) + C_4 ik^* K_1(k^*) \\ &\quad - C_2 ik^* I_0(k^*) + C_5 ik^* I_0(k^*) + C_6 ik^* K_0(k^*) = 0 \end{aligned} \tag{5.14a}$$

$$\begin{aligned} &C_1 k^* I_0(k^*) - C_3 k^* I_0(k^*) + C_4 k^* K_0(k^*) + C_2\left(2I_0(k^*) + k^* I_1(k^*)\right) \\ &\qquad + C_5\left(-2I_0(k^*) - k^* I_1(k^*)\right) + C_6\left(-2K_0(k^*) + k^* K_1(k^*)\right) = 0 \end{aligned} \tag{5.14b}$$

The final two equations are obtained based on satisfying the dynamic force balance (or momentum jump condition) at the interface (equation (3.3a)), with the introduced perturbation of the interface (equation (5.3)). In this case, the shear tensor ($\tau'_n$) for the disperse and continuous liquids can be expressed as:

$$\tau'_n = \begin{bmatrix} -P'_{r,n} + \tau'_{rr,n} & \tau'_{rz,n} \\ \tau'_{zr,n} & -P'_{z,n} + \tau'_{zz,n} \end{bmatrix} \tag{5.15}$$

Both the axial and radial components of the interfacial shear stress generally affect the movement of the interface. Assuming that the interface is a plane wave, only the radial components of interfacial shear forces need to be considered, thus equation (5.15) becomes:

$$\tau'_n = \begin{bmatrix} -P'_{r,n} + 2\mu_n \dfrac{\partial u'_{r,n}}{\partial r} & 0 \\ \mu_n\left(\dfrac{\partial u'_{r,n}}{\partial z} + \dfrac{\partial u'_{z,n}}{\partial r}\right) & 0 \end{bmatrix} \tag{5.16}$$

The force balance at the interface can be expressed as:

$$\left(-P_c' + 2\mu_c \frac{\partial u_{r,c}'}{\partial r}\right) - \left(-P_d' + 2\mu_d \frac{\partial u_{r,d}'}{\partial r}\right) = \sigma_{d,c}\left(\kappa' - \frac{1}{r_j^0}\right) \tag{5.17a}$$

The axial component of the interfacial shear stress is given as:

$$\mu_c\left(\frac{\partial u_{r,c}'}{\partial z} + \frac{\partial u_{z,c}'}{\partial r}\right) - \mu_d\left(\frac{\partial u_{r,d}'}{\partial z} + \frac{\partial u_{z,d}'}{\partial r}\right) = 0 \tag{5.17b}$$

Substituting equations (5.4) into equations (5.17a) and (5.17b) and rearranging the outcome, gives:

(a) Radial component of the interfacial shear stress

$$\left(-\hat{P}_c + 2\mu_c \frac{\partial \hat{u}_{r,c}}{\partial r}\right) - \left(-\hat{P}_d + 2\mu_d \frac{\partial \hat{u}_{r,d}}{\partial r}\right) = -\sigma_{d,c}\frac{\xi}{r_j^{0^2}}(1 - k^2 r_j^{0^2}) \tag{5.18a}$$

(b) Axial component of the interfacial shear stress

$$\mu_c\left(ik\hat{u}_{r,c} + \frac{\partial \hat{u}_{z,c}}{\partial r}\right) - \mu_d\left(ik\hat{u}_{r,d} + \frac{\partial \hat{u}_{z,d}}{\partial r}\right) = 0 \tag{5.18b}$$

These equations are rewritten in dimensionless forms as:

$$\left(-Re_{\text{int}}\hat{P}_c^* + 2\mu_r \frac{\partial \hat{u}_{r,c}^*}{\partial r^*}\right) - \left(-Re_{\text{int}}\hat{P}_d^* + 2\frac{\partial \hat{u}_{r,d}^*}{\partial r^*}\right) = -\frac{1}{Ka}\xi^*(1 - k^{*2}), \tag{5.19a}$$

and,

$$\mu_r\left(ik^*\hat{u}_{r,c}^* + \frac{\partial \hat{u}_{r,c}^*}{\partial r^*}\right) - \left(ik^*\hat{u}_{r,d}^* + \frac{\partial \hat{u}_{r,d}^*}{\partial r^*}\right) = 0 \tag{5.19b}$$

The kinematic boundary condition is used to find the dimensionless amplitude of the perturbed interface ($\xi^*$) in equation (5.19a). This condition states that the radial and axial velocity components of disperse and continuous liquids flows at the interface equal those of the interface itself. Thus, at any radial location, $r_j(z,t)$, the interface moves with

the same velocity as the disperse liquid. The radial location, and hence the amplitude "$\xi^*$" of the interface perturbations is obtained from the solution of following equation (Ashgriz, 2000; Jog, 2002):

$$\frac{\partial r_j}{\partial t} + u_d\Big|_{r=r_j^o} \cdot \nabla r_j = 0 \tag{6.20a}$$

This equation can also be written as:

$$\frac{\partial r_j}{\partial t} + u_{z,d}\Big|_{r=r_j^0} \frac{\partial r_j}{\partial z} - u_{r,d}\Big|_{r=r_j^0} = 0 \tag{6.20b}$$

Substituting for the total flow velocity in this equation from equation (5.4), neglecting the axial perturbed velocity, $u'_{z,d}$, and rearranging the result give the following equation:

$$-\xi i\omega + u^0_{z,d}\Big|_{r=r_j^0} \xi ik - \hat{u}_{r,d}\Big|_{r=r_j^0} = 0\,, \tag{5.21a}$$

This equation is expressed in a dimensionless form as:

$$-\xi^* i(\omega^* - k^*) + \hat{u}^*_{r,d}\Big|_{r=r_j^0} = 0\,. \tag{5.21b}$$

The amplitude ($\xi^*$) is eliminated by substituting equation (6.21b) into (6.19a), which gives:

$$\left(-Re_{\text{int}}\hat{P}^*_c + 2\mu_r \frac{\partial \hat{u}^*_{r,c}}{\partial r^*}\right) - \left(-Re_{\text{int}}\hat{P}^*_d + 2\frac{\partial \hat{u}^*_{r,d}}{\partial r^*}\right) = \frac{\hat{u}^*_{r,d}\Big|_{r^*=1}}{i(\omega^* - k^*)} \frac{1-k^{*2}}{Ka} \tag{5.22}$$

The dimensionless pressure terms ( $Re_{\text{int}}\hat{P}^*_c$ and $Re_{\text{int}}\hat{P}^*_d$ ) in this equation is obtained from the solution of equation (5.7b) together with equations (5.9a and 5.9b).

Equations (5.22) and (5.19b) are rewritten by expressing the velocities of the continuous and disperse liquids in terms of the stream function (equations (5.10a), (5.10b), (5.13a), and (5.13b)). The resulting two equations are given, respectively, as:

$$
\begin{aligned}
&C_1\left(2ik^{*2}I_0(k^*)-2ik^*I_1(k^*)+\frac{k^*\left(k^{*2}-1\right)I_1(k^*)}{Ka\left(k^*-\omega^*\right)}\right)-2iC_5k^{*2}\mu_rI_1(k^*)+\\
&C_3\left(2ik^*\mu_rI_1(k^*)-2ik^{*2}\mu_rI_0(k^*)\right)+2iC_6k^{*2}\mu_rK_1(k^*)+\\
&C_4\left(2ik^*\mu_rK_1(k^*)+2ik^{*2}\mu_rK_0(k^*)\right)+\\
&C_2\left(\frac{k^*\left(k^{*2}-1\right)I_0(k^*)}{Ka\left(k^*-\omega^*\right)}+2ik^{*2}I_1(k^*)\right)=0
\end{aligned}
\tag{5.23a}
$$

and,

$$
\begin{aligned}
&2iC_1k^*I_1(k^*)-2iC_3k^{*2}\mu_rI_1(k^*)+C_2\left(2k^{*2}I_0(k^*)+2k^*I_1(k^*)\right)\\
&+C_5\left(-2k^{*2}\mu_rI_0(k^*)+2k^*\mu_rI_1(k^*)\right)-2C_4k^{*2}\mu_rK_1(k^*)\\
&+C_6\left(-2k^{*2}\mu_rK_0(k^*)+2k^*\mu_rK_1(k^*)\right)=0
\end{aligned}
\tag{5.23b}
$$

In these equations, *Ka* is the capillary number of the disperse liquid at the interface of the basic flow. The six equations (5.13, 5.14, and 5.23) constitute a homogeneous linear system that involves six unknown constants (C1 to C6). The amplitude of the perturbations at the interface equals the eigenvalues in equation. To calculate the eigenvalues for equation (5.24), the determinant of the square matrix on the left-hand side of equation (5.24) should be zero.

$$
\begin{pmatrix}
2k^{*2}I_1(k^*) & A_2 & -2k^{*2}\mu_rI_1(k^*) & -2k^{*2}\mu_rK_1(k^*) & A_5 & A_6\\
B_1 & B_2 & B_3 & B_4 & -2ik^{*2}\mu_rI_1(k^*) & 2ik^{*2}\mu_rK_1(k^*)\\
-ik^*I_1(k^*) & -ik^*I_0(k^*) & ik^*I_1(k^*) & ik^*K_1(k^*) & ik^*I_0(k^*) & ik^*K_0(k^*)\\
k^*I_0(k^*) & D_2 & -k^*I_0(k^*) & k^*K_0(k^*) & D_5 & D_6\\
0 & 0 & k^*I_0(k^*R_c^*) & -k^*K_0(k^*R_c^*) & E_5 & E_6\\
0 & 0 & -ik^*I_1(k^*R_c^*) & -ik^*K_1(k^*R_c^*) & -ik^*R_c^*I_0(k^*R_c^*) & -ik^*R_c^*K_0(k^*R_c^*)
\end{pmatrix}
\begin{pmatrix}C_1\\C_2\\C_3\\C_4\\C_5\\C_6\end{pmatrix}=0
\tag{5.24}
$$

The constants $A_2$, $A_5$, $A_6$, $B_1$, $B_2$, $B_3$, $B_4$, $D_2$, $D_5$, $D_6$, $E_5$, and $E_6$ are expressed as:

$$
\begin{aligned}
A_2 &= 2k^{*2} I_0\left(k^*\right) + 2k^* I_1\left(k^*\right) \\
A_5 &= -2k^{*2} \mu_r I_0\left(k^*\right) - 2k^* \mu_r I_1\left(k^*\right) \\
A_6 &= -2k^{*2} \mu_r K_0\left(k^*\right) + 2k^* \mu_r K_1\left(k^*\right) \\
B_1 &= 2ik^{*2} I_0\left(k^*\right) - 2ik^* I_1\left(k^*\right) + \frac{k^*\left(k^{*2}-1\right) I_1\left(k^*\right)}{Ka\left(k^*-\omega^*\right)} \\
B_2 &= \frac{k^*\left(k^{*2}-1\right) I_0\left(k^*\right)}{Ka\left(k^*-\omega^*\right)} + 2ik^{*2} I_1\left(k^*\right) \\
B_3 &= -2ik^{*2} \mu_r I_0\left(k^*\right) + 2ik^* \mu_r I_1\left(k^*\right) \\
B_4 &= 2ik^{*2} \mu_r K_0\left(k^*\right) + 2ik^* \mu_r K_1\left(k^*\right) \\
D_2 &= 2I_0(k^*) + k^* I_1(k^*) \\
D_5 &= -2I_0(k^*) - k^* I_1(k^*) \\
D_6 &= -2K_0(k^*) + k^* K_1(k^*) \\
E_5 &= 2I_0\left(k^* R_c^*\right) + k^* R_c^* I_1\left(k^* R_c^*\right) \\
E_6 &= 2K_0\left(k^* R_c^*\right) - k^* R_c^* K_1\left(k^* R_c^*\right)
\end{aligned}
\tag{5.25}
$$

Equation (5.24) is a general form of an eigenvalue problem. The solution of the determinant for the square matrix is a very long equation in terms of $k^*$, $\omega^*$, $Ka$, $R_c^*$, and $\mu_r$. The rearranged equation gives the following expression for the dimensionless wave frequency as:

$$
\omega^* = k^* - i\frac{k^*(k^{*2}-1)\ NM}{2Ka\ DN}, \tag{5.26}
$$

In the equation, $NM$ and $DN$, functions of $k^*$, $R_c^*$ and $\mu_r$, are detailed in Appendix-A. Equation (5.26) is used to determine values for the absolute and convective instabilities corresponding to the transition and jetting regimes, respectively. In the present linear instability analysis, both the wave number and frequency are complex numbers, so that the perturbations' amplitude growth depend exponentially on ($\omega^*$ - $k^*$). Therefore, IM[$\omega^*$] and

**Table 5.1. Properties and parameters used in linear instability analysis.**

| Parameter | Value / Range | Units |
|---|---|---|
| Inner microtube radius, $R_d$ | 50 | μm |
| Outer microtube radius, $R_c$ | 160 – 600 | μm |
| Disperse liquid viscosity, $\mu_d$ | 0.06 | Pa·s |
| Continuous liquid viscosity, $\mu_c$ | 0.06 | Pa·s |
| Disperse/ continuous liquid density, $\rho_d / \rho_c$ | 1000 / 1000 | kg/m$^3$ |
| Interfacial tension, $\sigma_{d,c}$ | 0.02 | N/m |
| Outer microtube radius, $R_c / r_j^0$ | 1.75 - 553 | – |
| Microtube radius ratio, $R^*$ | 3.2 - 10.2 | – |

IM[$-k^*$] should be positive for the interface to be unstable due to the temporal and spatial growths of the amplitude of the interface perturbations. These perturbations travel at a velocity, IM[$\omega^*$]/IM[$-k^*$]. A breakup of a disperse droplet from the tip of the jet is affected by this traveling perturbation of the interface. When the velocity of the perturbation is positive, the growing perturbation of the interface propagate downstream (convective instability), and when the velocity is negative, the growing perturbation propagate upstream toward the exit of the disperse liquid microtube (absolute instability). The breakup of a disperse droplet in the jetting regime is considered the result of convective instability. Based on this criteria for the convective instability, the breakup of disperse droplet in the jetting regime occurs when the spatial growth rate of the wave, $-k^*i$, the moving velocity, IM[$\partial\omega^*/\partial k^*$] and the growth rate of the amplitude of the moving wave front, RE[$\partial\omega^*/\partial k^*$] are all positive.

### 5.2.2. Solution Methodology

Using the commercial algebra software, Mathematica 8.0 (www.wolfram.com), equation (5.25) is solved subject to the following conditions for marginal convective instability: IM[$\partial\omega^*/\partial k^*$] = 0, RE[$\partial\omega^*/\partial k^*$] = 0, and $-k^*i > 0$. The values of $R_c^*$ are varied from 1.7 to 553, the radius of the continuous liquid microtube is varied from 160 to 600 μm and the viscosity ratio, $\mu_r$, of the disperse and continuous liquids is unity (see Table 5.1). The solution determines the values of $k^*$, $\omega^*$, $Ka$ and $R_c^*$ corresponding to the boundary between the transition and jetting regimes for forming disperse droplets.

To express the instability results in terms of the dimensionless quantities, $Ca_d$ and $\mu_r\bar{u}_r$, the injection velocities of the disperse and continuous liquid had to be calculated. The obtained value of $Ka$ is used to calculate the interface velocity of the basic disperse

flow, $u^0_{z,\text{int}}$. This interface velocity and the calculated value of $R^*_c$ are used to calculate the injection flow rates of the co-flowing liquids ($Q^0_d$ and $Q^0_c$) using the following equations.

$$Q^0_c = u^0_{z,\text{int}} \pi \left( \frac{R_c}{R^*_c} \right)^2 \frac{R^{*2}_c - 1}{2} \tag{5.26a}$$

$$R^{*2}_c = 1 + \frac{Q^0_d}{Q^0_c} \left( 1 + \left( 1 + \frac{Q^0_d}{Q^0_c} \right)^{0.5} \right) \tag{5.26b}$$

## 5.3. Results and Discussion

The linear instability analysis is performed to predict the condition for the boundary between the transition and jetting regimes. This section presents and discusses the results. The performed analysis parametrically varied the injection rates of the liquids and the diameters of the coaxial microtubes (see Table 5.1). The analysis is validated by comparing the results with those of linear instability analysis reported by Herrada, Canan-Calvo and Guillot (2008) for aqueous solutions of glycerine and silicone oil flow in coaxial microtube with $R^*$ = 13.8. The present results are also compared to the experimental data for ionized water and PDMS (Polydimethylsiloxane) oil with $R^*$ = 10 (Utada et al., 2007). In addition, the results of the present linear instability analysis for the range of parameters in Table 5.1 are formulated into dimensionless quantities: $Ca_d$ and $\mu_r \bar{u}_r$. The values of these quantities are compared with the results of the present numerical simulations and the developed dimensionless correlation for the boundary between transition and jetting, discussed in Chapter 5.

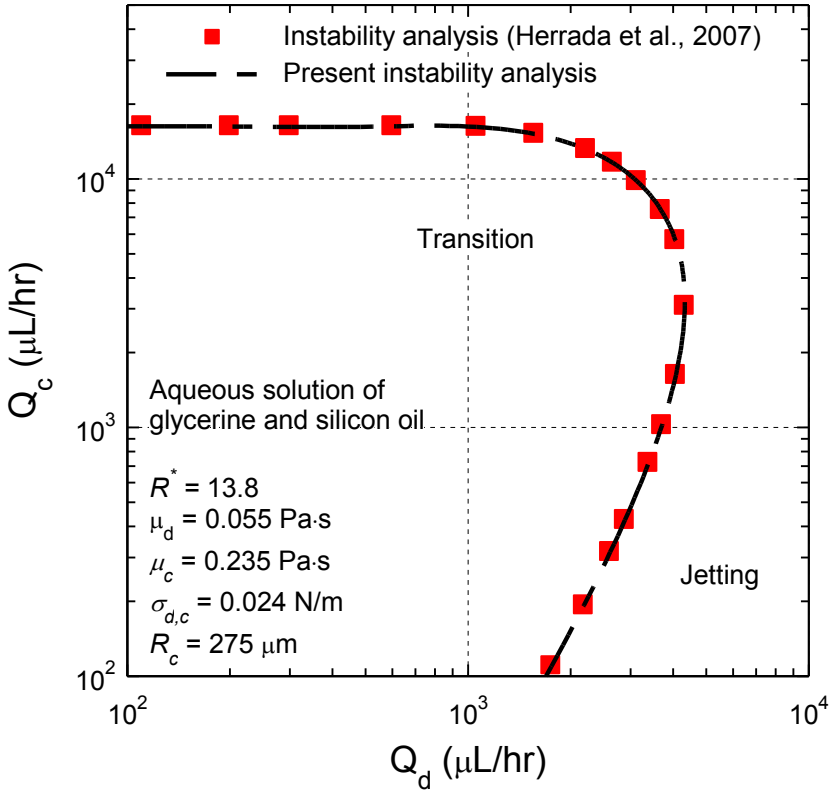


**Figure 5.3. Comparisons of the present instability analysis results with those of the instability analysis by Herrada et al. (2008).**

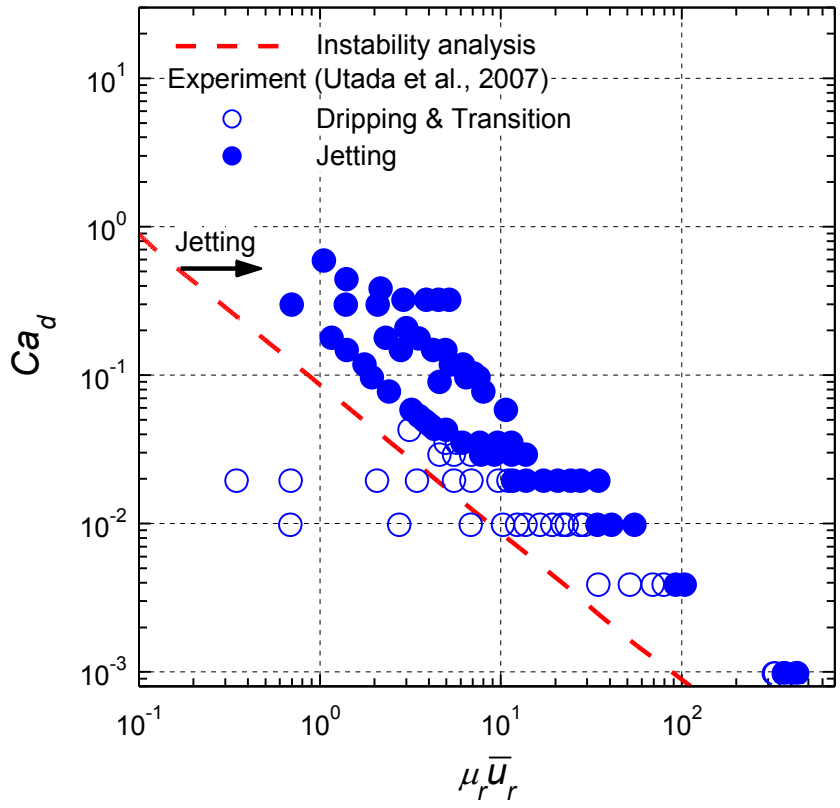


**Figure 5.4. Comparisions of the results of the instability analysis with the experimental data of Utada et al. (2007).**

### 5.3.1. Validation of Linear Instability Results

Figure 5.3 compares the present results for the boundary between transition and jetting with those reported by Herrada et al. (2008). It is no surprise that the present results are identical to those of Herrada et al. (2008), since the methodologies are identical. Nonetheless, such an agreement validates the absence of any error in implementing the methodology for performing parametric analysis. This analysis focuses on developing a data base for developing dimensionless regime map.

The results of the instability analysis, based on the parameters values in table 5.1, are formulated in terms of the dimensionless capillary number of disperse liquid, $Ca_d$, and the ratio of the dynamic forces of the continuous and disperse liquid, $\mu_r \bar{u}_r$. The results are then compared in the flow regimes map in Figure 5.4 with the experimental results of Utada et al. (2007). In Figure 5.4, the reported regimes experiment data by Utada et al. (2007) are for ionized water and PDMS (Polydimethylsiloxane) oil in coaxial microtubes with $R^* = 10$. Utada et al.'s (2007) have considered the transition regime to be a part of the dripping regime.

The comparison in Figure 5.4 confirms that the linear instability analysis, which uses the creeping flow approximation and considers linear perturbations, consistently underpredict the boundary between transition and jetting regimes. This could be attributed to the simplifying assumptions in the linear instability analysis. These include neglecting secondary perturbations, radial velocity of the interface, and higher order terms in the governing equations. In the next section, the comparison of the linear instability analysis results with the developed flow regimes maps, based on the numerical simulations in Chapter 4, are presented and discussed.

### 5.3.2. Comparison with Present Flow Regimes Map

Figures 5.5a – 5.5c compare the results of the linear instability analysis with the developed flow regimes maps in Chapter 4, based on the numerical results for the ranges of parameters listed in Table 3.1. The developed flow regimes map in Figure 5.5a, for $R_d$ = 50 and 100 μm and $R^*$ = 3.2, incorporates a total of 147 data points, including 51 data points in the dripping regime, 36 in the transition regime and 60 in the jetting regime. The flow regimes map in Figure 5.5b is for $R_d$ = 50 and 100 μm and $R^*$ = 6.4. It includes 166 data points of the flow regimes map, in the dripping regime, 242 in the transition regime and 188 in the jetting regime. Figure 5.5c for $R_d$ = 50 and 100 μm and $R^*$ = 10.2 includes of 69 data points in the dripping regime, 140 in the transition regime and 53 in the jetting regime. Figures 5.5a - 5.5c also compare the results of the instability analysis for $R^*$ = 3.2, 6.4, 10.2 with the developed dimensionless correlation in chapters for the boundary between transition and jetting (equation (4.1)).

The predictions of the instability analysis of the boundary between the transition and jetting regimes are consistently lower than equation (4.1) for low and intermediate $Ca_d$ values, but higher at higher $Ca_d$. Figure 5.5a shows that at low dynamic force ratios, $\mu_r \bar{u}_r <$ 0.85, the predictions of the instability analysis are higher than both the present correlations (equation (4.1)) and the numerical results, but increasingly lower as $\mu_r \bar{u}_r$ increase beyond 0.85. Increasing $R^*$ to 6.4 and 10.2 decreases the value of $\mu_r \bar{u}_r$ beyond which the linear instability analysis unpredicts the boundary between transition and jetting. This value is $\mu_r \bar{u}_r \approx$ 0.4 and 0.15 when $R^*$ = 6.4 and 10.4, respectively. Underestimating the boundary, between transition and jetting by linear instability analysis could be attributed to neglecting

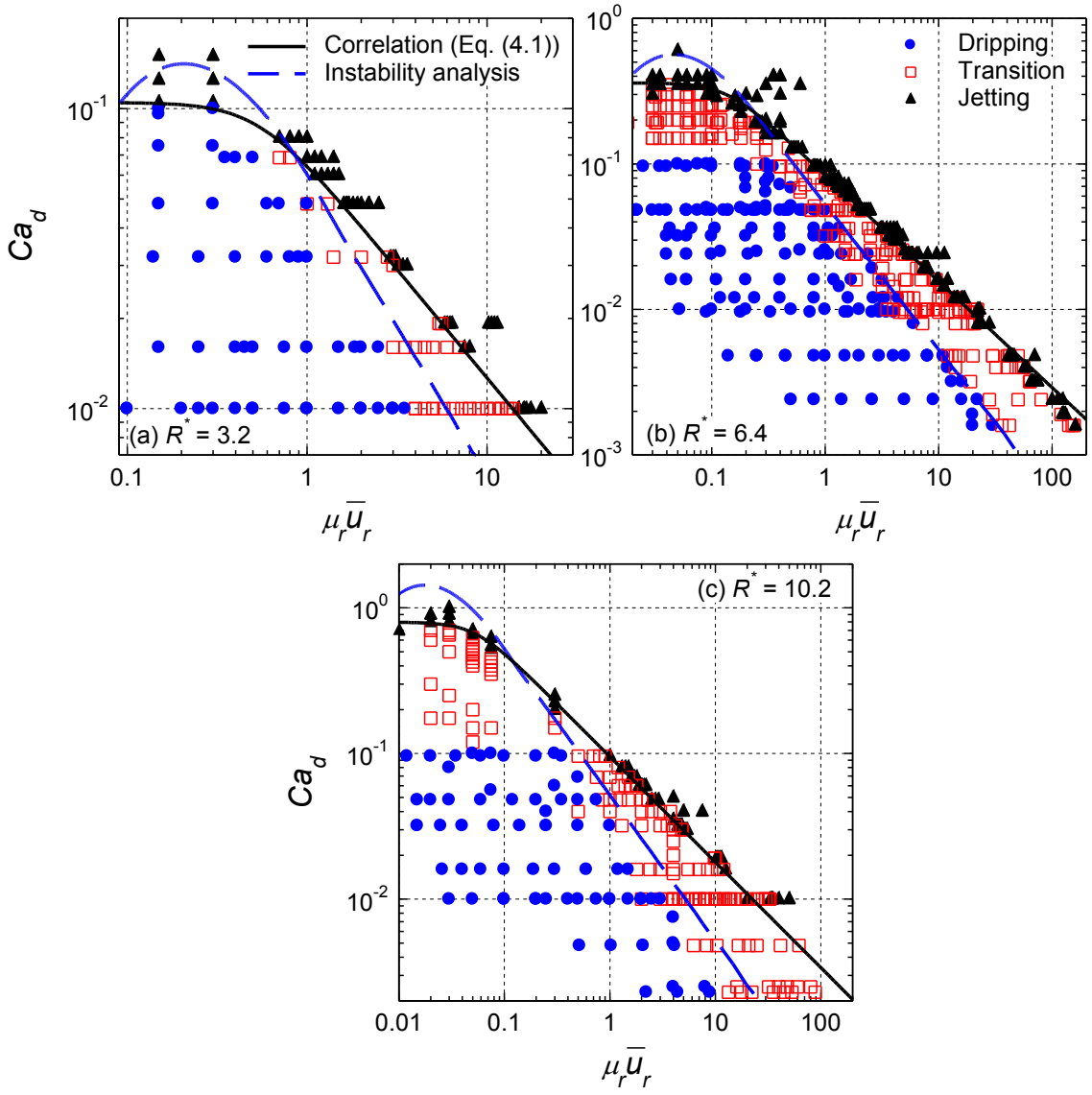


**Figure 5.5. Comparisons of instability analysis with the dimensionless correlation for the boundary between transition and jetting regimes. (a) $R^*$ = 3.2, (b) $R^*$ = 6.4 and (c) $R^*$ = 10.2.**

the inertia of disperse liquid, secondary perturbation and radial displacement and higher order terms in the linearized continuity and momentum balance equations. These assumptions, however, simplified the governing equation for obtaining a closed form analytical solution, requiring relatively much shorter time to perform the calculations than the numerical analysis, detailed in chapter 4. Note that for low values of $\mu_r \bar{u}_r$, the linear instability analysis missed the trend of the boundary between transition and jetting, indicating that the corresponding $Ca_d$ is almost independent of $\mu_r \bar{u}_r$ (Figures 5.5a – 5.5b)

Neglecting the secondary perturbations decreases the effective surface area of the disperse liquid jet, this overestimating the total hydrodynamic energy per the unit surface area corresponding to the boundary between transition and jetting regimes. This causes the linear instability analysis to predicts the boundary to occur at a lower value of the dynamic force ratios, $\mu_r \bar{u}_r$, compared to the present numerical results. The effect of neglecting the secondary perturbations by the linear instability analysis, decreases as the capillary number of the disperse liquid, $Ca_d$. It increases (Figures 5.5a – 5.5b). The difference in the values of the dynamic force ratios for the boundary between transition and jetting regimes by the linear instability analysis and the numerical results (chapter 4) decreases gradually, with increasing $Ca_d$, it diminishes when $Ca_d$ = 0.064, 0.25, and 0.0.5 in Figures 5.5a, 5.5b, and 5.5c, respectively.

## 5.4. Summary

This chapter presented and discussed the result of a linear instability analysis for predicting the boundary between transition and jetting regimes of forming disperse droplets. The results of the linear instability are compared with the reported flow regimes

map for ionized water and PDMS (Polydimethylsiloxane) oil (Utada et al., 2007), and the developed flow regimes maps in Chapter 5. The results of the linear instability based on disperse liquid creep flow approximation and neglecting secondary perturbations underestimate the boundary between the transition and jetting regimes.

# 6. RADIUS AND FORMATION FREQUENCY OF MONODISPERSE DROPLETS

This chapter presents and discusses the results of the numerical simulations investigating the effects of various liquids properties and operation parameters on the radius and formation frequency of disperse droplets in the dripping regime, and in the transition regime, but only when the volume of satellite droplet is < 1% of the primary droplet. The motivation of this investigation is to develop dimensionless correlations to predict the radius and the formation frequency of monodisperse droplets. In order to accomplish this objective, a parametric analysis is performed. The parameters considered in the present numerical simulations to develop a sufficient database are (Table 6.1): $\bar{u}_d$, $\bar{u}_c$, $\mu_d$, $\mu_c$ $R_d$, $R_c$, and $\sigma_{d,c}$. They are varied one at a time, while keeping others at their base values listed in Table 6.2. For the droplets in the transition regime, where the total volume of the satellite droplets is < 1% of the primary droplet, only the radius of the primary droplet is used in the comparisons presented and discussed in this chapter and for developing semi-empirical dimensionless correlations for the radius and formation frequency of the disperse droplets.

The next subsection presents the results of the parametric analysis investigating the effects of various properties of disperse and continuous liquids and the radii of co-axial microtubes on the radius and formation frequency of the disperse droplets. The obtained results, for wide ranges of liquids properties and operating parameters (Table 6.1), are used in the subsection 6.2 to develop the dimensionless semi-empirical correlations for the dimensionless radius and formation frequency of the disperse droplets.

**Table 6.1. Ranges of properties and parameters investigated in numerical simulations.**

| Parameter | Value / Range | Units |
|---|---|---|
| Inner microtube radius, $R_d$ | 50 - 100 | μm |
| Outer microtube radius, $R_c$ | 160 - 2020 | μm |
| Disperse liquid viscosity, $\mu_d$ | 0.0031 - 0.124 | Pa·s |
| Continuous liquid viscosity, $\mu_c$ | 0.0075 - 0.124 | Pa·s |
| Disperse/ continuous liquid density, $\rho_d / \rho_c$ | 1000 / 1000 | kg/m$^3$ |
| Interfacial tension, $\sigma_{d,c}$ | 0.01 - 0.0961 | N/m |
| Disperse liquid rate/ velocity, $Q_d / \overline{u}_d$` | 0.0487 - 2.4347 / 0.0062 - 0.31 | μl/s / m/s |
| Continuous liquid rate/ velocity, $Q_c / \overline{u}_c$ | 0.1924 - 9900 / 0.00037 - 2.48 | μl/s / m/s |
| Microtube radius ratio, $R^*$ | 3.2 - 20.2 | – |
| Disperse liquid Reynolds number, $Re_d$ | 0.02 - 1 | – |
| Disperse liquid Capillary number, $Ca_d$ | 0.0016 - 0.3844 | – |
| Continuous liquid Capillary number, $Ca_c$ | 0.0003 - 0.55 | – |
| Disperse liquid Weber number, $We_d$ | 0.0002 - 0.1602 | – |

**Table 6.2. Base values of properties and parameters in performed numerical simulations.**

| Parameter | Value | Units |
|---|---|---|
| Inner microtube radius, $R_d$ | 100 | μm |
| Outer microtube radius, $R_c$ | 1020 | μm |
| Disperse liquid rate/ injection velocity, $Q_d$ / $\overline{u}_d$ ` | 0.97 / 0.031 | μl/s / m/s |
| Continuous liquid rate/ injection velocity, $Q_c$ / $\overline{u}_c$ | 100 / 0.031 | μl/s / m/s |
| Disperse / Continuous liquid viscosity, $\mu_d$ / $\mu_c$ | 0.031 / 0.031 | Pa·s |
| Disperse/ Continuous liquid density, $\rho_d/\rho_c$ | 1000 / 1000 | kg/m$^3$ |
| Interfacial tension, $\sigma_{d,c}$ | 0.0961 | N/m |
| Disperse liquid Capillary number, $Ca_d$ | 0.01 | – |
| Continuous liquid Capillary number, $Ca_c$ | 0.01 | – |
| Disperse liquid Weber number, $We_d$ | 0.002 | – |
| Microtube radius ratio, $R^*$ | 10.2 | – |
| Disperse liquid Reynolds number, $Re_d$ | 0.2 | – |
| Continuous liquid Reynolds number, $Re_c$ | 1.8 | – |

## 6.1. Parametric Analysis Results

In the parametric analysis, the value of the capillary number of the continuous liquid, $Ca_c$, is varied by only varying the injection velocity of the continuous liquid. However, for the same value of $Ca_c$ by varying other properties (e.g., the interfacial tension, $\sigma_{d,c}$, or the continuous liquid viscosity, $\mu_c$) the diameter of the disperse droplet is different (see results in subsections 6.1.4 and 6.1.5). The next subsection presents and discusses the results of the performed parametric analysis.

### 6.1.1. Effects of Continuous Liquid Capillary Number and Microtube Radius

The results of the effects of the microtubes radii and of the capillary number of the continuous liquid (or injection velocity of the continuous liquid) on the dimensionless radius of the forming disperse droplets are presented in Figures 6.1a and 6.1b. These results are for $R_c$ = 320 μm, 520 μm and 1020 μm (or $R^*$ = 3.2 (solid circles), 5.2 (open triangles) and 10.2 (open squares)), respectively. Figure 6.1 shows that the dimensionless radius of the disperse droplet decreases slowly with increasing $Ca_c$ (or injection velocity of the continuous liquid) up to that corresponding to $r_d^*$ = 0.5 $R^*$ (or $r_d$ = 0.5 $R_c$). Below this value $Ca_c$, which depends on the radius of the continuous liquid microtube, the dimensionless radius of the forming disperse droplet, $r_d^*$, decreases inversely proportional to $\sqrt{Ca_c}$. Decreasing the radius of the continuous liquid microtube, $R_c$, decreases that of the forming disperse droplet. This is because, for the same injection velocity of the continuous liquid, decreasing its microtube radius increases the interfacial drag exerted onto the surface of the growing disperse droplet. Eventually, this effect causes the disperse

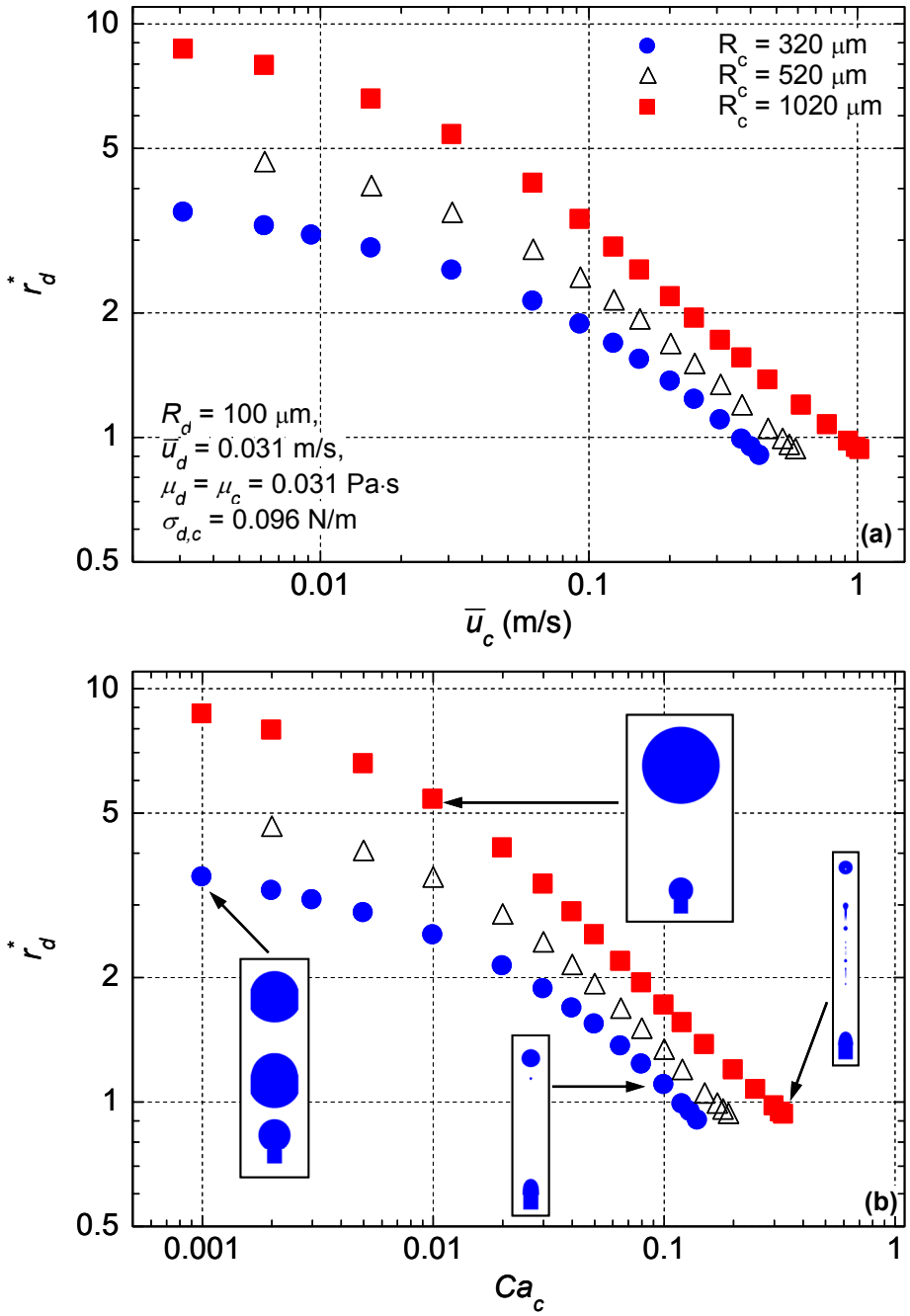


**Figure 6.1. Effects of microtube radius and inlet velocity of the continuous liquid (a) and Capillary number of the continuous liquid velocity (b) on the dimensionless radius of disperse droplet.**

droplet to pinch off at a smaller radius. The smaller droplet radius is typically associated with a higher frequency of formation.

The results delineated in Figure 6.1b also show that for $Ca_c \leq 0.01$, the monodisperse dripping regime prevails and relatively large droplets form one at time at a relatively low frequency. At higher values of $Ca_c$, the resulting emulsion becomes polydisperse. The pinch off of primary droplet is followed by the formation of one or several small satellite droplets. As shown in Figure 6.1b, at $Ca_c \approx 0.3$, the number and the collective size of the satellite droplets could affect the radius and the formation frequency of the significantly larger, primary droplet.

### 6.1.2. Formation Frequency

The calculated frequencies of forming disperse droplets in the dripping regime at different values of $Ca_c$ and radii of the continuous and disperse liquids microtubes, $R_c$ and $R_d$, are compared in Figure 6.2. These figures plot the formation frequency, determined from dividing the volumetric flow rate of the disperse liquid by the volume of the formed disperse droplet, $f_{mb}$, versus that determined from the transient progression in the numerical simulation, $f$. At low $Ca_c$, the two frequencies are identical. However, for the polydisperse droplets in the transition regime, occurring at high $Ca_c$, $f_{mb}$ of the primary droplet is progressively higher than $f$ with increased $Ca_c$. This is because only the volume of the primary droplet is considered, and the cumulative volume of the satellite droplets, which increase with $Ca_c$, is neglected in the determination of $f_{mb}$ (Figures 6.2a and 6.2b). The results in these figures show that the values of the formation frequencies and the difference between $f_{mb}$ and $f$, depends on the radii of the microtubes of the disperse and continuous coaxial flowing liquids.

The results in Figure 6.2a are for $R_d$ = 50 μm and $R^*$ = 3.2, 6.4 and 10.2, while those in Figures 6.2b are for $R_d$ = 100 μm and $R^*$ = 3.2, 5.2 and 10.2. For same $R_c$, decreasing $R_d$ (or increasing $R^*$) increases the formation frequency of the mono-disperse liquid droplets up to 200 and 100 Hz in Figures 6.2a and 6.2b, respectively. For polydisperse droplets in the transition regime, the formation frequency could be much higher; > 200 and 100 Hz, in Figures 6.2a and 6.2b, respectively.

The comparisons in Figures 6.2a and 6.2b confirm the accuracy of determining the formation frequency of the monodisperse droplet by dividing the flow rate of the disperse liquid by the volume of the forming droplet. This simple method is also accurate for determining the formation frequency of the primary droplets in the transition regime when the volume of the satellite droplets is negligibly small, < 1%. For this condition, which is satisfied in Figures 6.2a and 6.2b up to 350 and 160 Hz, respectively, the difference between $f_{mb}$ and $f$ for the primary droplets in the transition regime is negligibly small.

### 6.1.3. Effect of Disperse Liquid Microtube Radius

The results on the effects of the radius of disperse liquid microtube and the continuous liquid Capillary number, $Ca_c$, on the dimensionless radius of the disperse droplet are presented and compared in Figures 6.3a and 6.3b. The results are for two different radii of the disperse liquid microtube ($R_d$ = 50 μm and 100 μm), but same radius of the continuous liquid microtube, $R_c$ = 320 μm. The dimensionless radius of the disperse droplet in Figure 6.3a, $r_c^*$ , is based on that of the continuous liquid microtube, while that in Figure 6.3b, $r_d^*$, is based on the radius of the disperse liquid microtube. In Figure 6.3a, when $r_c^*$ < 0.5, it decreases inversely proportional to square root of the continuous liquid

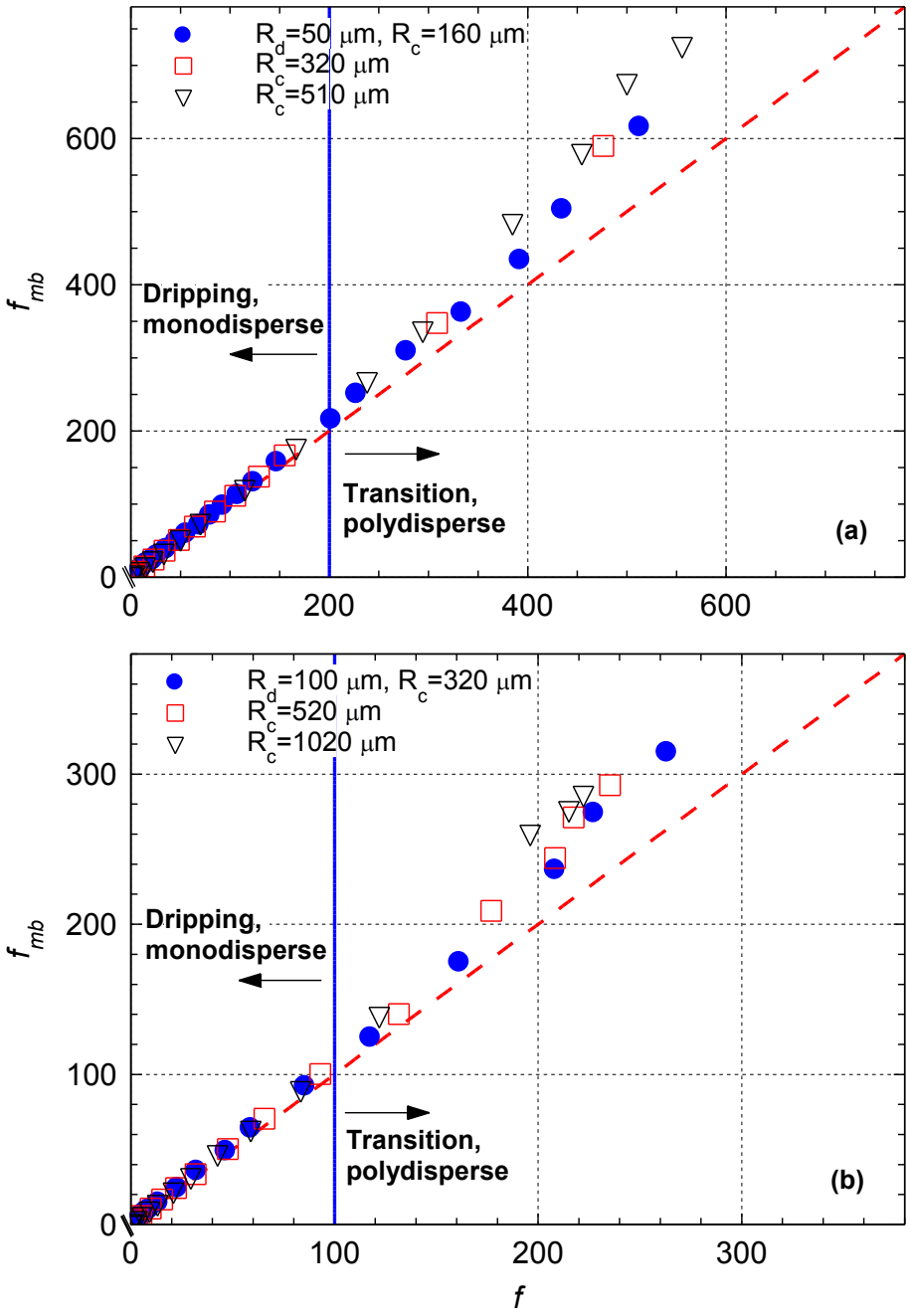


**Figure 6.2. Effects of radii of microtubes of disperse and continuous liquids on formation frequency of disperse droplets in dripping and transition regimes.**

Capillary number, $\sqrt{Ca_c}$ . The decrease in $r_c^*$ with increasing $Ca_c$, is more pronounced for the small disperse liquid microtube radius. At lower values of $Ca_c$, $r_c^*$ increases slower and the effect of $R_d$ on the radius of the forming disperse droplets gradually diminishes with decreasing $Ca_c$ (Figure 6.3a). Generally, for the same $Ca_c$, increasing the radius of disperse liquid microtube, $R_d$, increases that of the forming disperse droplet (Figure 6.3a).

For the same radii ratios of the disperse and continuous liquids microtubes, $R^*$, the dimensionless droplet radius, $r_d^*$, is independent of the radius of the disperse liquid microtube, $R_d$, but decreases with increasing $Ca_c$ (Figure 6.3b). The results in this figure also show that for the same $Ca_c$, increasing $R^*$ (or radius of continuous liquid microtube, $R_c$) increases the dimensionless radius of the forming disperse droplet, $r_d^*$. In addition to the geometrical effects shown in Figures 6.1 - 6.3, the physical properties of the coaxial flowing immiscible liquids, including the interfacial tension and the viscosities affect the frequency and the radius of the disperse droplets. The results demonstrating the effect of the interfacial tension, $\sigma_{d,c}$, are presented in Figures 6.4a – 6.4c and discussed next.

### 6.1.4. Effect of Interfacial Tension

The results presented in Figures 6.4a – 6.4c are for the same radius of disperse liquid microtube, $R_d$ = 50 μm, but three different values each of $R_c$ and $\sigma_{d,c}$. The interfacial surface tension is already included in the definition of $Ca_c$ ( $\mu_c \bar{u}_c / \sigma_{d,c}$ ), thus the results in these figures show how the interfacial surface tension, beyond that already included in $Ca_c$, affects the radius of the forming droplet, $r_d^*$. This additional effect is negligibly small. In general, at the same $Ca_c$, increasing the interfacial tension decreases the radius of the

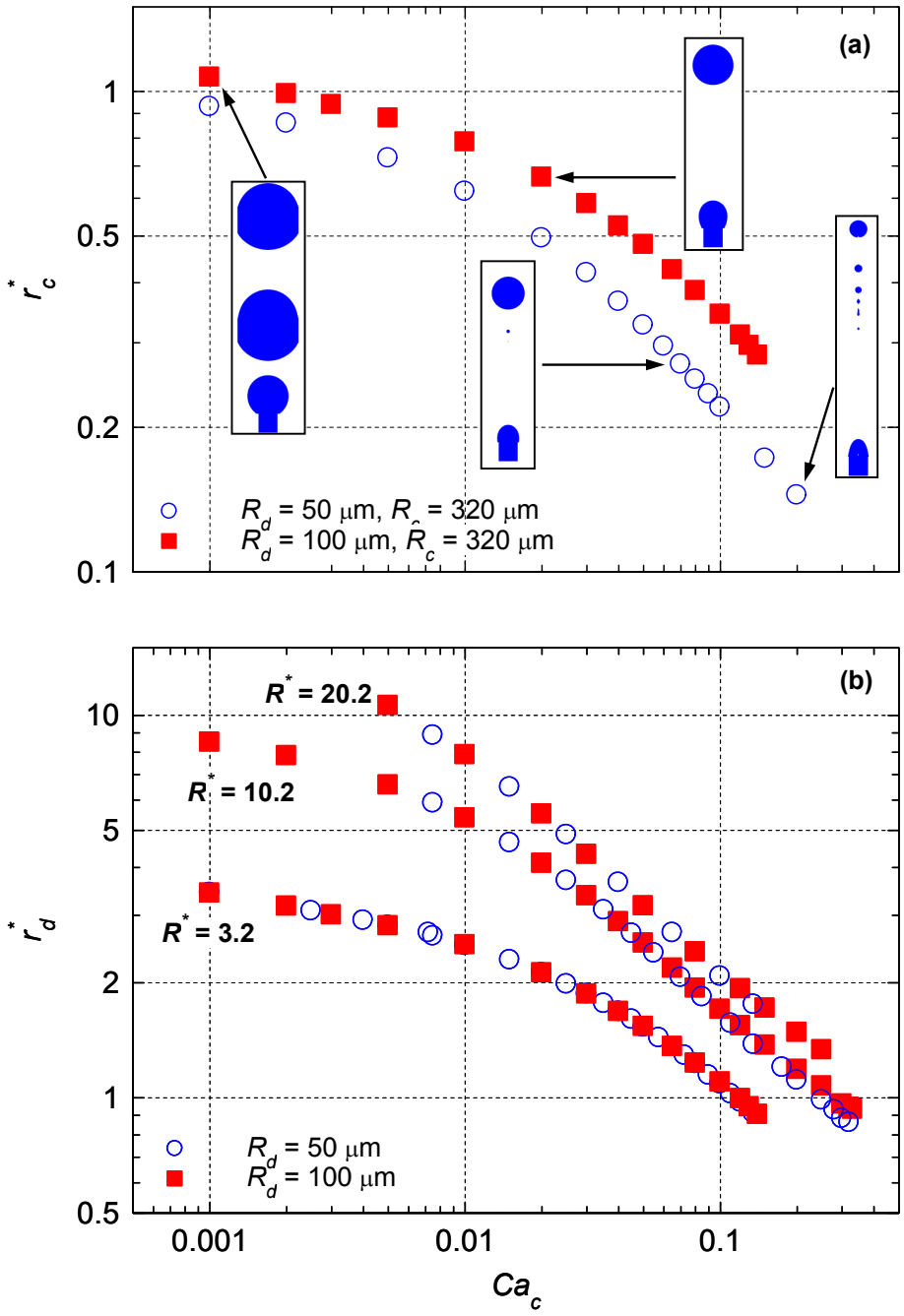


**Figure 6.3. Effects of disperse liquid microtube radius and continuous liquid Capillary number on the radius of disperse droplet.**

disperse droplet, depending on the value of $R_c$. When $R_c$ = 160 μm (or $R^*$ = 3.2), increasing the interfacial tension almost 5 times, from 20 to 96 mN/s, decreases the radius of the forming disperse droplet, $r_d^*$, by only ~20% (Figure 6.4a).

When increasing $R_c$ to 320 and 510 μm (or $R^*$ = 6.4 (Figure 6.4b) and 10.2 (Figure 6.4c)), respectively, the effect of interfacial tension on the droplet radius becomes progressive smaller. For example, the results in Figure 6.4c (for $R^*$ = 10.2 or $R_c$ = 510 μm) show that for the same $Ca_c$, increasing $\sigma_{d,c}$, from 20 to 96 mN/s decreases the radius of the forming disperse droplet by only 5%. Figures 6.4a – 6.4c also show that for the same $Ca_c$, the additional effect of increasing interfacial tensions diminishes at $Ca_c \geq 0.1$. To present the total effect of the interfacial tension on the radius of the forming disperse droplet, $r_d^*$, the results in Figures 6.4a - 6.4c are shown in Figures 6.4d – 6.4f, respectively, by plotting $r_d^*$ versus the ratio of the average injection velocities of the continuous and disperse liquids, $\overline{u}_c / \overline{u}_d$. The results in Figures 6.4d – 6.4f clearly show that decreasing the interfacial tension, $\sigma_{d,c}$, or increasing the average injection velocity of the continuous liquid, $\overline{u}_c$, decreases the dimensionless radius of the disperse droplet, $r_d^*$. The next subsection presents the results on the effects of the dynamic viscosities of the disperse and continuous liquids on the radius of forming disperse droplets in the dripping regime.

### 6.1.5. Effect of Dynamic Viscosities of Liquids

The results in Figures 6.5 and 6.6 show the effects of changing the dynamic viscosities of the disperse and continuous liquids, $\mu_d$ and $\mu_c$, on the radius of the disperse droplets in the dripping and transition regimes. Figure 6.5 shows that increasing the

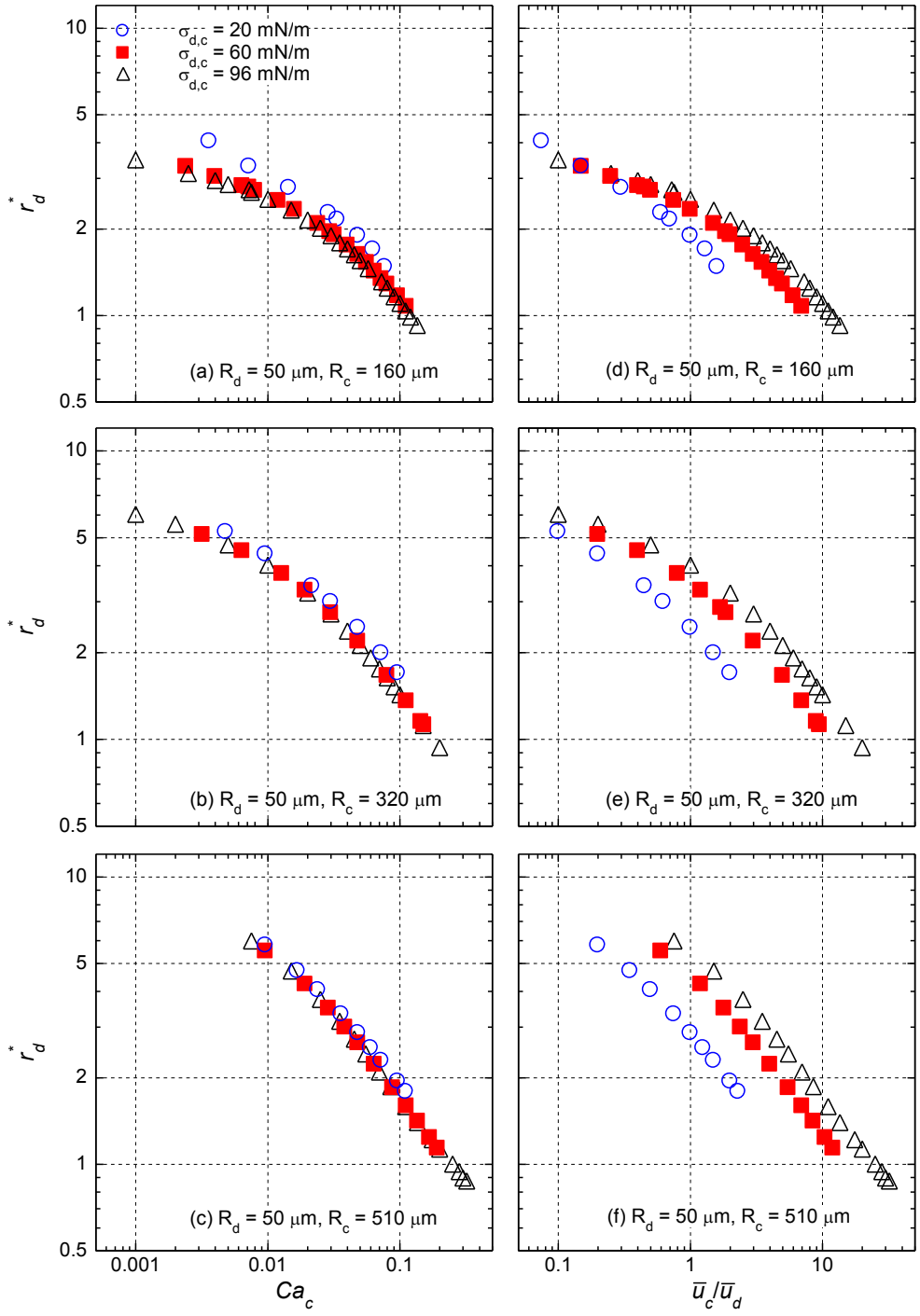


**Figure 6.4. Effects of continuous liquid microtube radius and interfacial tension on the radius of disperse droplet.**

viscosity of the disperse liquid only slightly decreases the radius of the forming droplets. Such an increase in disperse liquid viscosity slows down the growth rate of the droplet, but increases the rate of momentum transfer to the interface. The combined effect initiates earlier necking and smaller droplets pinch off (Figure 6.5). Conversely, increasing the dynamic viscosity of the continuous liquid, $\mu_c$, (or $Ca_c$) increases the drag exerted onto the surface of the growing disperse droplet, delaying its necking and pinch-off. Thus, the radius of the disperse droplet increases with increased viscosity of the continuous liquid (Figures 6.6a and 6.6b). In general, the dynamic viscosity of the continuous liquid has a larger effect than that of the disperse liquid on the radius of disperse droplet, at same $Ca_c$.

The effect of changing the viscosity of either the continuous or disperse liquid on the radius of the forming disperse droplet decreases with increasing $Ca_c$. Increasing the viscosity of the disperse liquid (Figure 6.5) or decreasing that of the continuous liquid (Figures 6.6a and 6.6b) decreases the radius of the disperse droplet, however, the decrease is relatively small. For example, in Figure 6.5 for the same $Ca_c$ increasing the disperse liquid viscosity ~16 times, from 0.0078 to 0.124 Pa.s, decreases the radius of the forming disperse droplet by less than 25%.

Conversely, the results in Figure 6.6a show that for the same $Ca_c$, increasing the viscosity of the continuous liquid ~16 times, from 0.0078 to 0.124 Pa.s, increases the size of the forming disperse droplet by about 44%, at $Ca_c < 0.08$ and slightly less at higher values of $Ca_c$. To show the total effect of the continuous liquid viscosity, the results in Figure 6.6a are plotted in Figure 6.6b in terms of the ratio of the average injection velocities of the continuous and disperse liquids. Figure 6.6b shows that the continuous

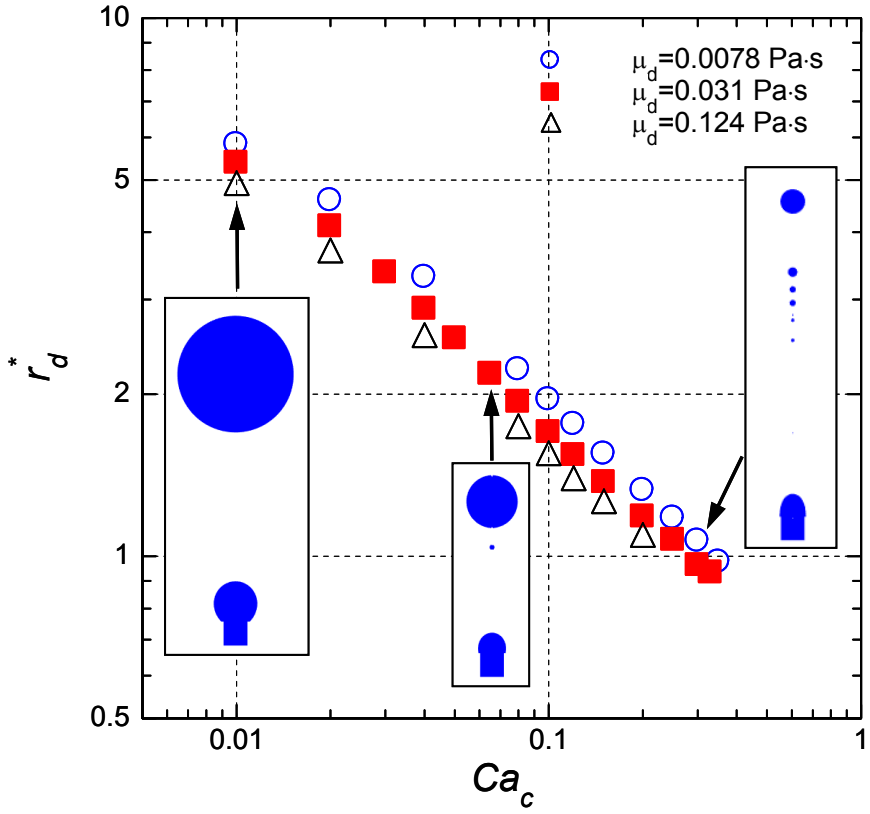


**Figure 6.5. Effects of disperse liquid viscosity and continuous liquid Capillary number on the radius of disperse droplet.**

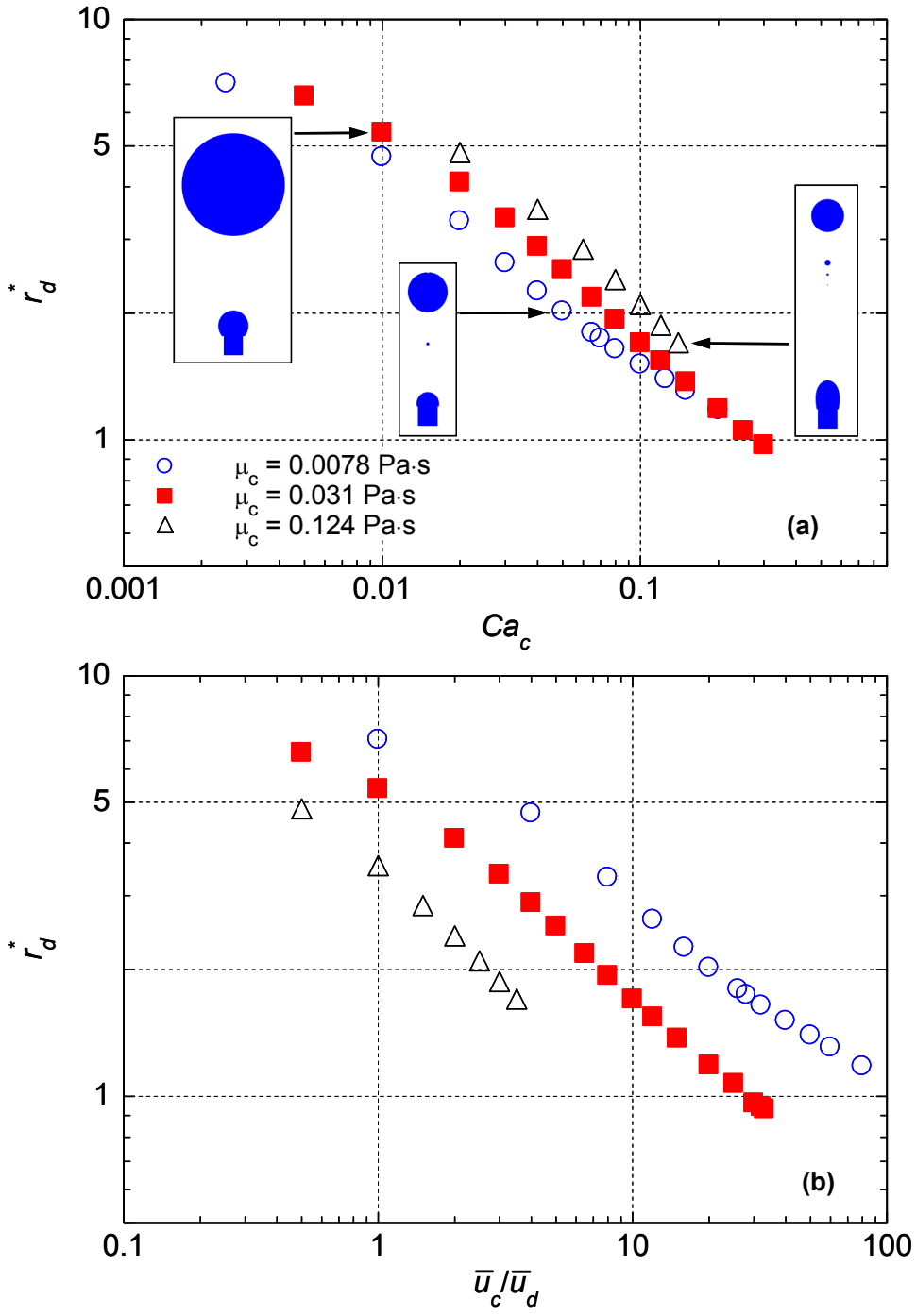


**Figure 6.6. Effects of continuous liquid viscosity and Capillary number on radius of the disperse droplets.**

liquid viscosity strongly affects the radius of the forming disperse droplets. Increasing the continuous liquid viscosity significantly increases the radius of these droplets in the dripping regime. The results presented in Figures 6.1 – 6.6 show a strong dependence of the radius of the disperse droplet on the injection rate or the capillary number of the continuous liquid, $Ca_c$. In the present analysis, the injection rate of the disperse liquid are relatively very low ($We_d$ is << 1.0). The obtained results of the effect of the injection rate of the disperse liquid (Table 6.1) on both the radius and frequency of the forming droplets are presented and discussed next (Figures 6.7a and 6.7b).

### 6.1.6. Effect of Disperse Liquid Injection Rate

Unlike the injection rate of the continuous liquid, that of the disperse liquid insignificantly affects the size of the forming disperse droplets in the dripping regime (Figure 6.7a). This is because disperse liquid injection rates used in the present analysis (Table 6.1) are low ($We_d$ << 1). The results in Figure 6.7a show that increasing the injection rate of the disperse liquid by 4.4 times, from 0.22 to 0.97 μl/s, increases the radius of the disperse droplet by less than 10%. Results also show that increasing $Ca_c$ markedly decreases the radius of the forming disperse droplet. For example, when $Ca_c$ = 0.001 the radius of the disperse droplet is as much as 8.5 times that of the inner microtube ($r_d^*$ = 8.5), but almost the same as that of the inner micro-tube ($r_d^*$ = 1.0) when $Ca_c$ ~ 0.3 (Figure 6.7a). The radius of the disperse droplet is inversely proportional to its formation frequency (Figure 6.7b). Although increasing the injection rate of the disperse liquid has little effect on the radius of the forming disperse droplets (Figure 6.7a), it generally increases their formation frequency. For example, the results in Figure 6.7b show that for a disperse

droplet radius that is twice that of the inner microtube ( $r_d^* = 2.0$), increasing the injection rate of the disperse liquid from 0.22 to 0.97 μl/s increases the frequency of forming this droplet from ~6 to 30 Hz. When halving the droplet size ( $r_d^* = 1.0$) the formation frequency increases from ~40 to as much as 200 Hz. The results of the parametric analysis presented and discussed in subsections 6.1.1 to 7.1.6, are used for developing dimensionless correlations for the radius and formation frequency of disperse droplets. These correlations are valid in the dripping regime. They also apply in the transition regime, only when the total volume of the satellite droplets is much smaller than that of the primary disperse droplet, or < 1%. The developed correlations are presented next.

## 6.2. Dimensionless Correlations for Disperse Droplets

The results of the present parametric analysis quantified the separate effects of the various parameters on both the radius and formation frequency of disperse droplets. The compiled analysis results are used to develop semi-empirical correlations of the dimensionless radius and formation frequency of disperse droplets in the dripping regime and in the transition regime, when the volume of satellite droplets < 1% of that of the primary droplet. These correlations, presented and discussed next, are valid for the ranges of liquids properties and parameters listed in Table 6.1 and the dimensionless quantities in Figure 6.8.

### 6.2.1. Disperse Droplet Radius Correlation

The values of the dimensionless radius of the disperse droplet, over wide ranges of liquid properties and parameters (Table 6.1 and Figure 6.8), are correlated as:

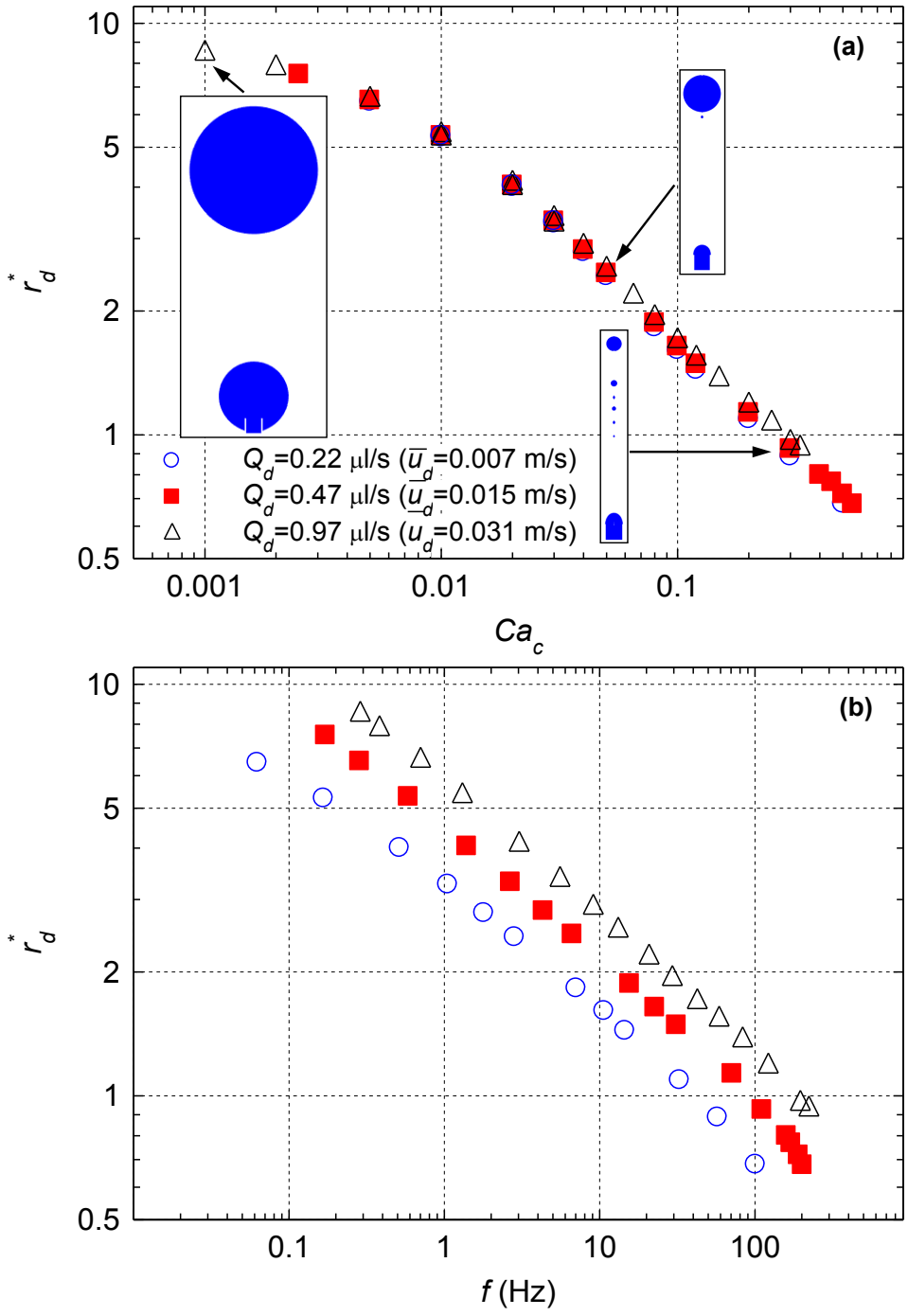


**Figure 6.7. Effects of disperse liquid injetction rate on disperse droplet radius and formation frequency.**

$$r_d^* = \frac{r_d}{R_d} = 0.228 R^{*0.466} \left( \frac{\mathrm{Re}_d}{\mathrm{Re}_d} \right)^{0.05} \left( \frac{1}{Ca_c} \right)^{0.5} \tag{6.1}$$

This correlation, for $r_d^* \leq 0.5\ R^*$, agrees with the numerical results to within +20% to - 6% (Figure 6.8). The dimensionless radius of the disperse droplet strongly depends on the ratio of the radii of the coaxial microtubes (Figure 3.1) and the Capillary number of continuous liquid, $Ca_c$. It weakly depends on the ratio of the Reynolds numbers of the disperse and continuous liquids.

The exponents of the different dimensionless quantities on the right hand side of equation (6.1), reflect their weighting on the radius of the forming disperse droplet. The exponent of the Capillary number of the continuous liquid, $Ca_c$, is the largest, but negative (− 0.5), followed close second by that of the radii ratio of the continuous and disperse liquid microtubes (0.466), and a distance third by the exponent of the Reynolds numbers ratio of these liquids (0.05).

The developed semi-empirical correlation for the dimensionless radius of the disperse droplets in the dripping regime (equation. (6.1)) is compared in Figure 6.9 with the reported experimental measurements for co-flowing water (disperse liquid) and salad oil (continuous liquid) in coaxial microtubes by Gu, Kojima and Miki (2011). This comparison is for disperse droplet radius (water), $r_d^* \leq 0.5\ R_c$. Table 6.1 lists the parameters and liquids properties in the experiments of Gu, Kojima and Miki (2011). Equation (6.1) is within +10% to −14% of the experimental measurements of the radius of the disperse water droplets in a continuous co-flowing salad oil in the dripping regime (Figure 6.9). The good agreement between the developed correlation (equation (6.1)) and

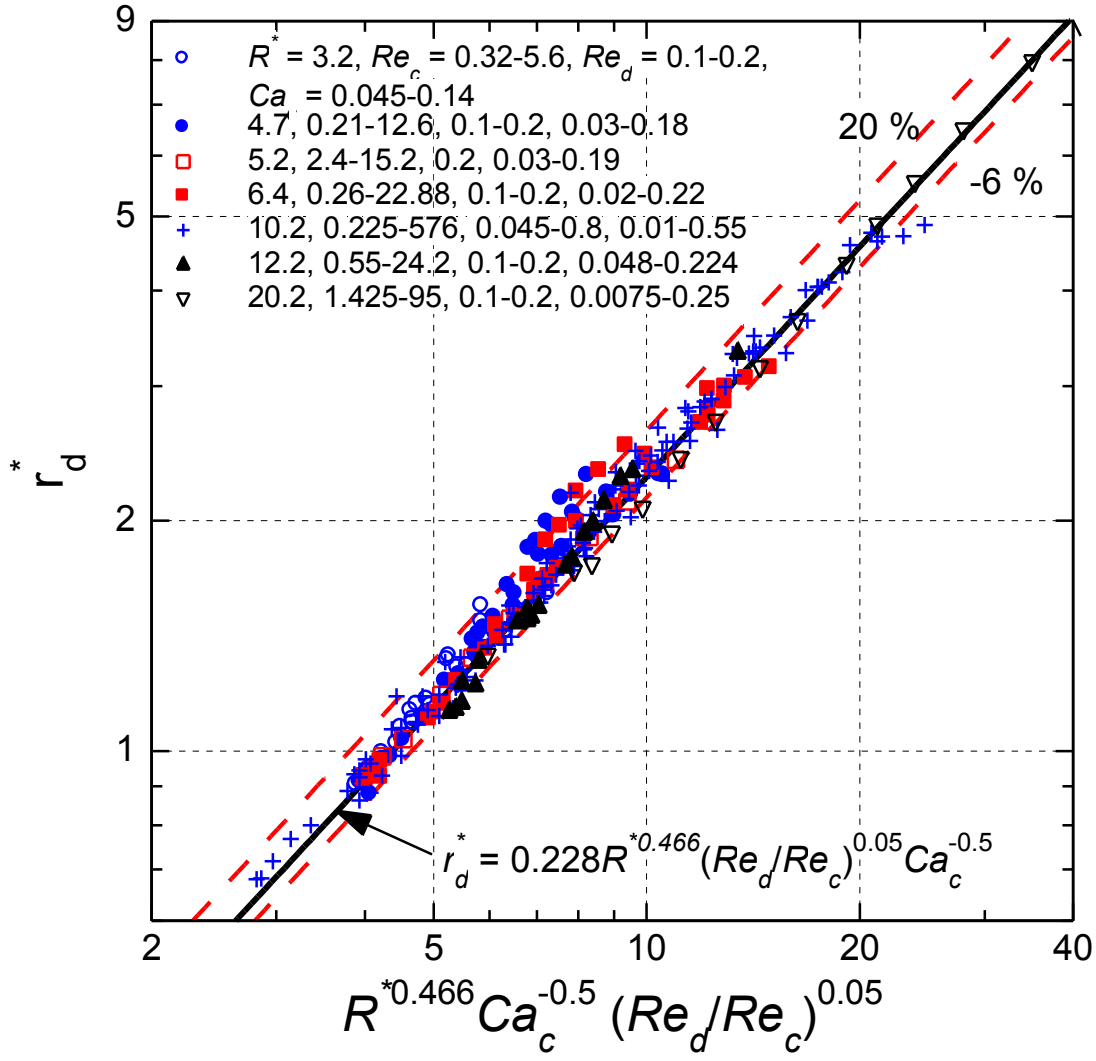


**Figure 6.8. Comparison of semi-empirical correlation (equation (6.1)) with numerical results of the dimensionless radius of disperse droplet.**

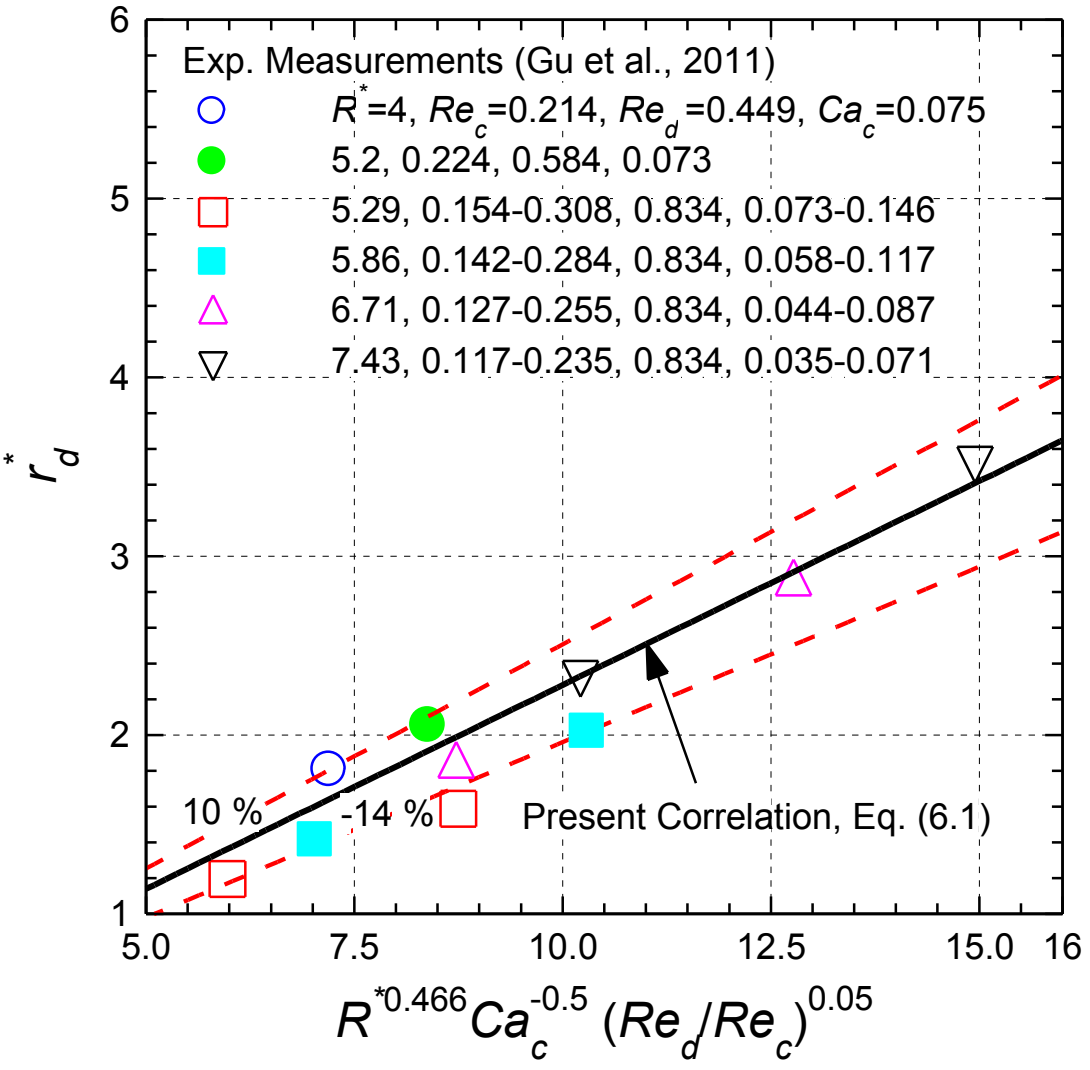


**Figure 6.9. Comparison of semi-empirical correlation (equation (6.1)) with experimental measurements of dimensionless radius of Gu Kojima and Miki (2011).**

the experimental measurements of Gu, Kojima and Miki (2011) further validates the methodology used in the present analysis and the fidelity of the numerical simulations. Based on the validation of the present numerical calculations of the dimensionless radius of the disperse droplets, the corresponding values of the dimensionless formation frequency are compiled to develop a semi-empirical correlation (equation (6.2)), presented and discussed next. This correlation is compared in Figure 6.10 with the present numerical simulation results.

### 6.2.2. Correlation of Formation Frequency of Disperse Droplets

The calculated values of the dimensionless frequency of forming disperse droplets in the dripping regime are correlated, using the same dimensionless quantities on the right hand side of equation (6.2), but in opposite proportionality and with higher exponents (Figure 6.10), as:

$$f^* = 53.26\, Ca_c^{1.47} \frac{1}{R^{*1.369}\left(\mathrm{Re}_d / \mathrm{Re}_c\right)^{0.147}} \tag{6.2}$$

While the dimensionless disperse droplet radius, $r_d^*$, increases proportional to the grouping of the dimensionless quantities on the right hand side in equation (6.2), the dimensionless frequency of forming droplets, $f^*$, decreases as the total value of the dimensionless quantities on the right hand side of equation (6.2) increases. The respective exponents indicate the weighting of the dimensionless quantities on the right hand side of equation (6.2).

Figure 6.10 compares the developed correlation for the dimensionless frequency of forming the disperse droplets in the dripping regime (equation (6.2)), subject to the ranges

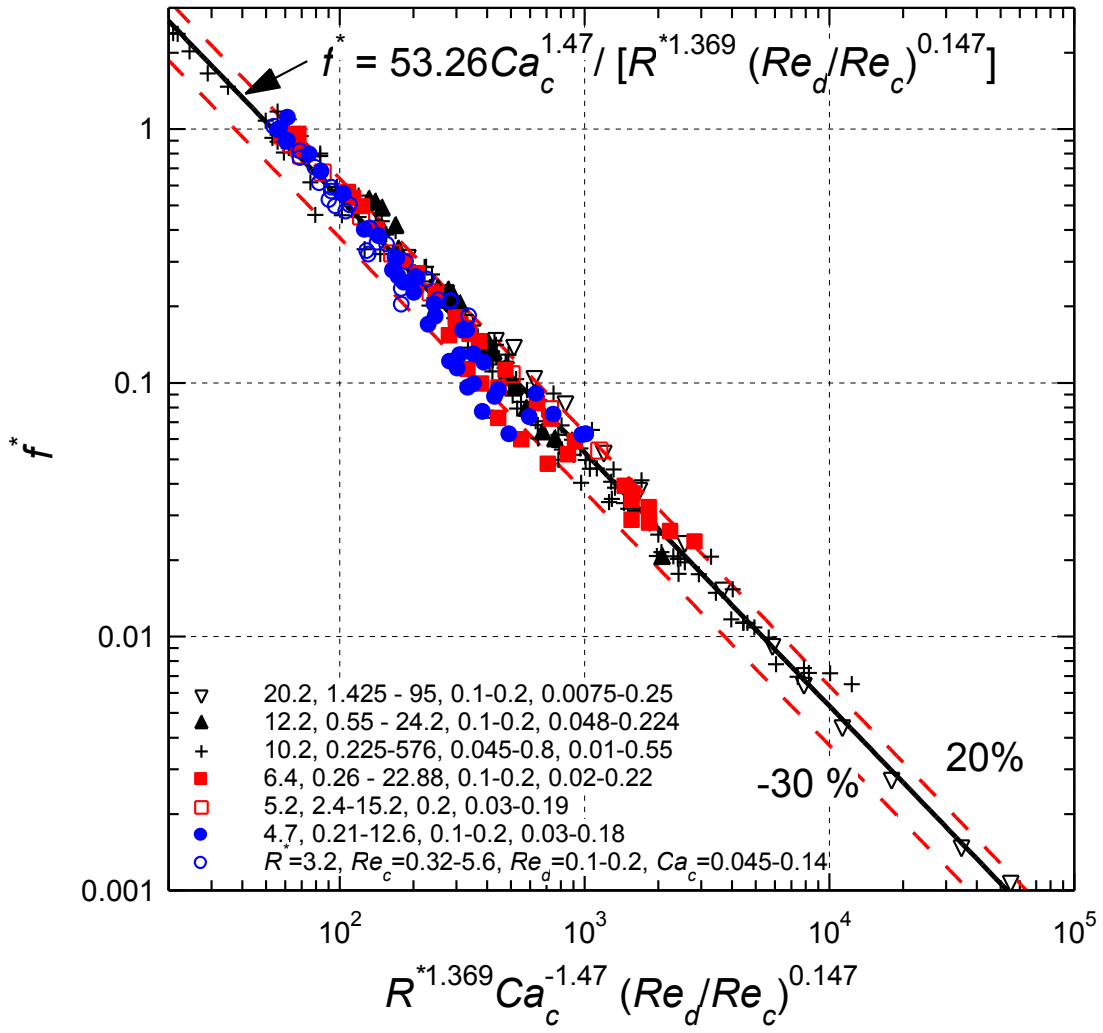


**Figure 6.10. Comparison of semi-empirical correlation (equation (6.2)) with calculated values for dimensionless frequency of disperse droplets.**

of parameters listed in Table 6.1 and shown in Figures 6.8 and 6.10. This correlation is within +20% to −30% of the numerical values of the dimensionless frequency of the disperse droplets.

## 6.3. Summary

This chapter presented the results of numerical simulations investigating the effects of different operation parameters and physical properties of the disperse and continuous co-flowing liquids on the radius and formation frequency of disperse droplets. The obtained numerical results are used to develop semi-empirical correlations of the dimensionless radius ($r_d^*$) and corresponding formation frequency ($f$*) of the disperse droplets for $r_d^* < 0.5\ R^*$. The correlation for $r_d^*$ is within + 20% to – 6%, while that for $f$* is within + 20% to -30% of the numerical predictions in the dripping regime.

The developed correlation for the dimensionless radius of disperse droplets in the dripping regime is within +10% to -14% of recently reported experimental measurements for the formation of disperse water droplets in a co-axial continuous flow of salad oil in the dripping regime (Gu, Kojima, and Miki, 2011). Such good agreement further confirms the soundness of the numerical method used and validates it accurately for calculating the size and determining the frequency of forming monodisperse droplets in the dripping and transition regimes.

# 7. SUMMARY AND CONCLUSIONS

This present work numerically simulated co-flowing immiscible liquids in coaxial microtubes for forming disperse droplets and investigated the effects of the injection velocities, diameters of microtubes and physical properties of the liquids and the interfacial tension on the characteristics and the boundaries of the regimes of forming the droplets. Also investigated are the effects of these parameters on the monodisperse droplet' radius and formation frequency. Dimensionless correlations are developed for predicting the disperse droplet radius and formation frequency, as well as the boundaries between the dripping, transition and jetting regimes of forming disperse droplets.

The numerical approach simultaneously solves the transient Navier-Stockes equations of the co-flowing liquids and the advection equation for the evolving interface, in conjunction with the momentum jump condition at the interface. The location and shape of the evolving disperse droplet are determined using the Level Set method. The present numerical simulations employed the commercial multi-physics software package of COMSOL 4.0a. The solver of COMOL 4.0a based on the finite element method implemented the Level Set method to track the evolving interface between the two immiscible, co-flowing liquids.

The numerical mesh grid in the computation domain for the present simulations comprises quadrilateral mesh elements of a uniform size (5 x 5 μm). The total number of mesh elements in the domain, which varied from 30 to 60 times the radius of the disperse liquid microtube, increases from 9,560 to 60,650, commensurate with radius of the continuous liquid microtube. Using a finer numerical grid, insignificantly changes the results, but increases computation time, which typically varies from 28 to 168 hours per

run. The length of the computation domain provided enough distance, from the tip of disperse liquid capillary, to obverse at least 3-5 and as much as 18 formation cycles of the primary disperse droplets, including the first one.

Numerical results are validated by comparing them with those reported by Hua, Zhang, and Lou (2007), and the experimental measurements reported by Gu, Kojima, and Miki (2011). The numerical results of Hua, Zhang, and Lou (2007) spans the dripping and jetting regimes, by increasing the flow rate of the disperse liquid (15 – 118 μl/s) with microtubes radii ratio, $R^* = 3.75$. Gu, Kojima, and Miki (2011) experimentally measured the disperse droplet radius in the dripping regime using aqueous solution of sodium alginate and salad oil in coaxial microtubes with $R^* = 2.5 - 6.7$. The calculated radii of the disperse droplets are within ± 10 % of the reported values by Hua, Zhang, and Lou (2007), and Gu, Kojima, and Miki (2011).

The results of as much as 1500 separate cases, are used to produce motion picture movies for characterizing the growth dynamics and the break off mechanisms of the disperse droplets and characterize the three distinct regimes of the droplet formation: *Dripping* (or monodisperse dripping), *Transition* (or polydisperse dripping), and *Jetting*. Monodisperse droplets are typically produced in the dripping regime, at low injection velocities of disperse and continuous liquids and high interfacial tension. In this regime, the pinch-off of the droplets occurs at the exit of disperse liquid capillary nozzle. Increasing the injection velocity of either liquids, produced a very thin and short thread of the disperse liquid between the exit of disperse liquid microtube and the growing droplet. Following the pinch off of the primary droplets, the disperse liquid thread breaks up by the interfacial tension and hydrodynamic instability into a few satellite droplets of miniature

sizes. These developments characterize the transition regime. Further increase of the injection velocities of the disperse and continuous liquids increases the length of the disperse-liquid thread, which eventually evolves into a stable jet. The formation of a stable liquid jet and the break off of disperse droplets by growing instability at the tip of the jet, characterize the jetting regime. In this regime, the sizes of the disperse droplets are comparable, but not identical and depend on the type of the stable jets: narrowing or widening. The former produces small primary disperse droplets (<100 μm in diameter) and highly polydisperse emulsion, while the latter produces relatively very large droplets (~400 - 500 μm in diameter) and very few satellite droplets.

The compiled numerical results database is used to develop a flow regimes map and dimensionless correlations for the boundaries between dripping, transition and jetting. These correlations for predicting the boundaries between dripping, transition and jetting are expressed in terms of dimensionless quantities: $Ca_{d,DT}$, $Ca_{d,TJ}$, $\mu_r \bar{u}_r$, $R^* \mu_r \bar{u}_r$ and $R^*$. The correlation for determining the boundary between the transition and jetting regimes is within ± 10% of the numerical calculations. The dimensionless correlation for the boundary between dripping and transition also agrees, to within $\pm$20%, with the numerical calculations. These correlations are validated by comparing to the reported experimental measurements by different investigators. These measurements are for different immiscible liquids, including aqueous solution of κ-Carrageeenan and sunflower oil with $R^* = 44.44$ (Cramer et al., 2004), aqueous solution of sodium alginate and salad oil in co-axial microtubes with $R^* = 2.5 - 6.7$ (Gu et al., 2011) ionized water and PDMS (Polydimethylsiloxane) oil with $R^* = 10$ (Utada et al., 2007), and aqueous solutions of glycerine into silicone oil flow with (Guillot et al., 2007) and without surfactant (Sodium

Dodecyl Sulfate) with $R^*$ = 13.8 (Herrada et al, 2008). The results of characterizing the flow regimes of disperse droplets shows that the monodisperse micro-emulsion is achievable only in the dripping regime. Mono-dispersity of the forming droplets in the transition regime can be also achieved by removing the tiny satellite droplets from the forming polydisperse micro-emulsion.

The experimental measurements for co-flowing ionized water and PDMS oil (Utada et al., 2007) and the present numerical results are compared to the developed dimensionless correlation and the results of a linear instability analysis for the boundary between the transition and jetting regimes. The linear instability analysis predictions are consistently lower than the experimental data, as well as the present numerical simulation results. The present dimensionless correlations of the boundaries between jetting, transition and dripping regimes agree well with the reported experimental data and present numerical results. Such good agreement of the correlation further confirms the soundness of the present numerical simulations and validates the present parametric dimensionless analysis and developed correlations.

The effects of various operation parameters and liquids properties on the radius and formation frequency of the monodisperse droplets are parametrically investigated. The parametric numerical analysis investigated the effects of the interfacial tension, velocities and viscosities of the two immiscible liquids and the diameters of the coaxial microtubes on the monodisperse droplet radius and formation frequency. The obtained results are used to develop semi-empirical dimensionless correlations of the dimensionless radius ( $r_d^*$ ) and the corresponding formation frequency ($f^*$) of the monodisperse droplets in the dripping regime as well as in the transition regime when the total volume of satellite droplets is <

1% of the primary droplets. The developed correlations are expressed in terms of the continuous liquid capillary number ($Ca_c$) and the ratios of Reynolds numbers ($Re_d/Re_c$) and microtubes' radii of the co-flowing immiscible liquids ($R^*$). They are applicable for when $r_d < 0.5R_c$. The correlation for $r_d^*$ is within +20% to −6%, while that for $f^*$ is within +20% to −30% of the numerical calculations. The correlation for the dimensionless radius of the disperse droplets is within +10% to −14% of recently reported experimental measurements for the formation of water droplets in a co-axial continuous flow of salad oil in the dripping regime (Gu et al., 2011). Such good agreement validates the accuracy of the developed correlations for calculating the radius and the formation frequency of the disperse droplets.

The developed dimensionless correlations for the radius of frequency of disperse droplets as well as for the boundaries between dripping, transition and jetting regimes are directly applicable to designing prototype or commercial coaxial microtubes emulsion generators. They are also useful for determining the operation of prototype micro-systems, requiring highly monodisperse droplets.

# 8. RECOMMENDATIONS FOR FUTURE WORK

This research identifies additional work for enhancing the present parametric dimensionless analysis on the formation dynamics of disperse droplets using co-flowing immiscible liquids in coaxial microtubes. The developed dimensionless correlations in this research are developed for the boundaries between the dripping, transition and jetting regimes. Additional correlations are also developed for the radius and formation frequency of disperse droplet in the dripping regime and the transition regime, when the total volume of the satellite droplets is less than 1% of the disperse primary droplets. Suggestions for future research to expand on the developed dimensionless correlations are summarized below.

*(1) Perform experimental verification of the developed correlation for the boundary between dripping and transition regimes.*

Although the developed correlations, based on the compiled results of present numerical simulations on forming disperse droplets, are validated by comparing with reported measurements by various experiments, additional experiments specially on forming droplets in transition regime need to be conducted. All reported experimental results did not identify the transition regime, considering it a part of dripping. Experiments for forming droplets in the transition regime can further validate the developed correlation for the boundary between dripping and transition regimes.

(2) *Investigate the formation of large disperse droplets ($r_d$>0.5$R_c$) in the dripping and in the transtion regime when the volume of the satellite droplets < 1% of the disperse primary droplet.*

Chapter 6 demonstrate that large droplets are generally produced when the injection velocity of the continuous liquid is much less than that of the disperse liquid. In this case, the diameter of the growing droplet at the tip of the inner microtube is comparable to that of the outer microtube. These droplets become elongated axially, and then pinches off as a bullet-like shape, with high curvature in the leading edge and low curvature in the trailing edge. This deformation of a forming disperse droplet at the tip of the inner microtube reduces its sphericity, the ratio of the surface area of a sphere (with the same volume as the deformed droplet) to the surface area of the deformed droplet. The sphericity of the deforming droplet decreases with increasing the rate of momentum transfer at the interface. If this effect could be quantified with prevailing dimensionless group, the present correlation for the size and formation frequency of disperse droplets could be extended to $r_d > 0.5R_c$ by adding the effect of the sphericity on the forming droplets to the correlations (equations (6.1 and 6.2)).

(3) *Investigate the effect of surfactant on forming disperse droplet.*

In the present numerical simulations, the interfacial tension is kept constant. This is not applicable in the case of an added surfactants to the disperse liquid. The gradient of the surfactant along the interface stimulate Marangoni convection, which would affect the characteristics of the disperse droplet. Additional numerical simulation with the surfactant gradient at the interface could have different results, from the presented results in this work.

# 9. REFERENCES


Abrahamse, A. J., Lierop, R. van der, Sman, R.G.M. van der, Padt, A. van der, and Boom, R.M., 2002, "Analysis of droplet formation and interactions during cross-flow membrane emulsification," J. Membr. Sci., 204, pp. 125 – 137.

Akoh, C. C., and Min, D. B., *Food lipids: chemistry, nutrition and biotechnology (3rd ed.)*, Boca Raton, CRC Press, 2008

Ashgriz, N., *Handbook of Atomization and Sprays*, New York, Springer, 2011.

Brackbill, J. U., Kothe, D. B., and Zemach C., 1992, "Acontinuum method for modeling surface tension," J. Computational Phys., 100(2), pp. 335–354.

Brivio, M., Verboom, W., and Reinhoudt, D. N., 2006, "Miniaturized continuous flow reaction vessels: influence on chemical reactions," Lab Chip, 6, pp.329-344.

Brouzes, E., Medkova, M., Savenelli, N., Marran, D., Twardowski, M., Hutchison, J. B., Mothberg, J. M., Link, D. R., Perrimon, N., and Samuels M. L., 2009, "Droplet microfluidic technology for single-cell high-throughput screening," PNAS, 106(34), pp. 14195 – 14200.

Carroll, N. J., Rathod, S. B., Derbins, E., Mendez, S., Weitz, D. A., and Petsev, D. N., "Droplet-based microfluidics for emulsion and solvent evaporation synthesis of monodisperse mesoporous silica microspheres," Langmuir, 24(3), 658 – 661.

Castro-Hernandez, E., Gundabala, V., Fernandez-Nieves, A., and Gordillo, J. M., 2009, "Scaling the drop size in coflow experiments," New J. Phys., 11(7), paper no. 075021.

Chabert, M., and Viovy, J.-L., 2008, "Microfluidic high-throughput encapsulation and hydrodynamic self-sorting of single cells," PNAS, 105(9), pp. 3191-3196.

Colin, T., and Tancogne, S., 2011, "Stability of bifluid jets in microchannels," Eur. J. Mech. B-Fluids, 30, pp. 409-420.

Comsol CFD user's guide, Comsol AB., Stockholm, 2010, 155–272, http://www.comsol.com.

Cordero, M. L., Gallaire, F., and Baroud, C. N., 2011, "Quantitative analysis of the dripping and jetting regimes in co-flowing capillary jets," Phys. Fluids, 23(9), paper no. 094111.

Cramer, C., Beruter, B., Fischer, P., and Windhab, E. J., 2002, "Liquid Jet Stability in a Laminar Flow Field," Chem. Eng. Technol., 25(5), 499-506.

Cramer, C., Fischer, P., and Windhab, E. J., 2004, "Drop formation in a co-flowing ambient fluid," Chem. Eng. Sci., 59(15), pp. 3045-3058.

Cubaud, T., and Mason, T. G., 2008, "Capillary threads and viscous droplets in square microchannels," Phys. Fluids, 20, paper no. 053302.

Cygan, Z. T., Cabral, J. T., Beer, K. L., and Amis, E. J., 2005, "Microfluidic platform for the generation of organic-phase microreactors," Langmuir, 21, pp. 3629-3634.

De Menech, M. D., Garstecki, P., Jousse, F., and Stone, H. A., 2008, "Transition from squeezing to dripping in a microfluidic T-shaped junction," J. Fluid Mech., 595, 141-161.

Duffy, D. C., Mcdonald, J. C., Schueller, O. J. A., and Whitesides, G. M., 1998, "Rapid prototyping of microfluidic systems in poly(dimethylsiloxane)," Anal. Chem., 70, pp. 4974-4984.

El-Genk, M.S., and Yang, I.H., 2009, "Numerical analysis of laminar flow in micro-tubes with a slip boundary," Energy Conversion and Management 50 (6), pp. 1481-1490.

El-Genk, M.S., and Yang, I.H., 2008, "Friction numbers and viscous dissipation heating for laminar flows of water in microtubes," Journal of Heat Transfer 130 (8), paper no. 082405.

Garstecki, P., Fuerstman, M. J., Stone, H. A., and Whitesides, G. M., 2006, "Formation of droplets and bubbles in a microfluidic T-junction-scaling and mechanism of break-up," Lab Chip, 6, 437-446.

Garstecki, P., Stone, H. A., and Whitesides, G. M., 2005, "Mechanism for flow-rate controlled breakup in confined geometries a route to monodisperse emulsions," Phy. Rev. Lett., 94, paper no. 164501.

Gu, Y., Kojima, H., and Miki, N., 2011, "Theoretical anlysis of 3D emulsion droplet generation by a device using coaxial glass tubes," Sens. Actuators A: Phys., 169(2), pp. 326-332.

Guillot, P., A. Colin, Utada, A. S., and Ajdari, A., 2007, "Stability of a jet in confined pressure-driven biphasic flows at low Reynolds numbers," Phys. Rev. Lett., 99(10), paper no. 104502.

Guillot, P., Colin, A., and Ajdari, A., 2008, "Stability of a jet in confined pressure-driven biphasic flows at low Reynolds number in various gemetries," Phys. Rev. E., 99(10), paper no. 016307.

Guillot, P., Colin, A., Utada, A. S., and Ajdari, A., 2007,"Stability of a jet in confined pressure-driven biphasic flows at low Reynolds numbers," Phys. Rev. Lett., 99(10), paper no. 104502.

Gupta, A., Murshed, S. M. S., and Kumar, R., 2009, "Droplet formation and stability of flows in a microfludic T-junction," Appl. Phys. Lett, 2009, 94, no. 164107.

Henderson, D. M., Pritchard, W. G., and Smolka, L. B, 1997, "On the pinch-off of a pendant drop of viscous fluid," Phys. Fluids, 9(11), pp. 3188 – 3200.

Herrada, M. A., G.-Calvo, A. M., and Guillot, P., 2008, "Spatiotemporal instability of a confined capillary jet," Phys. Rev. E, 78, paper no. 046312.

Hirt, C. W., and Nichols, B. D., 1981, "Volume of fluid (VOF) Method for the dynamics of free boundaries," J. Computational Phys., 39, pp. 201–225.

Homma, S., Koga, J., Matsumoto, S., Song, M., and Tryggvason, G., 2006, "Breakup mode of an axisymmetric liquid jet injected into another immiscible liquid," Chem. Eng. Sci., 61, pp. 2986-3996.

Hong, Y., and Wang, F., 2007, "Flow rate effect on droplet control in a co-flowing microfluidic device," Microfluid Nanofluid, 3(3), pp. 341–346.

Hua, J., Zhang, B., and Lou, J., 2007, "Numerical simulation of microdroplet formation in coflowing immiscible liquids," AIChE Journal, 53(10), pp. 2534–2547.

Huerre, P., and Monkewitz, P. A., 1990, "Local and global instabilities in spatially developing flows," Annu. Rev. Flud. Mech ., 22, pp. 473-537.

Jin, F., Gupta, N. R., and Stebe, K. J., 2006, "The detachment of a viscous drop in a viscous solution in the presence of a soluble surfactant," Phys. Fluids, 18(2), paper no. 022103.

Jog, C. S., *Foundations and Applications of Mechanics: Fluid Mechanics*, Boca Raton, CRC Press, 2002.

Keller, J. B., Rubinow, S. I., and Tu, Y. O., 1973, "Spatial instability of a jet," Phys. Fluids, 16(12), pp. 2052-2055.

Kelly, B. T., Baret, J.-C., Taly, V., and Griffiths, A. D., 2007, "Minaturizing chemistry and biology in microdroplets," Chem. Commun., pp. 1173-1788.

Kobayashi, I., Nakajima, M., Chun, K., Kikuchi, Y., and Fujita, H., 2002, "Silicon array of elongated through-holes for monodisperse emulsion droplets," AIChE J., 48(8), pp. 1639 – 1644.

Kobayashi, I., Mukatada, S., and Nakajima, M., 2004, "Effect of slot aspect ratio on droplet formation from silicon straight-through microchannels," J. Colloid Interface Sci., 279, pp. 277 – 280.

Koster, S., Angile, F. E., Duan, H., Agresti, J. J., Wintner, A., Schmitz, C., Rowa, C. A., Merten, C. A., Pisignano, D., Griffiths, A. D., and Weitz, D. A., 2008, "Drop-based microfluidic devices for encapsulation of single cells," Lab Chip, 8, pp. 1110 – 1115.

Leib, S. J., and Goldstein, M. E., 1986a, "The generation of capillary instabilities on a liquid jet", J. Fluid. Mech., 1986, 168, pp. 479-500.

Leib, S. J., and Goldstein, M. E., 1986b"Convective and absolute instability of a viscous liquid jet," Phys. Fluids, 29(4), pp. 952-954.

Link, D. R., G.-Mongrain, E., Duri, A., Sarrazin, F., Cheng, Z., Cristobal, G., Marquez, M., and Weitz, D. A., 2006, "Electric control of droplets in microfluidic devices," Angew. Chem., 118, pp. 2618-2622.

Liu, H., and Zhang, Y., 2011, "Lattice Boltzmann simulation of droplet generation in a microfluidic cross-junction," Commun. Comput. Phys., 9(5), 1235-1256.

Manz, A., Graber, N., and Widmer, H. M., 1990, "Miniaturized total chemical analysis systems: a novel concept for chemical sensing," Sensors and Actuators, B1, pp. 244-248.

Munson, M. S., Hasenbank, M. S., Fu, E., and Yager, P., 2004, "Suppression of non-specific adsorption using sheath flow," Lab Chip, 4, pp. 438-445.

Murshed, S. M. S., Tan, S. H., Nguyen, N. T., Wong, T. N., and Yobas, L., 2009, "Microdroplet formation of water and nonofluids in heat-induced microfluidic T-junction," Microfluid Nanofluid, 6, pp. 253-259.

O'Donnel, B., Chen , J. N., and Lin, S. P., 2001, "Transition from convective to absolute instability in a liquid jet," Phys. Fluids, 13(9), pp. 2732-2734.

Petersen, K. E., 1982, "Slicon as a mechanical material," Proc. IEEE, 70, pp. 420-457.

R.-Choudhury, P., 1997, *Handbook of microlithography, micromachining, and microfabrication*, SPIE, Belingham, WA.

Rayleigh, L., 1879, "On the instability of jets," Proc. London Math. Soc. 10, pp. 4-13.

Rayleigh, L., 1892, "On the instability of a cylinder of viscous liquid under capillary force," Phil. Mag., 34, pp. 145 - 154.

Saarloos, W. V., 1988, "Front propagation into unstable state: Marginal stability as a dynamical mechanism for velocity selection," Phys, Rev. A, 37(1), pp. 211-229.

Saarloos, W. V., 2003, "Front propagation into unstable states," Phys. Rep., 386, pp. 29-229.

Sakai, S., Kawabata, K., Ono, T., Ljima, H., and Kawakami, K., 2004, "Preparation of mammalian cell-enclosing subsieve-sized capsules (<100 μm) in a coflowing stream," Biotechnol. Bioeng., 86(2), 168-173.

Serra, C., Berton, N., Bouquey, M. Prat, L., and Hadziioannou, G., 2007, "A Predictive Approach of the Influence of the Operating Parameters on the Size of Polymer Particles Synthesized in a Simplified Microfluidic System," Langmuir, 23, pp. 7745-7750.

Suryo, R., and Basaran O. A., 2006, "Dripping of a liquid from a tube in the absence of gravity," Phys. Rev. Lett. 96, paper no. 034504.

Tan, S.-H., Murshed, S. M. S., Nguyen, N.-T., Wong, T. N., and Yobas, L, 2008, "Thermally controlled droplet formation in flow focusing geometry: formation regimes and effect of nanoparticle suspension," J. Phys. D: Appl. Phys., 41, 1-7.

Tewhey, R., Warner, J. B., Nakano, M., Libby, B., Medkova, M., Daivd, P. H., Kotsopoulos, S. K., Samuels, M. L., Hutchison, J. B., Larson, J. W., Topol, E. J., Weiner, M. P., Harismendy, O., Olson, J., Link, D. R., and Frazer, K. A., 2009, "Microdroplet-based PCR enrichment for large-scale targeted sequencing," Nat. Biotechnol., 27, pp. 1025-1031.

Ting, T. H., Yap, Y. F., Nguyen, N.-T., Wong, T. N., Chai, J. C. H., and Yobas, L., 2006, "Thermally mediated breakup of drops in microchannels," Appl. Phys. Lett, 89, paper no. 234101.

Tomotika, S., 1935, "On the instability of a cylindrical thread of a viscous liquid surrounded by another viscous fluid," Proc. R. Soc. London Ser. A., 150(870), pp. 322-327.

Ulmeanu, M., 2008, "Preparation and characterization of water in oil emulsion via drop break-off," Colloids Surface A, 316, pp. 119-124.

Umbanhowar, P. B., Prasad, V., and Weitz, D. A., 2000, "Monodisperse emulsion generation via drop break off in a coflowing stream," Langmuir, 16, 347-351.

Utada, A. S., Fernandez-Nieves, A., Stone, H. A., and Weitz, D. A., 2007, "Dripping to jetting transitions in coflowing liquid streams," Phys. Rev. Lett., 99(9), paper no. 094502.

Velve-Casquillas, G., Berre, M. L., Piel, M., and Tran, P. T., 2010, "Microfluidic tools for cell biological research," Nano Today, 5, pp. 28-47.

Vempati, B., Panchagnula, M. V., and Neti, A. O. S., 2007, "Numerical investigation of liquid-liquid coaxial flows," J. Fluids Eng., 129(6), pp. 713–719.

Vladisavljevic, G. T., Shimizu, M., and Nakashima, T., 2004, "Preparation of monodisperse multiple emulsions at high production rates by multi-stage premix membrane emulsification," J. Membr. Sci., 244, pp. 97 – 106.

Wang, W., Yang, C., and Li, C. M., 2009, "Efficient on-demand compound droplet formation: from microfluidics to microdroplets as miniaturized laboratories," Small, 5(10), 1149-1152.

Xu, J. H., Li, S. W., Tan, J., Wang, Y. J., and Luo, G. S., 2006, "Preparation of highly monodisperse droplet in a T-junction microfluidic device," AIChE J., 52(9), 3005-3010.

Yang, C.-H., Lin, Y.-S, Huang, K.-S., Huang, Y.-C., Wang, E.-C., Jhong, J.-Y., and Kuo, C.-Y., 2009, "Microfludic emulsification and sorting assisted preparation of monodisperse chitosan micropaticles," Lab Chip, 9, pp. 145-150.

Yang, I. H., and El-Genk, M. S., 2011b, "Emulsion Formation in Dripping Regime of Co-Flowing Immiscible Liquids in Co-aixal Micro-tubes," Int. J. Micro-Nano scale transport, 2 (1), pp. 57-84.

Yang, I.H., and El-Genk, M.S., 2011a "Parametric analysis of microdroplet formation in co-axial co-flowing immiscible liquids in microtubes", Proc. ASME 9th International Conference on Nanochannels, Microchannels, and Minichannels, paper no. 58088.

Yuyama, H., Yamamoto, K., Shirafuji, K., Nagai, M., Ma, G.-H., and Omi, S., 2000, "Preparation of polyurethaneurea (PUU) uniform spheres by SPG Membrane emulsification technique," J. Appl. Polym Sci., 77, pp. 2237-2245.

Zagnoni, M., Anderson, J., and Cooper, J. M., 2010, "Hystersis in multiphase microfluidics at a T-junction," Langmuir, 26(12), pp. 9416-9422.

Zhang, D. F., and Stone, H. A., 1997, "Drop formation in viscous flows at a vertical capillary tube," Phys. Fluids, 9(8), pp. 2234-2242.

Zhang, X., 1999, "Dynamics of drop formation in viscous flows," Chem. Eng. Sci., 54(12), pp. 1759–1774.

Zhang, X., and Basaran, O. A., 1995, "An experimental study of dynamics of drop formation," Phys. Fluids, 7(6), pp. 1184-1203.

Ziemecka, I., van Stejin, V., Koper, G. J. M., Rosso, M., Brizard, A. M., van Esch, J. H., and Kreutzer, M. T., 2011, "Monodisperse hydrogel microspheres by forced droplet formation in aqueous two-phase systems," Lab Chip, 11, 620-624.

Gada, V. H., and Sharma, A., 2009, "On derivation and physical-interpretation of level set method based equations for two-phase flow simulations," Numer. Heat Transfer B, 56, pp. 307–322.

Olsson, E., Kreiss, G., and Zahedi, S., 2007, "A conservative level set method for two phase flow II," J. Computational Phys, 225(1), pp. 785–807.

Wolfram Mathmatica 8.0 Tutorial Collection, Wolfram Research, Inc., USA, http://www.wolfram.com.

## APPENDIX-A. *DN* and *NM* in equation (5.26)

This appendix presents the functions of *DN* and *NM* used in equation (5.26) for calculating the determinant of the square matrix (equation (5.24)). These functions are fully expanded in terms of $Ka$, $R_c^*$ and $\mu_r$:

$$
\begin{aligned}
DN = {} & (1/k^*)\,((\mu_r-1)^2 k^{*3}(R_c^* k^*) K_0(R_c^* k^*)+K_1(R_c^* k^*)(2K_0(R_c^* k^*)- R_c^* k^* K_1(R_c^* k^*))) \\
& I_0(k^*)^4+(\mu_r-1)^2 k^{*2}(R_c^* k^*((k^*-\mu_r k^*) K_0(k^*)+\mu_r K_1(k^*)) I_0(R_c^* k^*)^2+(-2(\mu_r-1) R_c^* k^* \\
& I_1(k^*) K_0(R_c^* k^*)-(\mu_r-1) k^* K_0(k^*)(R_c^* k^* K_0(R_c^* k^*)+2K_1(R_c^* k^*))+ K_1(k^*)((\mu_r-1) I_1 \\
& (R_c^* k^*) k^{*2}-(\mu_r-2) R_c^* K_0(R_c^* k^*) k^*+((\mu_r-1)(R_c^{*2}+1) k^{*2}+2\mu_r) K_1(R_c^* k^*)))+ I_0(R_c^* \\
& k^*)+2(\mu_r-1) I_1(k^*) K_1(R_c^* k^*)(R_c^* k^* K_1(R_c^* k^*)- 2K_0(R_c^* k^*))+ I_1(R_c^* k^*)+(K_1(k^*)(((\mu_r \\
& -1) R_c^{*2} k^{*2} 2(\mu_r-2)) K_0(R_c^* k^*)+ R_c^* k^* K_1(R_c^* k^*))-2(\mu_r-1) k^* K_0(k^*)(R_c^* k^* K_1(R_c^* \\
& k^*)- K_0(R_c^* k^*)))) I_0(k^*)^3+ k^*(-R_c^* k^*(-(\mu_r-1)^2 k^{*2} K_0(k^*)^2+2(\mu_r-1) k^* K_1(k^*) K_0 \\
& (k^*)+((\mu_r-1)^2 k^{*2}+(\mu_r-2)\mu_r) K_1(k^*)^2+(\mu_r-1) I_1(k^*)((2-3\mu_r) k^* K_0(k^*)+((\mu_r-1) k^{*2}+3 \\
& \mu_r) K_1(k^*))) I_0(R_c^* k^*)^2+(-(\mu_r-1)^2 R_c^* k^*(2k^{*2}+1) K_0(R_c^* k^*) I_1(k^*)^2+(\mu_r-1)(I_1(R_c^* k^*) \\
& ((\mu_r-1) k^* K_0(k^*)-2\mu_r K_1(k^*)) k^{*2}+ K_0(k^*)(\mu_r R_c^* k^* K_0(R_c^* k^*)+((\mu_r-1)(R_c^{*2}+1) \\
& k^{*2}+6\mu_r-4) K_1(R_c^* k^*)) k^* K_1(k^*)(R_c^* k^*(\mu_r-(\mu_r-1) k^{*2}) K_0(R_c^* k^*)-2((\mu_r(R_c^{*2}+1) \\
& -1) k^{*2}+3\mu_r) K_1(R_c^* k^*))) I_1(k^*)+2 I_1(R_c^* k^*)(-(\mu_r-1)^2 k^{*2} K_0(k^*)^2+2(\mu_r-1) k^* K_1 \\
& (k^*) K_0(k^*)+((\mu_r-1)^2 k^{*2}+(\mu_r-2)\mu_r) K_1(k^*)^2)) I_0(R_c^* k^*)+ R_c^* k^* I_1(R_c^* k^*)^2(-(\mu_r-1)^2 \\
& k^{*2} K_0(k^*)^2+2(\mu_r-1) k^* K_1(k^*) K_0(k^*)+((\mu_r-1)^2 k^{*2}+(\mu_r-2)\mu_r) K_1(k^*)^2)+(\mu_r-1)^2 \\
& (2k^{*2}+1) I_1(k^*)^2 K_1(R_c^* k^*)(R_c^* k^* K_1(R_c^* k^*)-2K_0(R_c^* k^*))+(\mu_r-1) I_1(k^*) I_1(R_c^* k^*) \\
& (k^* K_0(k^*)(((\mu_r-1) R_c^{*2} k^{*2}-2\mu_r) K_0(R_c^* k^*)+2(2\mu_r-1) R_c^* k^* K_1(R_c^* k^*))-2 K_1(k^*) \\
& (((\mu_r(R_c^{*2}-1)+1) k^{*2}+\mu_r) K_0(R_c^* k^*)+ R_c^* k^*((\mu_r-1) k^{*2}+\mu_r) K_1(R_c^* k^*)))) I_0(k^*)^2+ \\
& I_1(k^*)(R_c^* k^*((\mu_r-1) I_1(k^*)(k^*((\mu_r-1) k^{*2}-2\mu_r-1) K_0(k^*)+\mu_r(k^{*2}+2) K_1(k^*))+2 \\
& \mu_r(-(\mu_r-1) k^{*2} K_0(k^*)^2+ k^* K_1(k^*) K_0(k^*)+(\mu_r-1)(k^{*2}+1) K_1(k^*)^2)) I_0(R_c^* k^*)^2- \\
& (-2(\mu_r-1)^2 R_c^* k^*(k^{*2}+1) K_0(R_c^* k^*) I_1(k^*)^2+(\mu_r-1)(I_1(R_c^* k^*)(2\mu_r k^* K_0(k^*)+((\mu_r \\
& -1) k^{*2}-1) K_1(k^*)) k^{*2}+ K_0(k^*)(R_c^* k^*((1-\mu_r) k^{*2}-2\mu_r+1) K_0(R_c^* k^*)+2((\mu_r R_c^{*2}+ \\
& 1) k^{*2}+2\mu_r+1) K_1(R_c^* k^*)) k^*+ K_1(k^*)(R_c^* k^*((2-3\mu_r) k^{*2}-2\mu_r+2) K_0(R_c^* k^*)+((\mu_r \\
& -1)(R_c^{*2}+1) k^{*4}-(R_c^{*2}+2\mu_r+1) k^{*2}-4\mu_r) K_1(R_c^* k^*))) I_1(k^*)+4\mu_r I_1(R_c^* k^*)(-(\mu_r \\
& -1) k^{*2} K_0(k^*)^2+ k^* K_1(k^*) K_0(k^*)+(\mu_r-1)(k^{*2}+1) K_1(k^*)^2) I_0(R_c^* k^*)+2\mu_r R_c^* k^* I_1 \\
& (R_c^* k^*)^2((\mu_r-1) k^{*2} K_0(k^*)^2- k^* K_1(k^*) K_0(k^*)-(\mu_r-1)(k^{*2}+1) K_1(k^*)^2)-2(\mu_r-1)^2 \\
& (k^{*2}+1) I_1(k^*)^2 K_1(R_c^* k^*) R_c^* k^* K_1(R_c^* k^*)-2K_0(R_c^* k^*))+(\mu_r-1) I_1(k^*) I_1(R_c^* k^*) \\
& (K_1(k^*)((-(\mu_r-1) R_c^{*2} k^{*4}+(R_c^{*2}-6\mu_r+4) k^{*2}-4\mu_r+4) 2K_0(R_c^* k^*)+2(2\mu_r-1) R_c^* \\
& k^*(k^{*2}+1) K_1(R_c^* k^*))+2 k^{*2} K_0(k^*)(((-\mu_r R_c^{*2}-\mu_r+1) K_0(R_c^* k^*))+ R_c^* k^*((\mu_r-1) k^{*2} \\
& -1) K_1(R_c^* k^*)))) I_0(k^*)+ I_1(k^*)^2(R_c^* k^*((-(\mu_r-1)^2 k^{*3}+2\mu_r k^*-k^*) K_0(k^*)^2+2(\mu_r-1) \\
& (k^{*2}+1) K_1(k^*) K_0(k^*)+(\mu_r-1)^2 k^*(k^{*2}+1) K_1(k^*)^2-(\mu_r-1) I_1(k^*)((\mu_r-2) k^*-2) K_0 \\
& (k^*)-(\mu_r-1) k^*(k^{*2}+1) K_1(k^*))) I_0(R_c^* k^*)^2+((\mu_r-1)^2 R_c^* k^{*2}(k^{*2}+1) K_0(R_c^* k^*) I_1 \\
& (k^*)^2-(\mu_r-1)(((\mu_r-1) k^{*2}-1) I_1(R_c^* k^*) K_0(k^*) k^{*2}-(\mu_r-1)(k^{*2}+1) K_1(k^*)(R_c^* k^* \\
& K_0(R_c^* k^*)+2K_1(R_c^* k^*)) k^*+ K_0(k^*)(((\mu_r-1)(R_c^{*2}+1) k^{*4}-(R_c^{*2}-2\mu_r+5) k^{*2}-4) \\
& K_1(R_c^* k^*)-\mu_r R_c^* k^{*3} K_0(R_c^* k^*))) I_1(k^*)+2 I_1(R_c^* k^*)(((\mu_r-1)^2 k^{*3}-2\mu_r k^*+k)^* \\
& K_1(k^*)^2-2(\mu_r-1)(k^{*2}+1) K_1(k^*) K_0(k^*)-(\mu_r-1)^2 k^*(k^{*2}+1) K_1(k^*)^2)) I_0(R_c^* k^*)- \\
& k^*((\mu_r-1)^2(k^{*2}+1) K_1(R_c^* k^*)(R_c^* k^{*3} K_1(R_c^* k^*)-2K_0(R_c^* k^*) I_1(k^*)^2-(\mu_r-1) I_1(R_c^* \\
& k^*)(K_0(k^*)(k^*(((\mu_r-1) k^{*2}-1) k^{*2}-1) R_c^{*2}+2\mu_r) 2K_0(R_c^* k^*)-2 R_c^*(k^{*2}+1) K_1(R_c^* \\
& k^*))-2(\mu_r-1)(k^{*2}+1) K_1(k^*)(R_c^* k^* K_1(R_c^* k^*)- K_0(R_c^* k^*))) I_1(k^*)+ R_c^* I_1(R_c^* k^*)^2
\end{aligned}
$$

$((-(\mu_r - 1)^2 k^{*3} + 2\mu_r k^* - k^*) K_0(k^*)^2 + 2(\mu_r - 1)(k^{*2} + 1) K_1(k^*) K_0(k^*) + (\mu_r - 1)^2 k^*(k^{*2} + 1) K_0(k^*)^2))))$,

and,

$NM = (\mu_r k^{*2} I_0(R_c^* k^*) K_1(k^*) (I_1(R_c^* k^*) + K_1(R_c^* k^*)) I_0(k^*)^3 + k^*(\mu_r R_c^* k^* K_1(k^*) (I_1(k^*) + K_1(k^*)) I_0(R_c^* k^*)^2 + (-(\mu_r - 1) R_c^* k^* K_0(R_c^* k^*) I_0(k^*)^2 + \mu_r(I_1(R_c^* k^*) (k^* K_0(k^*) 2K_1(k^*)) - R_c^* k^* K_0(R_c^* k^*) K_1(k^*) + (k^* K_0(k^*) - 4K_1(k^*)) K_1(R_c^* k^*)) I_1(k^*) + 2\mu_r I_1(R_c^* k^*) K_1(k^*)^2) I_0(R_c^* k^*) + \mu_r R_c^* k^* I_1(R_c^* k^*)^2 + 2\mu_r I_1(k^*) I_1(R_c^* k^*) K_1(k^*) (K_0(R_c^* k^*) - R_c^* k^* K_1(R_c^* k^*) + (\mu_r - 1) I_1(k^*)^2 K_1(R_c^* k^*) (R_c^* k^* K_1(R_c^* k^*) - 2K_0(R_c^* k^*))) I_0(k^*)^2 + I_1(k^*) (R_c^* k^*(2\mu_r K_1(k^*)^2 + I_1(k^*) (2\mu_r K_1(k^*) - k^* K_0(k^*))) I_0(R_c^* k^*)^2 - (-2(\mu_r - 1) R_c^* k^* K_0(R_c^* k^*) I_1(k^*)^2 + k^* I_1(R_c^* k^*) (2\mu_r K_0(k^*) + (\mu_r - 1) k^* K_1(k^*)) + k^* K_0(k^*) (R_c^* k^* K_0(R_c^* k^*) + 2(\mu_r + 1) K_1(R_c^* k^*)) - K_1(k^*) (2(\mu_r - 1) R_c^* k^* K_0(R_c^* k^*) + ((R_c^{*2} - \mu_r + 1) k^{*2} + 4\mu_r) K_1(R_c^* k^*))) I_1(k^*) + 4\mu_r I_1(R_c^* k^*) K_1(k^*)^2) I_0(R_c^* k^*) - 2\mu_r R_c^* k^* I_1(R_c^* k^*)^2 K_1(k^*)^2 - 2(\mu_r + 1) I_1(k^*)^2 K_1(R_c^* k^*) (R_c^* k^* K_1(R_c^* k^*) - 2K_0(R_c^* k^*)) + I_1(k^*) I_1(R_c^* k^*) (2k^* K_0(k^*) (K_0(R_c^* k^*) - R_c^* k^* K_1(R_c^* k^*)) + K_1(k^*) ((R_c^{*2} k^{*2} - 4\mu_r + 4) K_0(R_c^* k^*) + 2(2\mu_r + 1) R_c^* k^* K_1(R_c^* k^*)))) I_0(k^*) + I_1(k^*)^2 (R_c^* k^* (k^* K_0(k^*)^2 + 2K_1(k^*) K_0(k^*) + (\mu_r - 1) k^* K_1(k^*)^2 + I_1(k^*) (2K_0(k^*) + (\mu_r - 1) k^* K_1(k^*))) I_0(R_c^* k^*)^2 + ((\mu_r - 1) R_c^* k^{*2} K_0(R_c^* k^*) I_1(k^*)^2 + (-(\mu_r - 1) I_1(R_c^* k^*) K_0(k^*) k^{*2} + (\mu_r - 1) R_c^* K_0(R_c^* k^*) K_1(k^*) k^{*2} + (((R_c^{*2} - \mu_r + 1) k^{*2} + 4) K_0(k^*) + 2(\mu_r - 1) k^* K_1(k^*)) K_1(R_c^* k^*)) I_1(k^*) - 2I_1(R_c^* k^*) (k^* K_0(k^*)^2 + 2K_1(k^*) K_0(k^*) + (\mu_r - 1) k^* K_1(k^*)^2)) I_0(R_c^* k^*) + k^*((\mu_r - 1) K_1(R_c^* k^*) (2K_0(R_c^* k^*) - R_c^* k^* K_1(R_c^* k^*)) I_1(k^*)^2 + I_1(R_c^* k^*) R_c^* K_0(k^*) (R_c^* k^* K_0(R_c^* k^*) + 2K_1(R_c^* k^*)) - 2(\mu_r - 1) K_1(k^*) (K_0(R_c^* k^*) - R_c^* k^* K_1(R_c^* k^*))) I_1(k^*) - R_c^* I_1(R_c^* k^*)^2 (k^* K_0(k^*)^2 + 2K_1(k^*) K_0(k^*) + (\mu_r - 1) k^* K_1(k^*)^2))))$.